Ollscoil na hÉireann, Corcaigh
National University of Ireland, Cork

Illumination Light Manipulation and Engineering for Sensitive Detection

Thesis presented by
Hui Ma

ORCID: 0009-0006-9280-2159

for the degree of
Doctor of Philosophy

University College Cork

Engineering Science Department

Head of Department: Fatima Gunning
Supervisor: Stefan Andersson-Engels
Co-supervisor: Sanathana Konugolu Venkata Sekar
Co-supervisor: Rekha Gautam

2025

Illumination Light Manipulation and Engineering for Sensitive Detection

Biophotonics, Tyndall National Institute
Department of Physics
University College Cork, UCC
Ireland

For my family!

Abstract

Biophotonic diagnostics provide noninvasive access to structural and biochemical information, yet their performance is often limited by uncontrolled light delivery, depth-dependent signal loss, and a lack of physiological standardisation. This thesis builds on the hypothesis that diagnostic accuracy can be significantly improved by engineering illumination to actively direct photon transport rather than treating it as a static constraint. A series of illumination strategies are therefore developed across multiple platforms, progressing from fundamental beam control to application-specific sensing systems.

The thesis begins by establishing a framework for structured illumination through multimode optical fibres using the transmission matrix (TM). A real-valued intensity transmission matrix (RVITM) approach is implemented to generate controlled circular symmetric output patterns such as rings and combinations of rings without interferometric detection using a 16×16 Hadamard calibration basis. The generated patterns, including rings of tunable radius and composite double ring profiles, remain stable under fibre bending, demonstrating robustness against mode scrambling and providing a compact, axicon free route to programmable beam shaping at the fibre tip.

To address the need for spatially uniform illumination in quantitative imaging, a Köhler integrator based laser microscope incorporating dual microlens arrays (500 µm pitch, 13.8 mm focal length) is developed to homogenise excitation across the sample plane, achieving a coefficient of variation (CV) of approximately 1.2 to 1.5% across the field of view. This system is applied to upconversion nanoparticle (UCNP) assisted biomarker imaging for semi-quantitative assessment of HER2 expression (scoring levels 0 to 3+) in breast cancer tissues. The UCNP labelled samples achieved a signal to background ratio of 40, representing a 25 fold improvement over conventional 3,3′-diaminobenzidine (DAB) chromogenic staining (ratio of 1.6), demonstrating substantially enhanced contrast and quantification accuracy in widefield cancer diagnostics.

For subsurface biochemical detection, tailored illumination is applied in Raman spectroscopy. A dual wavelength inverse spatially offset Raman spectroscopy (DWiSORS) system is implemented using axicon based ring illumination with excitation at 730 nm and 830 nm, enabling simultaneous access to the fingerprint (393 to 2195 cm^{-1}) and high wavenumber (2043 to 3846 cm^{-1}) spectral regions. A novel enhancement to noise ratio (ENR) metric is introduced to determine the optimal spatial offset for subsurface probing, yielding patient specific optimal offsets in the range of 5 to 9 mm. Validated through Monte Carlo simulations and two layer tissue mimicking phantom measurements, the system demonstrates sensitive detection of bone mineral and hydration markers at depths of up to 14 mm through overlying soft tissue, with in vivo measurements performed on ten healthy volunteers.

Finally, to enable calibration of optical sensing systems under physiologically relevant conditions, a light guided solid dynamic phantom is constructed. By integrating a polymer optical fibre (3 mm diameter) with

a liquid crystal display modulator, the phantom reproduces wavelength specific pulsatile absorption changes across four wavelengths (455, 530, 660, and 940 nm). The system accurately simulates photoplethysmography (PPG) signals across a range of heart rates (80 to 120 bpm) and oxygen saturation levels (SpO_2: 86 to 100%), providing a controllable and reproducible platform for pulse oximeter calibration and validation that outperforms conventional liquid blood based phantoms in stability, response time, and spatial controllability.

Across the different systems, analytical modelling frameworks are used to guide illumination strategy and interpret photon transport behaviour. In the Raman studies, these are further supported by Monte Carlo simulations to quantify depth sensitivity and validate experimental trends. Together, this work establishes illumination as a powerful design parameter for enhancing sensitivity, selectivity, and reliability in biophotonic diagnostics, paving the way for future platforms where light delivery is adaptively matched to the sensing target.

List of Publications

This thesis is based in the following research papers, which will be referenced using Roman numerals in the text. The works of Papers **I**, **II**, and **III** have been published, while Paper **IV** has recently been submitted for publication.

I **High contrast breast cancer biomarker semi-quantification and immunohistochemistry imaging using upconverting nanoparticles**
S. Konugolu Venkata Sekar, H. Ma, K. Komolibus, G. Dumlupinar, M. J. Mickert, K. Krawczyk and S. Andersson-Engels.
Biomedical Optics Express **15**, 900-909 (2024).

II **Light-guided dynamic phantom to mimic microvasculature for biomedical applications: an exploration for pulse oximeter**
H. Ma, D. Angelone, C. N. Guadagno, S. Andersson-Engels and S. Konugolu Venkata Sekar.
Journal of Biomedical Optics **29(S3)**, S33312 (2024).

III **Raman Spectroscopy based framework for In-Vivo Assessment of Bone Composition**
H. Ma, P. Lanka, S. Kothuri, B. Jayet, A. Mahadevan Jansen, S. Andersson-Engels, S. Konugolu Venkata Sekar and R. Gautam.
Journal of Physics: Photonics **8(1)**, 015065 (2026).

IV **Real-valued Intensity Transmission Matrix Based Multimode Fibre Beamshaping for Biophotonics Applications (Submitted for publication)**
H. Ma, R. Gautam,S. Andersson-Engels and S. Konugolu Venkata Sekar.
(2026) *Optics Letters.*

Abbreviations

CPA	Control Pellet Array
CR	Cross Relaxation
CSU	Cooperative Sensitisation Upconversion
CT	Computed Tomography
CV	Coefficient of Variation
CW	Continuous-wave
DAB	3,3'-diaminobenzidine
DMD	Digital Micromirror Device
DOI	Diffuse Optical Imaging
DOT	Diffuse Optical Tomography
ENR	Enhancement-to-noise Ratio
ESA	Excited State Absorption
ETU	Energy Transfer Upconversion
FFPE	Formalin Fixed Paraffin Embedded
fNIRS	Functional Near-infrared Spectroscopy
Hb	Deoxyhaemoglobin
HbO_2	Oxyhaemoglobin
HER2	Human Epidermal Growth Factor Receptor 2
HIER	Heat Induced Antigen Retrieval
HRP	Horseradish Peroxidase
IHC	Immunohistochemistry
iSORS	inverse Spatially Offset Raman Spectroscopy
LCD	Liquid Crystal Display
LED	Light-emitting Diode
MC	Monte Carlo
MCML	Monte Carlo Modelling of Light transport in Multi-Layered tissues
MCX	Monte Carlo eXtreme
MLA	Microlens Array
MMF	Multimode Fibre
MPE	Maximum Permissible Exposure
MRI	Magnetic Resonance Imaging
MSIM	Multifocal Structured Illumination Microscopy
NIR	Near-infrared
OCT	Optical Coherence Tomography
OPRA	Optical Photon Reassignment Microscopy
PA	Photon Avalanche

PPG	Photoplethysmography
PSF	Point Spread Function
RTE	Radiative Transport Equation
RVITM	Real-Valued Intensity Transmission Matrix
SERS	Surface-enhanced Raman Scattering
SFDI	Spatial Frequency Domain Imaging
SIM	Structured Illumination Microscopy
SLM	Spatial Light Modulator
SNR	Signal to Noise Ratio
SORS	Spatially Offset Raman Spectroscopy
SpO_2	Oxygen Saturation
STED	Stimulated Emission Depletion
TBSF	Tris Buffered Saline Containing 1 mM Sodium Fluoride
TIRF-SIM	Total Internal Reflection Fluorescence Structured Illumination Microscopy
TM	Transmission Matrix
UCNPs	Upconverting Nanoparticles

Contents

Chapter 1

Introduction

1.1 Motivation

Modern medicine is evolving from a reactive disease-centric model to proactive and predictive patient-centric approaches [1]. Early detection and continuous monitoring are critical to preventing illness, managing chronic diseases, optimising overall health conditions, and reducing the burden on both patients and healthcare infrastructures [2]. However, conventional diagnostic methods present notable drawbacks. For example, open surgical biopsy is invasive and can cause wound complications and tumour spreading [3]. Imaging techniques like computed tomography (CT) and X-ray expose patients to ionising radiation, raising concerns in vulnerable populations such as children and pregnant women [4, 5]. Magnetic resonance imaging (MRI) uses non-ionising electromagnetic radiation without exposure-related hazard. However, it is expensive, time-consuming, and may be contraindicated in patients with electrically, magnetically, or mechanically activated implants. In addition, the use of contrast agents in MRI is risky for people with allergies or impaired renal function [6]. These limitations highlight the need for alternative diagnostic approaches that are noninvasive, safe, and capable of providing high-resolution and molecular-level information without compromising patient safety or comfort.

Biophotonics provides an alternative solution to the limitations of conventional diagnostic modalities by enabling noninvasive, label-free, and real-time characterisation of biological tissues at both structural and molecular levels through the interaction of light with cells and tissues[7–9]. For example, Optical Coherence Tomography (OCT) utilises low-coherence interferometry to generate high-resolution cross-sectional images of biological tissues [10]. Diffuse optical imaging (DOI) uses near-infrared (NIR) light to probe the absorption and scattering properties of biological tissues. It enables functional imaging of tissue haemodynamics and oxygenation at depths beyond the reach of conventional optical microscopy [11]. Photoacoustic imaging is a hybrid biomedical imaging technique that combines optical excitation with ultrasonic detection to visualise the optical absorption properties of tissues. It provides high-contrast, high-resolution images of vascular structures and tissue composition at greater depths than purely optical methods [12]. Raman spectroscopy is a label-free technique that investigates molecular vibrational modes through the inelastic scattering of monochromatic light. In biophotonics, it enables non-invasive molecular analysis of biological tissues, offering high specificity for detecting biochemical changes. This makes it particularly valuable for applications such as cancer diagnostics, tissue classification, and disease monitoring [13, 14].

While conventional biophotonics techniques have significantly ad-

vanced non-invasive diagnostics by providing structural and molecular insights, their performance is often constrained by factors such as limited spatial resolution and reduced imaging depth. To overcome these limitations, structured illumination has emerged as a powerful approach to improve imaging resolution, increase measurement sensitivity, and selectively probe specific tissue volumes.

This thesis builds on the hypothesis that diagnostic accuracy in biophotonics can be improved through the optimisation of illumination patterns. The goal for this thesis is to develop and evaluate structured, optimised, and programmable illumination strategies that enhance sensitivity, selectivity, and quantitative performance across a range of biophotonics modalities. To achieve this goal, the research addresses four interconnected challenges that limit the performance of current biophotonics techniques. The first challenge is the problem of nonuniform excitation in quantitative imaging, which directly reduces the accuracy and repeatability of biomarker quantification. The second challenge concerns the limited sampling depth in Raman spectroscopy, where signals from subsurface tissues are often obscured by stronger contributions from superficial layers. A third challenge arises from the lack of physiologically realistic calibration platforms, which makes it difficult to standardise optical devices such as pulse oximeters and to evaluate their performance under controlled and reproducible conditions. Finally, there is a need for compact and flexible fibre based illumination shaping to support the development of miniaturised instruments suitable for clinical translation.

Each of these challenges forms the motivation for one of the four scientific papers included in the thesis, and together they demonstrate how illumination engineering can improve biophotonic measurements at several levels, including spatial uniformity, depth sensitivity, physiological realism, and fibre scale control.

1.2 Structure of the thesis

This thesis explores various methods for manipulating illumination light and their applications in precise biomedical sensing, along with the development of a transmission matrix-based illumination system at the fibre tip for flexible beam shaping.

This work was carried out as part of the Biophotonics@Tyndall team, based at Tyndall National Institute in Ireland, and kindly supported by Research Ireland (RI) grants SFI-12/RC/2276_P2 and SFI-22/RP-2TF/10293.

The main results of this thesis are presented in four publications, which will be referred to by their Roman numerals as Papers **I**, **II**, **III**, **IV** respectively, in the text. The main chapters of the thesis provide a more comprehensive background to these papers, including detailed discussions of the state-of-the-art, theoretical frameworks, experimental strategies, and techniques employed, as well as a general discussion that places the main results in the context of existing literature.

Chap. 2 – State of the art presents a state-of-the-art review of structured illumination and light manipulation techniques in biophotonics. It discusses approaches to achieve uniform illumination, and highlights advanced techniques including Structured Illumination Microscopy (SIM), Spatial Frequency Domain Imaging (SFDI), and Stimulated Emission Depletion microscopy (STED). The chapter also explores the use of ring illumination for deep-tissue Raman spectroscopy and the application of spatial light modulators (SLM) with transmission matrix (TM) methods for wavefront shaping and endoscopic imaging.

Chap. 3 – Transmission matrix and beamshaping presents the transmission matrix (TM) framework for light manipulation through

complex optical media. The chapter introduces the theoretical basis of the TM in the linear regime and details experimental strategies for its measurement using both phase-sensitive and intensity-only methods. It also describes how the real-valued intensity transmission matrix (RVITM) enables practical beam shaping through multimode fibres without interferometry, with applications in robust and compact biomedical systems. The chapter complements Paper **IV**.

Chap. 4 – Concepts of biophotonics modalities for tissue diagnostics presents the theoretical background of the biophotonics modalities combined with beam shaping for various diagnostic applications. These concepts form the basis for all the papers included in this thesis. The chapter introduces the use of upconverting nanoparticles (UCNPs) for breast cancer detection, discusses the principles of Raman spectroscopy and inverse spatially offset Raman spectroscopy (iSORS), and explains the fundamentals of diffuse optics and pulse oximetry for tissue characterisation and physiological monitoring.

Chap. 5 – Köhler integrator for wide field imaging presents the theoretical background, design and implementation of Köhler integrator in wide-field optical microscopy. It describes the construction and optimisation of a custom laser-based microscope system employing microlens arrays to achieve spatially uniform excitation at the sample plane. This illumination strategy is applied to enhance image quality and quantification accuracy in UCNP-based imaging for breast cancer diagnostics. The application is described in Paper **I**.

Chap. 6 – Ring illumination for dual wavelength inverse spatially offset Raman spectroscopy presents the development and application of an axicon-based ring illumination system, showcasing light manipulation can enhance the sensitivity of inverse spatially offset Raman spectroscopy (iSORS) for in-depth bone characterisation. Dual-wavelength excitation at 730 nm and 830 nm is used to access both the high wavenumber and fingerprint spectral regions, respectively. The technique is evaluated on tissue-mimicking phantoms, and through in vivo measurements on healthy volunteers, demonstrating its potential for detecting subsurface biochemical changes in bone. The development and evaluation of a dual wavelength iSORS system are described in Paper **III**.

Chap. 7 – A light-guide based dynamic phantom for system validation introduces the design and validation of a light-guided solid dynamic phantom developed to simulate biologically relevant optical signals for system calibration. By integrating a liquid crystal display (LCD) with a polymer optical fibre, the system enables controlled manipulation of light absorption, decouples angular dependence, and allows for rapid, wavelength-specific modulation. The system was characterised across four wavelengths (455, 530, 660, and 940 nm), and its performance was demonstrated through photoplethysmography (PPG) signal generation at various heart rates and simulated oxygen saturation levels. The phantom was further evaluated for its potential to calibrate and validate pulse oximeters and other spectroscopy systems under dynamic physiological conditions. This chapter forms the background to Paper **II**, where the development and characterisation of the dynamic solid phantom are presented in detail.

To conclude, **Chap. 8 – General Discussion** discusses the key findings of this work, compares them with related studies, and reflects on the broader implications of light manipulation for sensitive detection. **Chap. 9 – Conclusions and future perspective** summarises the overall results presented in this thesis and outlines possible directions for future research.

Chapter 2

State of the art

This chapter reviews relevant structured illumination and light pattern manipulation techniques applied in biophotonics. Most conventional light sources emit light with a Gaussian intensity profile, resulting in non-uniform illumination across the field. Obtaining uniform illumination is essential for precise and quantitative microscopic imaging [15]. Structured illumination microscopy (SIM) improves spatial resolution beyond the diffraction limit by projecting patterned light onto the sample and computationally reconstructing high-frequency information [16]. Spatial frequency domain imaging (SFDI) characterises tissue optical properties by projecting spatially modulated light patterns and analysing the diffuse reflectance at different spatial frequencies [17]. Stimulated Emission Depletion (STED) microscopy uses ring illumination to selectively and efficiently deactivate fluorescence around the excitation focus, allowing emission only from a central sub-diffraction region and thereby achieving super-resolution imaging[18]. Ring illumination in biophotonics improves the penetration depth and signal-to-noise ratio (SNR) in Raman spectroscopy [19]. Spatial light modulators (SLMs) combined with the transmission matrix approach enables dynamic wavefront shaping and endoscopic applications [20].

Together, these techniques illustrate the central role of illumination control in advancing biophotonics. They demonstrate how patterned and structured light can enhance resolution, depth penetration, quantitative accuracy, and contrast, thereby addressing fundamental challenges in tissue characterisation and imaging. This context forms the foundation for the research presented in Papers I–IV, where similar concepts of beam shaping, structured illumination, and wavefront engineering are explored and applied to improve diagnostic capabilities.

2.1 Uniform Illumination for Wide Field Imaging System

Illumination uniformity is a critical parameter in wide-field biological imaging applications. Non-uniform illumination typically arises from the Gaussian intensity profile of light sources [21], as well as from vignetting and optical misalignment. As a result, microscopic images often show a brighter area towards the centre and a darker area towards the edges. To address the challenges associated with non-uniform illumination in microscopic imaging, a variety of approaches have been developed to achieve more homogeneous light distribution across the field of view.

Diffractive diffusers are optical components with microstructured surfaces that modify the phase of incoming light, spreading it into a controlled angular or spatial pattern [22]. They act as far-field beam shapers

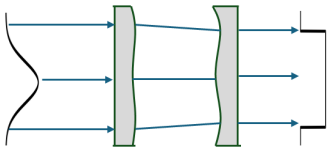

Figure 2.1: πShaper optical layout

by creating many diffracted orders that interfere with one another. When specific spatial frequencies are encoded onto the phase of the laser beam, the light undergoes self-interference as it propagates. This causes the beam to form a defined pattern with a fixed divergence angle, determined by those spatial frequencies [23, 24].

While diffractive diffusers offer precise and compact solutions for far-field beam shaping, their performance is wavelength dependent due to the nature of diffraction, limiting their applicability in broadband systems. An alternative achromatic approach is to use refractive beam shapers. πShaper is a field mapping approach where the input intensity profile is transformed into a uniform flat-top distribution through controlled manipulation of the wavefront[25]. The optical layout of the πShaper system is shown in Figure 2.1. This method introduces a predetermined wavefront aberration to achieve the desired energy redistribution, followed by its compensation to preserve the collimated nature of the beam. As a result, the πShaper enables a highly accurate and almost lossless transformation, producing a collimated and speckle-free output beam suitable for high-precision optical applications[26].

Although the πShaper provides precise beam shaping through field mapping, its performance relies heavily on the quality and structure of the input wavefront, typically requiring a well-collimated Gaussian beam for accurate and efficient transformation. In contrast, Köhler illumination, developed by August Köhler of the Carl Zeiss company in 1893, offers a more tolerant and versatile solution for achieving uniform illumination, particularly in microscopy[27]. In this configuration, the image of the light source is focused at the condenser aperture, while the field diaphragm is focused onto the sample plane. This setup ensures that each point in the sample receives light from the entire light source, and each point on the light source illuminates the entire sample uniformly. The schematic layout of the Köhler illumination is illustrated in Figure 2.2. Köhler illumination has been widely used in quantitative imaging, such as fluorescence microscopy[28] and UCNP imaging[29, 30]. Although Köhler illumination is generally considered uniform, it still shows an intensity drop of approximately 10 to 20% towards the edges of the field of view[31]. Better uniformity can be achieved by using only the centre part of the illumination[32]. However, this approach reduces the field of view and the illumination efficiency. To overcome these limitations, the Köhler integrator has been developed. It combines beam homogenisation optics, such as microlens arrays (MLA), with the Köhler configuration to achieve highly uniform and efficient illumination across the entire field of view[33, 34]. In this system, the first MLA splits the incident light into multiple beamlets that are spatially superimposed by the second MLA, producing a homogenised illumination with uniform intensity and angular distribution. The schematic layout of the Köhler integrator is shown in Figure 2.3, where LA_1 and LA_2 represent the first and second microlens arrays, respectively. The parameter p_{LA} represents the pitch of the microlens array, f_{LA1} refers to the focal length of the first microlens array, s indicates the separation between the microlens array and the Fourier lens, and f_{FL} represents the focal length of the Fourier lens. This design enables the coefficient of variation (CV) of the illumination to be reduced to approximately 1.2 to 1.5%, demonstrating excellent homogenisation performance suitable for quantitative imaging applications[35].

Even though uniform illumination is important for widefield imaging, some biophotonics applications use structured illumination to go beyond what conventional widefield imaging can achieve.

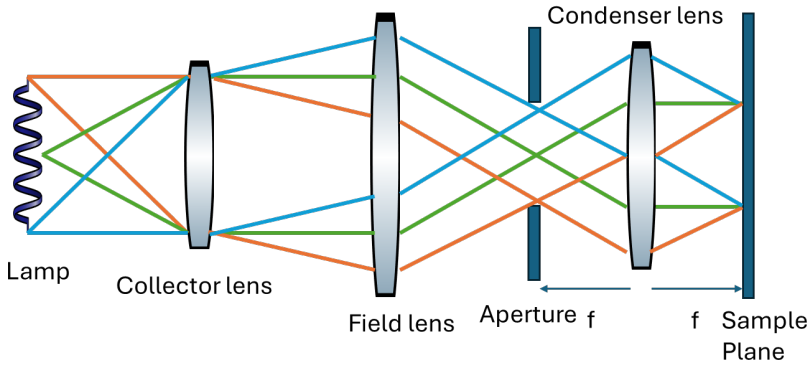

Figure 2.2: Illustration of the Köhler illumination principle

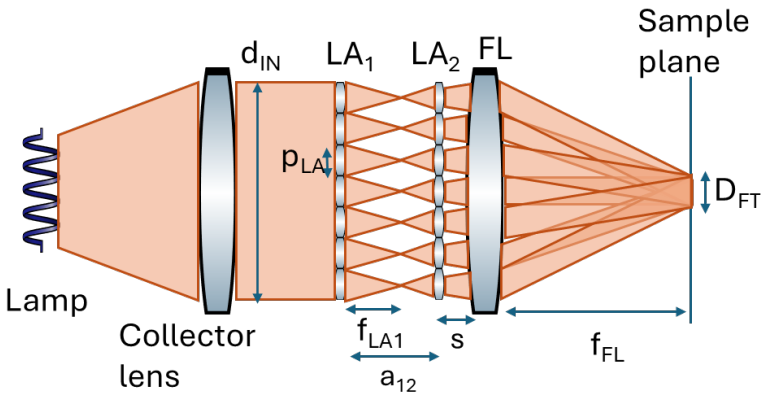

Figure 2.3: Schematic layout of the Köhler integrator

2.2 Structured Illumination Microscopy

2.2.1 Conventional Structured Illumination Microscopy

Structured illumination microscopy (SIM), first proposed by Gustafsson in 2000, is a widefield fluorescence microscopy technique that improves spatial resolution beyond the optical diffraction limit of the conventional microscopy[16, 36]. The principle of SIM is to illuminate the sample with a known spatially modulated light pattern, usually a sinusoidal fringe, which interacts with sub-diffraction features in the sample to generate Moiré fringes. These fringes encode structural details corresponding to high spatial frequencies in the sample in low-frequency signals. By acquiring multiple images with different phase shifts and orientations of the illumination pattern, and applying computational reconstruction algorithms, SIM recovers sub-diffraction spatial details, improves the resolution by a factor of two compared to conventional or confocal microscopy. This enhancement increases the lateral resolution from approximately 290 nm to around 115 nm.

Figure 2.4 illustrates the basic configuration and imaging outcomes of conventional SIM, highlighting its ability to enhance resolution. L_1–L_6 represent the relay and imaging lenses used to guide and focus the illumination and detection paths, QWP indicates the quarter-wave plate used to control the polarisation state of the illumination beam, and DM represents the dichroic mirror that separates the excitation and emission light paths. The generated periodic illumination pattern is projected onto the sample through the objective lens, and the resulting fluorescence signal is collected and recorded by the camera. While conventional SIM effectively improves spatial resolution, various advanced implementations

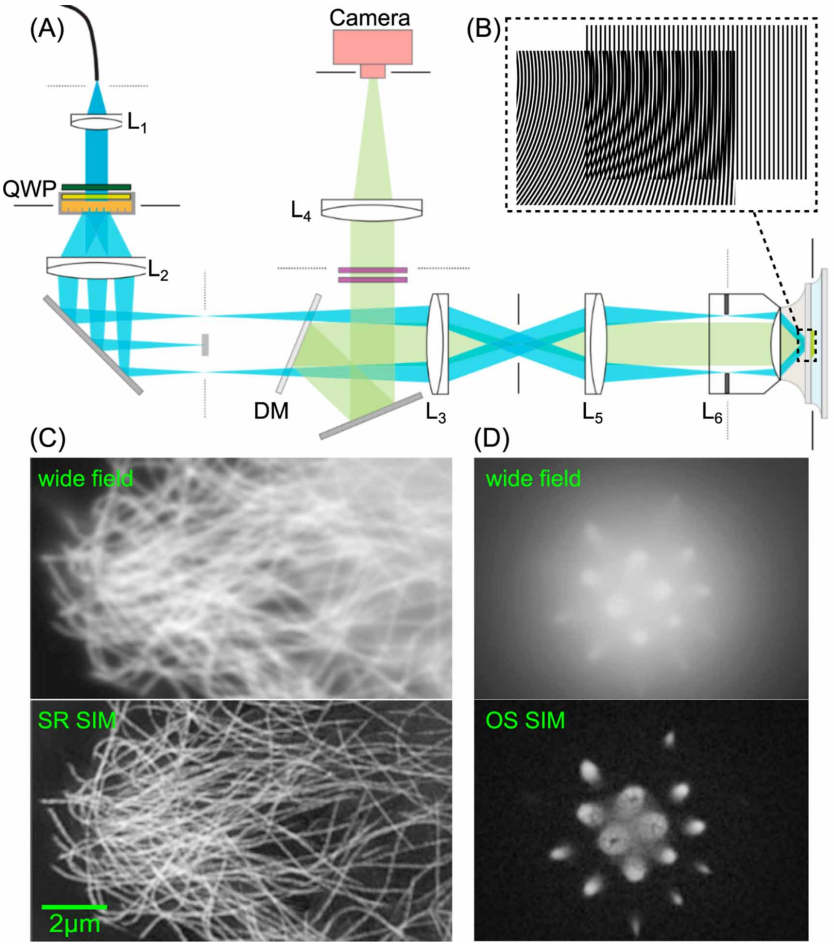

Figure 2.4: The principle, instrumentation, and imaging results of SIM. (A) Schematic layout of SIM. (B) The moiré pattern generated by projecting a periodic pattern on a sample. (C) Comparison of microtubule imaging in HeLa cells using conventional fluorescence microscopy and super-resolution SIM. (D) Comparison of pollen grain images acquired using conventional bright-field microscopy and optical sectioning SIM. The image has been adapted from [37].

have been developed to extend its capabilities.

2.2.2 Total Internal Reflection Fluorescence Structured Illumination Microscopy

Total Internal Reflection Fluorescence Structured Illumination Microscopy (TIRF-SIM) integrates the principles of structured illumination microscopy with total internal reflection fluorescence to achieve high-resolution imaging confined to the region near the membrane of the cell. The evanescent field is generated when excitation light is incident from an optically denser medium, such as a glass coverslip, onto a optically rarer medium, typically an aqueous biological sample, at an angle greater than the critical angle. The evanescent field excites only the region within about 100 nm of the sample above the coverslip, providing excellent optical sectioning. Various optical configurations have been developed to implement TIRF-SIM, including the use of periodically nano-structured substrates[38], SLMs[39], 2D square mesh-grid illumination patterns[40], scanning mirrors combined with Michelson interferometers[41], and acousto-optic deflectors[42]. These diverse approaches broaden the flexibility and applicability of TIRF-SIM for high-

resolution imaging of near-membrane biological processes in live cells.

2.2.3 Nonlinear Structured Illumination Microscopy

The principle of nonlinear SIM further improves the resolution by utilising the nonlinear response of fluorophores to the excitation light. This response generates higher-order harmonics of the illumination pattern, allowing the retrieval of finer structural information. One method to generate higher-order spatial frequencies in structured illumination microscopy (SIM) is through saturated excitation. In this approach, intense patterned illumination induces nonlinear fluorescence, shifting additional high-frequency information into the observable range. This results in higher resolution, achieving up to 50 nm[43]. However, saturated excitation requires high power, which can accelerate photobleaching and cause damage to biological samples. In contrast, reversible photoswitching of a fluorescent protein offers the necessary nonlinearity while using light intensities six orders of magnitude lower than those required for saturation [44].

2.2.4 Spot-scanning Structured Illumination Microscopy

Conventional SIM is a wide-field imaging technique that is often limited to thin samples less than 20 μm. SIM imaging of thick samples is challenged by out-of-focus fluorescence, which contributes to background noise and reduces image quality. The spot-scanning SIM overcomes these issues by using a focused excitation beam which acts as a spot illumination scanned across the sample plane with greater penetration depth[45]. Several spot-scanning SIM modalities have been developed depending on the system configurations. Since point-by-point scanning across the sample plane results in prolonged acquisition times, Multifocal Structured Illumination Microscopy (MSIM) improves imaging speed by using a 2D lattice array of excitation spots to illuminate multiple locations simultaneously. To image the entire field of view, the multifocal excitation pattern is sequentially shifted, and a fluorescence image is acquired after each shift [46–49]. While MSIM requires post-processing to reconstruct the final image, Optical Photon Reassignment Microscopy (OPRA) produces super-resolved images without the need for post-processing. Unlike confocal microscopy, where detection is limited to the excitation focus, OPRA reassigns photons to the point of maximum overlap between excitation and detection probability distributions. Eventally, OPRA eliminates readout noise and reduces artifacts caused by mechanical drift [50, 51].

Apart from the techniques discussed above, plasmonic SIM[52, 53], photonic-chip SIM[54], speckle SIM[55], lattice SIM[56, 57], and 3D SIM[58, 59] have been developed to address specific imaging challenges. To support these modalities, several open source reconstruction algorithms have also been introduced, including fairSIM[60], OpenSIM[61], SIMcheck[62], SIMToolbox[63], and machine learning based reconstruction algorithms[64–66].

2.3 Spatial Frequency Domain Imaging

Optical properties can be characterised using spatial or temporal measurements and analysed in either the real domain or the frequency domain. Spatial Frequency Domain Imaging (SFDI) is a non-contact, widefield optical imaging technique used to quantitatively map tissue optical properties, such as absorption and reduced scattering coefficients. It operates by projecting sinusoidal illumination patterns of

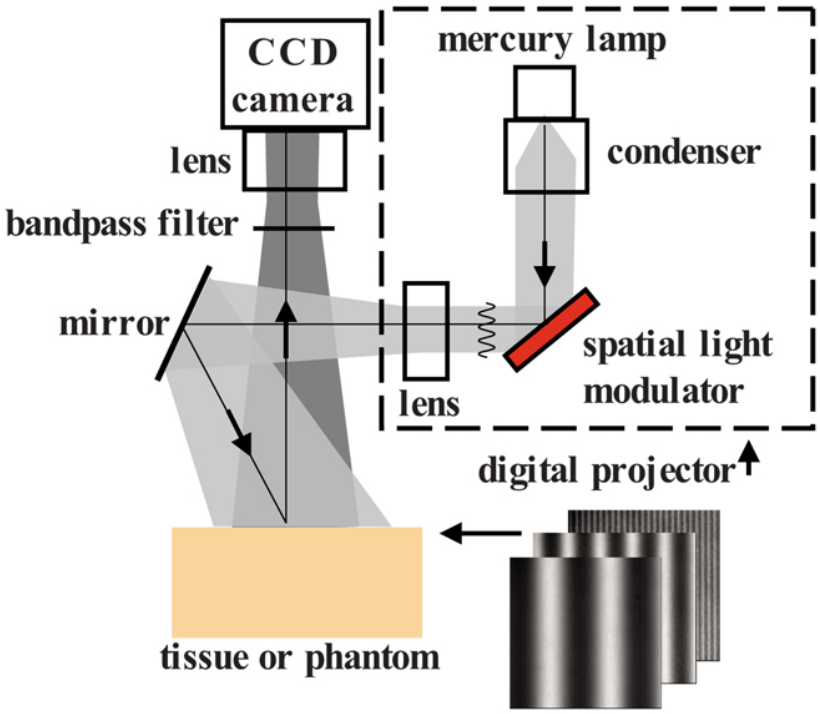

Figure 2.5: Spatial frequency domain imaging setup, adapted from [17].

varying spatial frequencies onto the sample and measuring the diffuse reflectance. The spatial frequency domain models were first applied to analyse Fourier-domain light transport signals by Dögnitz and Wagnières in 1998[67], and Cuccia further developed the approach toward native spatial frequency domain in 2009. Figure 2.5 shows the typical SFDI setup. Reflected intensity images are first acquired under multiple spatially modulated patterns with different spatial frequencies and phases[17]. These images are then demodulated using appropriate algorithms, such as three-phase demodulation[17], Gram-Schmidt orthonormalisation[68], or the spiral phase transform[69], to retrieve diffuse reflectance at each spatial frequency. By fitting the frequency dependent reflectance data to light transport models like the diffusion approximation equation[70] or Monte Carlo simulations[71, 72], and applying inverse parameter estimation methods, such as nonlinear least square fitting[73] or look up table approaches[74, 75], SFDI enables the separation of absorption and scattering effects. Moreover, multispectral and hyperspectral SFDI systems have been developed to enable wavelength dependent chromophores quantification, such as haemoglobin, water, and lipid content[76–78]. SFDI has been widely used in biomedical imaging for burn assessment[79–81], tumor detection[82–84], skin characterisation[85–87], surgical guidance[88, 89], and brain tissue imaging[78, 90, 91]. In addition, SFDI can also be combined with other biophotonics modalities to enhance imaging accuracy and expand functional capability. For example, SFDI can be integrated into fluorescence imaging systems to quantify tissue scattering, thus improving the accuracy of fluorescence signal localisation and quantification[92–94]. Optical Coherence Tomography (OCT) can be integrated with SFDI to complement widefield optical property mapping with high-resolution depth-resolved structural information[95]. SFDI has also been combined with laser speckle imaging to simultaneously measure blood flow, tissue perfusion and oxygenation for burn assessment[96, 97].

2.4 Ring Illumination in Biophotonics

While SIM and SFDI use stripe sinusoidal illumination patterns to enhance resolution or extract optical properties, other advanced techniques utilise alternative beam geometries. For example, STED microscopy and iSORS use ring-shaped illumination. In STED, the ring beam suppresses fluorescence around the excitation centre, enabling sub-diffraction resolution[18]. In iSORS, the ring pattern enhances sensitivity to subsurface Raman signals by spatially separating excitation and collection[19].

2.4.1 Stimulated Emission Depletion Microscopy

Stimulated emission depletion microscopy (STED) is a fluorescence microscopy technique that overcomes the diffraction limit by selectively deactivating fluorophores in the periphery of the focused excitation beam. The concept was first proposed by Stefan Hell and Jan Wichmann in 1994 [18], and the first experimental implementation was demonstrated a few years later by Thomas A. Klar and Stefan Hell in 1999[98, 99]. The process involves two beams: the excitation beam that excites fluorophores within the focal volume to an excited singlet state, the depletion beam, shaped into a doughnut profile, with zero intensity at its centre, stimulates excited fluorophores to return to the ground state via stimulated emission. This approach effectively reduces the point spread function (PSF) of the microscope, enabling the acquisition of images with spatial resolution beyond the diffraction limit. The doughnut-shaped depletion beam is generated using a vortex phase plate to introduce a 2π phase shift to the depletion beam, leading to destructive interference at the focal point, resulting in zero intensity at the centre. The schematic layout and working principle is shown in Figure 2.6. However, this approach is highly sensitive to optical aberrations, which can distort the beam profile and degrade the resolution. In STED microscopy, aberrations can be grouped into two types. The first distorts the depletion beam shape while preserving the central intensity minimum, which may reduce resolution, but still allows some STED enhancement. Severe distortion can break the ring structure, causing the system to behave like a confocal microscope. The second type fills in the central minimum, leading to unwanted depletion of central fluorophores. This results in reduced signal and resolution, similar to confocal imaging but with lower efficiency[100, 101]. To address these limitations, adaptive optics has been introduced to correct aberrations and restore image quality in real time[102, 103]. This is typically implemented in a closed loop configuration, where aberrations are continuously detected and compensated using a combination of a wavefront sensing method and an adaptive optical element, such as an SLM. To speed up the correction process, machine learning approaches are increasingly applied in adaptive optics systems, enabling rapid identification and compensation of aberrations during imaging[104]. Adaptive optics techniques enable effective correction of aberrations introduced by the sample, allowing three dimensional STED imaging at greater depths, reaching up to 164 μm in fixed cells and 76 μm in living cells[105]. Conventional STED microscopy typically achieves a spatial resolution of approximately 15 - 20 nm[106], while the more advanced MINSTED technique can reach 1 - 3 nm by localising single fluorophores through precise steering of the STED doughnut minimum, which serves as a movable reference point for determining the fluorophore's position based on minimal stimulated emission[107].

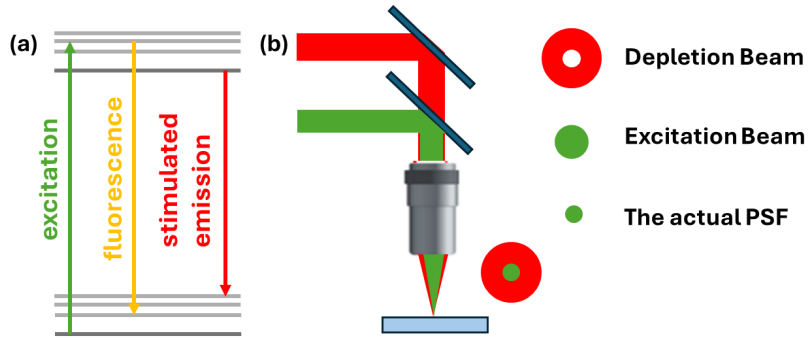

Figure 2.6: (a) Jablonski diagram illustrating the process of excitation, stimulated emission and fluorescence. (b) Schematic layout of a STED microscopy and working principle of smaller PSF in STED microscopy.

2.4.2 Inverse Spatially Offset Raman Spectroscopy

Inverse Spatially Offset Raman Spectroscopy (iSORS), introduced by Pavel Matousek in 2006, enhances subsurface Raman signal detection by using an annular illumination and centralised collection, effectively reducing surface contributions and improving sensitivity to deeper layers in turbid, layered media[19]. Numerous applications across healthcare, pharmaceuticals, and security require the ability to identify analytes through barriers such as packages or biological tissue[108–110]. For example, in medical diagnostics, the overlying fat or skin can obscure featured signals. The presence of overlying barriers has limited the applicability of Raman spectroscopy for probing subsurface features. This limitation was addressed with the development of spatially offset Raman spectroscopy (SORS) by Pavel Matousek in 2005[111]. This configuration introduces a spatial separation between illumination and detection, enables the collection of Raman photons that have migrated from deeper layers within the sample. The spatial offset in SORS can be realised through various configurations, most commonly point-to-point or point-to-ring geometries, where the excitation and collection regions are spatially separated either along a line or across a circular arrangement to improve sensitivity to subsurface Raman signals[112]. For measurements on biological samples, the excitation power must remain below the maximum permissible exposure (MPE) to avoid photodamage. This limitation constrains the strength of the Raman signal achievable with conventional SORS configurations. To overcome this challenge, the iSORS approach has been introduced. It reverses the conventional SORS geometry by using an annular illumination combined with centralised point detection. This configuration enables distributed delivery of optical power across a larger area, thereby reducing local intensity while maintaining effective subsurface signal collection. In iSORS, ring-shaped illumination is typically generated using an axicon lens. Alternative approaches have demonstrated that ring illumination can also be achieved without an axicon by using a multi-mode optical fibre positioned at a non-zero angle relative to the optical axis of a focusing lens. In this setup, the fibre tip produces concentric illumination rings of varying sizes on the sample surface, providing a compact and flexible method for implementing ring illumination[113]. The configuration of illumination and collection in iSORS is illustrated in Figure 2.7. This technique has shown strong potential in biomedical applications, particularly for non-invasive bone characterisation[114]. Its depth sensitivity can be further enhanced by incorporating surface-enhanced Raman scattering (SERS) techniques, allowing more effective detection of biochemical markers in bone and other tissues[115].

Figure 2.7: Illumination and collection configuration of iSORS

2.5 Transmission Matrix and Beamshaping

Beam shaping through scattering media has become an essential tool in biomedical optics, enabling precise light control even in highly diffusive environments. It was first demonstrated by Vellekoop and Mosk in 2007 to focus coherent light through an opaque scattering medium by shaping the incident wavefront with an SLM[116]. A key approach to manipulating light in complex environments is through the transmission matrix, which characterises the relationship between input and output fields in an optical system. Measuring the transmission matrix allows for precise control of the incident wavefront, enabling the transmitted light to be shaped into a specific pattern, even after passing through complex or disordered media. The first experimental method for measuring the optical transmission matrix was developed by Sébastien M. Popoff in 2010 [117]. The transmission matrix is typically acquired by sequentially illuminating the system with a set of known input patterns, such as plane waves or Hadamard bases, and recording the corresponding complex output fields using an interferometric technique. Once the transmission matrix has been acquired, it can be used to shape the output wavefront, enabling precise control of beam propagation through scattering media[118, 119]. Techniques including phase conjugation, singular value decomposition and eigenmode selection have been applied to shape the beam.

While conventional wavefront shaping relies on modulating the incident light using devices such as SLM or digital micromirror devices (DMD), recent research has introduced an alternative approach to manipulate the transmission matrix by applying controlled local bends along the fibre using piezoelectric actuators. This approach provides a significantly larger number of degrees of control, offering greater versatility for complex beam shaping applications[120].

Full-field control through conventional transmission matrix techniques usually requires phase retrieval using holographical methods, which complicates the optical system and reduces its stability. To overcome this, machine learning approaches have been explored to enable reference-arm-free TM estimation using intensity-only data[121–123]. While deep learning has enabled image retrieval through MMFs without phase information, these methods often require large training datasets, iterative optimisation, and long computation times, limiting their practicality. As an alternative, Bayesian phase retrieval algorithms have been proposed to reconstruct the complex TM from noisy intensity-only measurements in a reference-free setup. These methods provide reliable TM estimation with moderate computational cost and can be parallelised for speed, making them attractive for practical applications[124]. To further simplify the system, a real-valued intensity transmission matrix (RVITM) approach has been introduced. This approach assumes a pseudo-linear relationship between input and output intensities. This enables fast and robust multimode fibre (MMF) characterisation without iterative processing or large datasets, offering a practical solution for applications that do not require phase information[125].

Beam shaping through multimode fibre has been widely used in imaging, spectroscopy, and microfabrication. In imaging, wavefront shaping enables high-resolution fluorescence and reflectance endoscopy through MMFs, allowing access to delicate tissues such as the brain without mechanical scanning[126–128]. Beam shaping also facilitates the generation of high-energy, temporally focused pulses for microfabrication applications[129]. Moreover, beam shaping through multimode fibres has enabled the implementation of three-dimensional optical tweezers and the generation of customised optical force fields for advanced optical trapping applications[130, 131].

The development of structured illumination and beam shaping techniques has significantly improved the performance of optical imaging and spectroscopy in biophotonics. The transition from conventional Gaussian illumination to structured light patterns such as top-hat, sinusoidal fringes, and ring illumination has overcome limitations in spatial resolution, depth sensitivity, and uniformity. This chapter has outlined the state of the art in structured illumination and light manipulation techniques within biophotonics. Building on this foundation, the following chapters will explore how these approaches are applied to push the boundaries of optical imaging and spectroscopy, enabling new capabilities in biomedical applications in my research.

Chapter 3

Transmission matrix and beamshaping

Light manipulation and engineering are important to enhance the sensitivity in optical detection systems. Optical components such as lenses, fibres, and scattering media can be understood as systems that transform input optical fields into output fields. In the linear regime, where the response of the medium is independent of the light intensity, this transformation can be fully described by a transmission matrix (TM). The TM framework enables precise control and shaping of light through complex media, which is essential for applications in sensitive optical measurements. In this chapter, I provide an overview of the TM approach as applied to scattering materials, covering its theoretical foundations, experimental implementation, and relevance to light shaping through multimode fibres (MMFs) for biomedical applications. These concepts form the basis for Paper **IV**, where the TM framework was employed to realise structured illumination at the distal end of an MMF for biomedical applications.

3.1 Theoretical Background

In a perfectly homogeneous medium, electromagnetic waves propagate in a predictable manner according to their wave equations, with minimal scattering or distortion. However, in disordered materials such as biological tissue or MMFs, spatial inhomogeneities on the scale of the wavelength give rise to multiple scattering events. These interactions produce complex interference patterns at the output, which can be described by the transmission matrix K:

$$E_m^{\text{out}} = \sum_n k_{mn} E_n^{\text{in}}, \tag{3.1}$$

where $\mathbf{E}_{\text{in}}$ and $\mathbf{E}_{\text{out}}$ are the complex-valued input and output optical fields, respectively. The element $k_{mn} \in \mathbb{C}$ denotes the complex transmission coefficient that links the n-th input mode to the m-th output mode, while E_n^{in} represents the complex amplitude—including both magnitude and phase—of the input field in the n-th mode.

The TM can be used to calculate an optimal input wavefront that focuses light at a target output mode E_{target}. Assuming full knowledge of K, the ideal input field under phase conjugation is given by:

$$E_{\text{in}} = K^\dagger E_{\text{target}}, \tag{3.2}$$

where $K^\dagger$ is the Hermitian transpose of the TM. The resulting output field is:

$$E_{\text{eff}} = K K^\dagger E_{\text{target}} = \mathcal{O}_{\text{foc}} E_{\text{target}}, \tag{3.3}$$

where $\mathcal{O}_{\text{foc}}$ is the time-reversal operator.

3.2 Experimental Setup

This section introduces two commonly used experimental configurations for measuring the TM of a scattering medium: one that enables full phase and amplitude retrieval using interferometric detection, and another that relies only on intensity measurements. Both approaches use SLMs for input wavefront control and camera-based detection for measuring the output field.

3.2.1 Phase Measurement Using Interferometric Detection

A phase-sensitive transmission matrix measurement can be achieved using an interferometric approach that reconstructs the complex optical field transmitted through the scattering medium. This method was first demonstrated by S. M. Popoff[117], and has since become a widely adopted technique due to its ability to recover both amplitude and phase components of the TM.

The input wavefront is structured using a Hadamard pattern, which offers orthogonality, binary values, and improved SNR compared to pixel-by-pixel modulation. A coherent laser source is expanded and directed onto an SLM. The polarisation configuration is optimised to ensure that the SLM operates predominantly in a phase-modulation regime, allowing for a full 2π phase shift while maintaining minimal amplitude modulation. A reference beam can be generated by introducing a reference arm[132] or keep part of SLM static[117]. The experimental setup is shown in Figure 3.1.

The modulated beam is shined onto a strongly scattering medium, and the transmitted speckle is collected and measured by a CCD camera using a high-numerical-aperture objective. The output field is reconstructed using a four-phase phase-shifting interferometry method. For each input pattern, four intensity images are recorded with relative phase delays of $\phi = 0, \pi/2, \pi, 3\pi/2$. For the setup with a reference arm, the complex field at the output mode m for a given input mode n is extracted from:

$$k_{mn} = \frac{1}{4}\left(I_m^{(0)} - I_m^{(\pi)}\right) + i\frac{1}{4}\left(I_m^{(3\pi/2)} - I_m^{(\pi/2)}\right), \tag{3.4}$$

where k_{mn} is the complex transmission coefficient relating the input mode n to the output mode m.

If the unmodulated part of the SLM is used as the reference, a constant is added to the TM:

$$s_m k_{mn} = \frac{1}{4}\left(I_m^{(0)} - I_m^{(\pi)}\right) + i\frac{1}{4}\left(I_m^{(3\pi/2)} - I_m^{(\pi/2)}\right), \tag{3.5}$$

where s_m is the complex amplitude of the static reference field at the m-th output mode. This procedure is repeated for all input modes.

3.2.2 Real-Valued Intensity Transmission Matrix Measurement

In addition to full complex TM reconstruction, a simplified representation known as the real-valued intensity transmission matrix (RVITM) can be used to describe the input-output behaviour of a scattering medium[125]. The RVITM models the intensity response of the system under intensity-only modulation and is particularly relevant in applications where phase modulation is not available or not required.

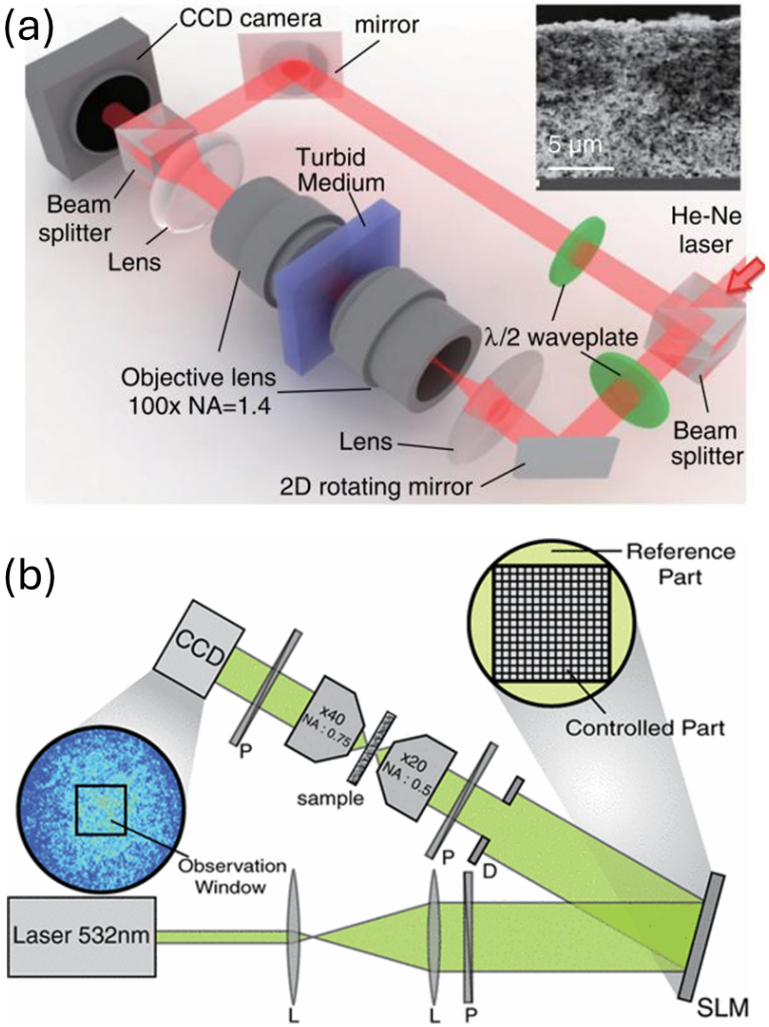

Figure 3.1: Schematic layout of the transmission matrix measurement setup (a) with reference arm[132] (b) with static SLM part[117].

Light from a laser source was collimated and modulated using a digital micromirror device (DMD) to project binary patterns. The patterned light was then focused onto the scattering material. The scattered light was collected and imaged by a camera.

In the characterisation step, a Hadamard matrix $\mathbf{H} \in \{-1, +1\}^{N \times N}$ was used to construct binary input patterns. Since the DMD supports only binary modulation between `0` and `1`, each column of $\mathbf{H}$ was converted into two binary matrices using:

$$\mathbf{H}_1 = \frac{\mathbf{H} + 1}{2}, \quad \mathbf{H}_2 = \frac{-\mathbf{H} + 1}{2}. \tag{3.6}$$

Each column of the concatenated matrix $[\mathbf{H}_1, \mathbf{H}_2]$ was reshaped into a square binary pattern and projected onto the sample using the DMD, resulting in $2N$ binary Hadamard patterns. The intensities of the corresponding output speckles were recorded by a camera and assembled into a measurement matrix. The RVITM links the input and output intensities through the relationship:

$$\begin{bmatrix} I_{11} & \cdots & I_{p1} \\ \vdots & \ddots & \vdots \\ I_{1m} & \cdots & I_{pm} \end{bmatrix} = \mathrm{RVITM} \cdot \begin{bmatrix} \mathbf{H}_1 & \mathbf{H}_2 \end{bmatrix}, \tag{3.7}$$

where I_{pm} represents the intensity at the m-th pixel in the p-th output speckle pattern. Since the first Hadamard pattern corresponds to all micromirrors switched "ON", the formulation can be transformed into:

$$\begin{bmatrix} 2I_{11} - I_{11} & \cdots & 2I_{p1} - I_{11} \\ \vdots & \ddots & \vdots \\ 2I_{1m} - I_{1m} & \cdots & 2I_{pm} - I_{1m} \end{bmatrix} = \mathrm{RVITM} \cdot \begin{bmatrix} 2\mathbf{H}_1 - 1 & 2\mathbf{H}_2 - 1 \end{bmatrix} = \mathrm{RVITM} \cdot \begin{bmatrix} \mathbf{H} & -\mathbf{H} \end{bmatrix}. \tag{3.8}$$

Owing to the orthogonality of the Hadamard matrix, the RVITM can be calculated as:

$$\mathrm{RVITM} = \begin{bmatrix} 2I_{11} - I_{11} & \cdots & 2I_{p1} - I_{11} \\ \vdots & \ddots & \vdots \\ 2I_{1m} - I_{1m} & \cdots & 2I_{pm} - I_{1m} \end{bmatrix} \cdot \begin{bmatrix} \mathbf{H} & -\mathbf{H} \end{bmatrix}^{\top}, \tag{3.9}$$

where the transpose of $[\mathbf{H}, -\mathbf{H}]$ equals its inverse due to the Hadamard matrix properties.

The image retrieval from a new output speckle intensity pattern $\mathbf{I}_{\mathrm{out}}$ can be achieved using the pseudo-inverse of the RVITM:

$$\mathbf{I}_{\mathrm{image}} = \mathrm{RVITM}^{+} \cdot \mathbf{I}_{\mathrm{out}} \approx \mathbf{I}_{\mathrm{in}}, \tag{3.10}$$

where $\mathbf{I}_{\mathrm{image}}$ is the reconstructed input intensity distribution and RVITM^{+} is the Moore–Penrose pseudo-inverse.

3.3 RVITM Based Beamshaping for Biomedical Applications

In addition to image reconstruction through multimode fibres, the RVITM provides a practical framework for intensity-only beam shaping through MMFs. Unlike conventional methods that rely on phase sensitive transmission matrix and interferometric setups, RVITM based beam shaping operates only on intensity measurements, significantly simplifying the optical system. Since no phase stability or reference arm is required, the system maintains functional performance even in dynamic environments such as handheld probes, flexible catheters, or during patient motion. How this robust and compact configuration can be applied to iSORS is explained in Paper **IV**.

The concepts of transmission matrix and beam shaping presented in this chapter form the optical control foundation for the inverse spatially offset Raman spectroscopy (iSORS) system developed in this work. While these methods define how light can be precisely manipulated to achieve the desired illumination profiles and detection geometries, their full potential is realised when applied to specific biophotonics techniques. Therefore, the next chapter introduces the modalities applied throughout this thesis, including upconversion nanoparticle imaging, Raman spectroscopy, diffuse reflectance spectroscopy, and pulse oximetry, along with the Monte Carlo simulations used to model light–tissue interactions.

Chapter 4

Concepts of biophotonics modalities for tissue diagnostics

This chapter introduces key biophotonics modalities used for noninvasive tissue diagnostics, with a focus on upconverting nanoparticles, Raman spectroscopy, diffuse optics, and pulse oximetry, along with Monte Carlo simulation as a modelling approach for analysing light–tissue interactions in these techniques. Upconverting nanoparticles (UCNPs) serve as advanced luminescent biomarkers that convert near-infrared excitation into visible emission, enabling high-contrast, deep tissue imaging with minimal background interference. Raman spectroscopy provides label-free molecular characterisation based on vibrational signatures, offering high specificity for detecting biological or biochemical changes. Diffuse optical methods, particularly near-infrared spectroscopy, quantify tissue properties by modelling light scattering and absorption. Pulse oximetry, a widely used clinical technique, determines arterial oxygen saturation based on the distinct absorption spectra of oxygenated and deoxygenated haemoglobin. Monte Carlo simulation, a statistical technique for modelling photon transport in scattering media, enables realistic predictions of light–tissue interactions in complex geometries. These modalities provide the foundational context in which illumination manipulation is applied for sensitive tissue diagnostics, forming the basis for the light engineering strategies developed in this thesis.

4.1 Upconverting Nanoparticles

Upconverting nanoparticles (UCNPs) are a class of luminescent nanomaterials that convert low-energy excitation into higher-energy emission through nonlinear optical processes. Owing to their sharp emission peaks, high photostability, deep tissue penetration under NIR excitation, and minimal autofluorescence, UCNPs have emerged as promising contrast agents in biomedical imaging and sensing. This section provides an overview of the fundamental principles of upconversion process, material composition of UCNPs, and their advantages in biomedical applications.

4.1.1 Upconversion Process

Photo upconversion is a nonlinear optical process in which two or more incident photons of relatively low energy are absorbed and converted into one single photon with higher energy. Five fundamental upconversion mechanisms have been identified: excited state absorption (ESA), energy transfer upconversion (ETU), cooperative sensitisation upconver-

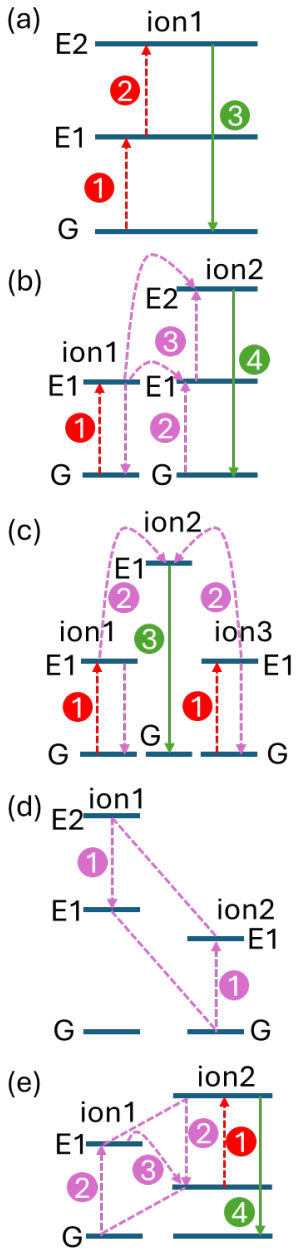

Figure 4.1: Principle of upconversion process: (a) excited-state absorption (ESA), (b) energy transfer upconversion (ETU), (c) cooperative sensitization upconversion (CSU), (d) cross relaxation (CR), and (e) photon avalanche (PA).

sion (CSU), cross relaxation (CR), and photon avalanche (PA)[133]. The upconversion process is illustrated in Figure 4.1.

Excited State Absorption

Excited state absorption (ESA) occurs when a single ion sequentially absorbs two pump photons via a ladder-like energy level structure. This process relies on equal or near-equal energy gaps between the ground state (G) and the intermediate state (E1), and between E1 and the higher excited state (E2), as well as the relatively long lifetime of the E1 state, which serves as an energy reservoir. Once the ion is excited to E1, the extended lifetime allows for the absorption of a second photon, promoting the ion to E2 before it relaxes back to the ground state. As a result, emission of upconverted photons occurs from the E2 level. Efficient ESA requires a well aligned ladder-like energy level structure, and only a few lanthanide ions have such energy level structures such as Er^{3+}, Ho^{3+}, Tm^{3+}, and Nd^{3+}[134]. These ions also benefit from absorption bands at wavelengths corresponding to commercially available near-infrared laser sources (e.g., 975 nm or 808 nm), making them particularly useful for upconversion applications. ESA occurs entirely within a single ion and does not require high dopant concentrations. However, its relatively low efficiency due to weak excited-state absorption cross sections.

Energy Transfer Upconversion

While ESA occurs entirely within a single ion, energy transfer upconversion (ETU) requires two neighbouring ions. In an ETU process, the sensitiser ion (ion 1) is excited from its ground state to a metastable level E1 by absorbing a pump photon. It subsequently transfers the excitation energy to a neighbouring activator ion (ion 2), first exciting it from the ground state to an intermediate state E1, and then from the intermediate state to a higher-energy emitting level E2, while the sensitiser ion returns to the ground state after each energy transfer step. Since energy exchange in ETU occurs through dipole–dipole interactions, its efficiency is highly dependent on the average distance between sensitiser and activator ions, which is determined by dopant concentration.

Cooperative Sensitisation Upconversion

Cooperative sensitisation upconversion (CSU) involves the interaction of three ions, with ion 1 and ion 3 typically being of the same type. After absorbing excitation photons, both ion 1 and ion 3 are excited to the excited state, and subsequently cooperate to simultaneously transfer their energy to a nearby ion 2, and excite ion 2 to the excited state. Ion 2 then relaxes to the ground state, emitting an upconverted photon. The efficiency of CSU is significantly lower than that of ESA or ETU, as it involves quasi-virtual intermediate states that require higher-order quantum mechanical perturbation theory to describe the energy transfer process.

Cross Relaxation

Cross relaxation (CR) is an energy transfer process that results from ion–ion interactions, where an excited ion (ion 1) transfers part of its energy to a neighbouring ion (ion 2) through the transition: E2 (ion 1) + G (ion 2) $\rightarrow$ E1 (ion 1) + E1 (ion 2). Since the CR process results from ion-ion interaction, the efficiency strongly depends on the dopant concentration.

Photon Avalanche

Photon avalanche (PA) is an upconversion process that occurs only above a specific excitation power threshold. Below this threshold, upconverted fluorescence is minimal, but once exceeded, the photoluminescence intensity increases by orders of magnitude. PA involves a feedback loop combining excited-state absorption (ESA) and cross-relaxation (CR). Initially, the metastable level E1 of ion 2 is weakly populated through non-resonant ground-state absorption. ESA then excites ion 2 from E1 to the emitting state E2. An efficient CR process between ion 1 and ion 2 follows, after which ion 1 transfers its energy to ion 2, repopulating its E1 level and completing the feedback loop.

4.1.2 Material Composition

The optical performance of UCNPs is largely determined by their material composition. UCNPs typically consist of a host lattice doped with sensitiser and activator lanthanide ions. The host provides a low-phonon environment for efficient energy transfer, while dopants define the excitation and emission characteristics[133, 135, 136].

Host Materials

The selection of host materials is critical for achieving high-efficiency upconversion emission. An ideal host should be optically transparent in the spectral region of interest, chemically stable, and have a high threshold for optical damage. The host lattice affects the upconversion efficiency in two ways: phonon dynamics and local crystal field. Non-radiative multiphonon relaxations, which convert electronic excitation energy into lattice phonons, are the major loss mechanism in upconversion process. Fluorides, particularly $NaYF_4$, are the most effective hosts due to their low phonon cutoff energy ($\sim 350\,\mathrm{cm}^{-1}$) and high chemical stability[137]. In contrast, oxides and vanadates have higher phonon energies ($> 500\,\mathrm{cm}^{-1}$), which increase multiphonon relaxation and reduce the upconversion efficiency[138, 139]. In addition to phonon energy, the local crystal field environment of the dopant ions strongly affects the upconversion performance. A less symmetric crystal phase is generally favourable for upconversion efficiency, as it has stronger intermixing between the 4f states of the lanthanide ion and higher electronic configurations, thereby increasing optical transition probabilities.

Dopants

Upconversion emissions are theoretically possible from most rare earth ions, but under low excitation power, only a few such as Er^{3+}, Ho^{3+}, and Tm^{3+} produce efficient upconversion due to their ladder like energy levels and spectral compatibility with commercial diode lasers. Among them, Tm^{3+} ions emit strongly in the near infrared around 800 nm. This emission falls within the biological optical window, where tissue absorption and scattering are minimal, making Tm^{3+} doped UCNPs particularly attractive for deep tissue bioimaging. The doping concentration of activators is generally kept low (typically below 2 mol%) to reduce cross-relaxation energy losses. Single-doped nanoparticles often have relatively low upconversion efficiency due to the difficulty in balancing reduced quenching at low activator concentrations with sufficient pump energy absorption at higher concentrations. To improve luminescence efficiency, sensitisers with large absorption cross-sections in the near-infrared region are commonly co-doped with activators. Typical direct sensitisers include Yb^{3+}, which is the most widely used due to its strong absorption around 980 nm [140], as well as Nd^{3+} and Er^{3+}, which can enable

excitation at alternative wavelengths such as 808 nm [141]. Efficient energy transfer between the sensitiser and activator is required to achieve strong upconversion emission. In addition to these direct sensitisers, indirect sensitisers such as Ce^{3+} and Mn^{2+} can be introduced to modulate energy transfer pathways and selectively enhance specific emission bands [133].

4.1.3 Advantages for Biomedical Applications

UCNPs offer several advantages over conventional fluorescent biomarkers that make them highly attractive for bioimaging and sensing. First, they are excited by NIR light rather than ultraviolet radiation, which significantly reduces photo damage to biological tissue and increases the penetration depth. Additionally, the anti-Stokes emission nature eliminates background autofluorescence, resulting in a high SNR and improved detection sensitivity. Unlike other anti-Stokes processes such as second-harmonic generation, multi-photon absorption or anti-Stokes Raman scattering, upconversion are based on real, long lived intermediate states within the lanthanide ion. This enables efficient frequency conversion at the moderate light intensities that are suitable for biological samples and can be achieved using compact and cost-effective diode lasers. UCNPs also have exceptional photostability: they do not blink under continuous excitation, resist photobleaching and are chemically robust. Their emission lines are narrow and well defined, they display a large anti-Stokes shift, and their output colour can be tuned simply by adjusting dopant composition or excitation wavelength[142]. Surface functionalised UCNPs can act as nanocarriers and fluorescent tags for drugs and biomolecules[143–145]. By attaching antibodies, peptides, or other ligands, they selectively target tumour cells, enabling precise imaging and combined diagnostic and therapeutic applications. These properties allow UCNPs to provide specific, high-contrast, and long-lasting imaging of targets deep within biological tissue.

4.2 Raman Spectroscopy

Raman spectroscopy is a vibrational spectroscopic technique that provides molecular specific information based on the inelastic scattering of photons. Raman spectroscopy enables non-invasive, label-free characterisation of biological tissues by probing their biochemical composition with high specificity. This section introduces the fundamental principles of Raman scattering, categorises the spectral regions of interest and their biomedical significance, and introduces key advancements that enhance depth sensitivity and selectivity, including Spatially Offset Raman Spectroscopy (SORS), inverse SORS (iSORS), and Dual Wavelength Raman Spectroscopy. These techniques expand the capability of Raman spectroscopy for deep-tissue analysis and clinical translation.

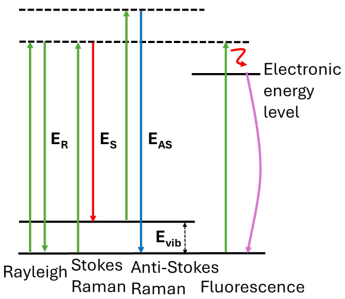

Figure 4.2: Different types of light matter interactions.

4.2.1 Fundamentals of Raman Scattering

Raman spectroscopy is a vibrational spectroscopic technique based on the inelastic scattering of photons, a process known as the Raman effect. This phenomenon was first observed in 1928 by an Indian physicist Chandrashekhara Venkata Raman, who discovered that when monochromatic light interacts with a material, a small portion of the scattered light undergoes a frequency shift due to energy exchange with molecular vibrations. This inelastic scattering reveals detailed information about molecular structures, enabling non destructive and label free analysis.

When light encounters a sample, several interactions can occur, as illustrated in Figure 4.2. Some light may be reflected directly from the

surface through reflection, or it may be elastically scattered without a change in energy, known as Rayleigh scattering. If the energy of the incoming photons matches an electronic transition of a molecule, resonant excitation can occur, followed by relaxation through the emission of a photon at a longer wavelength, a process called fluorescence. Raman inelastic scattering occurs when incident photons interact with molecular vibrations, leading to an inelastic exchange of energy[146, 147]. In Stokes Raman scattering, the molecule absorbs energy from the photon, leading to a scattered photon with lower energy and a longer wavelength than the incident light. The photon energy is given by:

$$E_{\text{Stokes}} = h(\nu_0 - \nu_v) \tag{4.1}$$

where ν_0 is the frequency of the incident light, ν_v is the vibrational frequency of the molecule, and h is Planck's constant. If the molecule is already in a vibrationally excited state, it can transfer energy to the photon during relaxation, resulting in anti-Stokes scattering, where the scattered photon has higher energy and a shorter wavelength:

$$E_{\text{anti-Stokes}} = h(\nu_0 + \nu_v) \tag{4.2}$$

The difference between the incident and scattered photon energies corresponds to a specific vibrational mode of the molecule. This energy shift is commonly expressed as the Raman shift in wavenumber units (cm^{-1}):

$$\Delta\tilde{\nu} = (\frac{1}{\lambda_0} - \frac{1}{\lambda_s}) * 10^7 \tag{4.3}$$

where λ_0 and λ_s are the wavelengths of the incident and scattered light in nm, respectively. Since molecular vibrations are highly specific to chemical bonds and molecular symmetry, the Raman spectrum provides a unique molecular fingerprint of the sample.

The intensity of the anti-Stokes scattering is typically weaker than that of the Stokes line because the population of vibrationally excited states follows the Boltzmann distribution. The intensity ratio between anti-Stokes and Stokes scattering is given by:

$$\frac{I_{\text{anti-Stokes}}}{I_{\text{Stokes}}} \propto \exp\left(-\frac{h\nu_v}{k_B T}\right) \tag{4.4}$$

where k_B is Boltzmann's constant and T is the absolute temperature. This relationship allows Raman spectroscopy to be applied for temperature measurements at microscopic scales[148].

In classical mechanics, Raman scattering arises from the interaction of the incident light's electric field with the molecule's polarisability. The electric field of the incident light is expressed as:

$$E(t) = E_0 \cos(2\pi\nu_0 t) \tag{4.5}$$

and induces a dipole moment P:

$$P = \alpha E \tag{4.6}$$

where P is the induced dipole moment and α is the molecular polarisability.

The vibrational motion of the molecule can be described as:

$$Q = Q_0 \cos(2\pi\nu_n t) \tag{4.7}$$

where Q is the vibrational displacement, Q_0 is the amplitude of vibration, and ν_n is the vibrational frequency of the mode.

As the molecule vibrates, its polarisability α changes periodically with Q. This variation can be expressed as a Taylor expansion about the equilibrium position:

$$\alpha = \alpha_0 + \left(\frac{\partial \alpha}{\partial Q}\right) Q + higher\ term \tag{4.8}$$

where α_0 is the equilibrium polarisability, and $\left(\frac{\partial \alpha}{\partial Q}\right)$ is the rate of change of polarisability with respect to the vibrational coordinate.

Substituting the expressions for α, Q, and E into the dipole moment gives:

$$P = \left[\alpha_0 + \left(\frac{\partial \alpha}{\partial Q}\right) Q_0 \cos(2\pi\nu_n t)\right] E_0 \cos(2\pi\nu_0 t) \tag{4.9}$$

$$= \alpha_0 E_0 \cos(2\pi\nu_0 t) + \left(\frac{\partial \alpha}{\partial Q}\right) Q_0 E_0 \cos(2\pi\nu_0 t)\cos(2\pi\nu_n t) \tag{4.10}$$

This can be further expanded as:

$$P = \alpha_0 E_0 \cos(2\pi\nu_0 t) + \frac{1}{2}\left(\frac{\partial \alpha}{\partial Q}\right) Q_0 E_0 \left[\cos 2\pi(\nu_0 + \nu_n)t + \cos 2\pi(\nu_0 - \nu_n)t\right] \tag{4.11}$$

Where, the first term corresponds to Rayleigh scattering at the original frequency ν_0. The second term corresponds to anti-Stokes scattering at frequency $\nu_0 + \nu_n$, and the third term to Stokes scattering at frequency $\nu_0 - \nu_n$.

For a vibrational mode to be Raman active, the polarisability must change during the vibration. This condition is written as:

$$\left(\frac{\partial \alpha}{\partial Q}\right) \neq 0 \tag{4.12}$$

The efficiency of Raman scattering is described by the Raman cross-section:

$$\sigma_R \propto (\nu_0 - \Delta\nu)^4 \left(\frac{\partial \alpha}{\partial Q}\right)^2 \tag{4.13}$$

where σ_R is the Raman scattering cross-section, and $(\nu_0 - \Delta\nu)^4$ reflects the strong dependence on the frequency of the scattered light.

The overall Raman signal intensity is given by:

$$I_R = K I_0 \sigma_R C V \tag{4.14}$$

where I_R is the Raman intensity, I_0 is the incident laser power, C is the molecular concentration, V is the scattering volume, and K is a constant depending on the collection geometry and instrument configuration.

In conclusion, Raman spectroscopy explores molecular vibrations by detecting the inelastic scattering of photons. Although the likelihood of this interaction is low, occurring in only one out of every 10^6, the technique offers highly specific insights into molecular structure. Its ability to work effectively with water-based samples and its non-invasive characteristics make it particularly suitable for biomedical uses, such as tissue diagnostics and *in vivo* chemical sensing.

4.2.2 Raman Spectral Regions and Biomedical Relevance

The Raman spectrum of biological samples contains rich molecular information that varies across specific wavenumber regions, each associated with characteristic vibrational modes of biomolecules. In biomedical Raman spectroscopy, two spectral windows are of particular importance:

the fingerprint region (approximately 400 to 1800 cm^{-1}) and the high wavenumber region (2800 to 3800 cm^{-1}).

The fingerprint region is so named because it contains numerous sharp and molecule-specific peaks corresponding to fundamental vibrational modes of proteins, lipids, nucleic acids, and carbohydrates. Key features include the amide I band (1650 cm^{-1}) and amide III around 1250 cm^{-1}, both arising from peptide backbone vibrations. The spectral range between 800 and 1100 cm^{-1} contains contributions from phosphodiester backbone vibrations of DNA and RNA. Bands due to C–C stretch, C=C stretch, and C–H bending modes are typically observed throughout this region and are particularly useful for characterising lipid, protein and carbohydrate content [149, 150]. Owing to its high chemical specificity, the fingerprint region is widely used for diagnostic applications, tissue classification, and biochemical phenotyping.

The high wavenumber region, spanning from approximately 2800 to 3800 cm^{-1}, is dominated by C–H, N–H, and O–H stretching vibrations. Although it generally exhibits broader and less distinct bands compared to the fingerprint region, it provides valuable insight into lipid chain organisation, protein content, and the hydration state of tissues [151, 152].The broad O-H stretching vibration band (3000-3800 cm^{-1}) is highly sensitive to hydrogen bonding. This allows researchers to differentiate between the spectral signatures of bound water and free/bulk water. This sensitivity makes the high wavenumber region especially powerful for studying hydration dynamics, biomolecular interactions, and the aqueous environments of live cells. .

Together, these spectral regions enable comprehensive molecular profiling in biomedical contexts. The fingerprint region offers highly resolved biochemical specificity, while the high wavenumber region provides robust contrast related to hydration and lipid content. In applications such as cancer detection, inflammation monitoring, and metabolic assessment, the combined use of both spectral windows enhances diagnostic performance.

4.2.3 Spatially Offset Raman Spectroscopy (SORS)

Spatially Offset Raman Spectroscopy (SORS) is a technique that enables the recovery of Raman signals from subsurface layers of diffusely scattering media by collecting scattered light at a lateral distance from the point of laser illumination. In conventional Raman measurements, signal collection is typically limited to superficial regions due to the dominance of photons scattered near the surface. The spatial offset allows deeper tissue signals to be detected while suppressing surface-dominated spectra. By collecting the Raman signal at increasing spatial offsets, contributions from deeper layers become more prominent relative to the top layer, enabling analysis of subsurface components[111].

Two prevalent collection geometries utilised in SORS implementations are as follows: (1) Point Source-Point Collection Configuration: In this configuration, both the excitation and collection points are discrete and spatially separated. This arrangement facilitates depth-resolved measurements by varying the offset distance between the two points allowing the interrogation of subsurface layers within a turbid medium. (2) Point Source-Ring Collection Configuration: This setup features a single central excitation point surrounded by a circular array of collection fibers. This geometry enables simultaneous acquisition of Raman signals from multiple equidistant points, which significantly enhances the quality of the collected signal by improving the signal-to-noise ratio. The advantages of this configuration are particularly relevant in applications requiring high sensitivity and depth profiling such as biomedicine.[153]. These two configurations are shown in Figure 4.3.

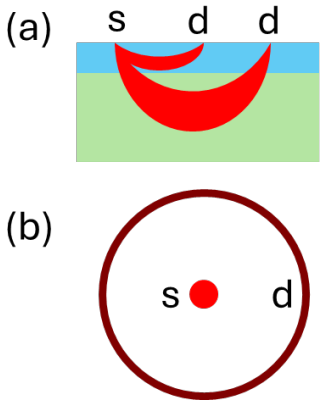

Figure 4.3: (a) Point source point collection. (b) Point source ring collection. s: source, d: detector.

SORS provides a non-destructive and label-free method to access molecular information beneath the surface of biological samples, expanding the diagnostic potential of Raman spectroscopy in clinical applications.

4.2.4 Inverse Spatially Offset Raman Spectroscopy (iSORS)

Inverse Spatially Offset Raman Spectroscopy (iSORS) is a variation of the SORS technique, developed to enable deeper and more sensitive non-invasive probing of turbid, layered media such as biological tissues[19]. While conventional SORS collects Raman signals from spatially offset positions relative to a central laser excitation spot, iSORS adopts a reverse geometry: Raman photons are collected from a central point while the sample is illuminated by a ring-shaped laser beam. This configuration minimises spectral distortions inherent to multiple collection offsets and improves the signal-to-noise ratio by concentrating detection in a single channel.

The ring illumination in iSORS can be generated using an axicon lens, which transforms a collimated laser beam into an annular profile. The spatial offset, defined as the illumination ring radius, can be tuned by adjusting the distance between the axicon and the sample. This tunable geometry allows flexible control over the sampling depth and enables high-power laser delivery while maintaining low power density, an important consideration for in vivo applications where illumination intensity is strictly limited.

4.2.5 Dual Wavelength Raman Spectroscopy

Dual wavelength Raman spectroscopy combines the strengths of the fingerprint and high wavenumber regions by using two excitation wavelengths within a single system[154]. This approach enables simultaneous or sequential acquisition of comprehensive biochemical information from tissue samples, enhancing the diagnostic potential of Raman spectroscopy in biomedical applications.

Traditional single excitation Raman systems often face limitations in simultaneously accessing both regions due to detector sensitivity and optical configuration. In contrast, a dual excitation setup using two near-infrared laser sources, overcome these constraints. Both excitation wavelengths can be integrated into a single laser module and delivered through a fibre optic probe, enabling rapid switching between fingerprint and high wavenumber acquisition without the need for realignment or manual optical adjustment. This configuration maps the relevant Raman shifts for each excitation wavelength onto the most sensitive detection range of a silicon CCD, ensuring high spectral quality across the full biochemical range.

4.3 Diffuse Optics and Pulse Oximeter

When light enters biological tissue, it interacts with the medium through several mechanisms, including absorption, scattering, and fluorescence. These interactions determine how light propagates within the tissue and how much of it is eventually detected at the surface. In highly scattering media such as skin, muscle, or brain tissue, the majority of photons undergo multiple scattering events before either being absorbed or escaping the tissue. Understanding these fundamental light–tissue interactions is essential for interpreting optical signals and forms the basis of diffuse optics.

4.3.1 Scattering

Scattering occurs when photons interact with microscopic variations in the refractive index within biological tissue, such as cell membranes, organelles, or collagen fibres, leading to changes in photon direction. Unlike absorption, which results in energy loss, scattering redistributes photons spatially and strongly influences how light propagates through tissue.

Two primary types of scattering are relevant in biological media: Rayleigh scattering and Mie scattering. Rayleigh scattering occurs when the scattering particles are much smaller than the wavelength of light and its intensity scales with the inverse fourth power of wavelength ($\propto \lambda^{-4}$), making it more pronounced at shorter wavelengths. Mie scattering, in contrast, is caused by particles that are comparable in size to the wavelength, such as cellular structures and organelles, and shows a weaker dependence on wavelength[155].

Biological tissues exhibit anisotropic scattering, meaning that photons are more likely to scatter in the forward direction than backward or laterally. This directional preference is characterised by the anisotropy factor, g, defined as the mean cosine of the scattering angle:

$$g = \langle \cos\theta \rangle \tag{4.15}$$

where θ is the scattering angle. In most tissues, g typically ranges from 0.8 to 0.95, indicating strong forward scattering.

To account for anisotropic behaviour, the reduced scattering coefficient, μ_s', is defined as:

$$\mu_s' = \mu_s(1 - g) \tag{4.16}$$

where μ_s is the scattering coefficient [cm^{-1}], representing the probability of scattering per unit pathlength. The reduced scattering coefficient, μ_s', reflects the effective rate at which photon direction becomes randomised due to multiple scattering events.

In the NIR window (650–950 nm), scattering dominates over absorption ($\mu_s \gg \mu_a$), causing photons to follow highly tortuous paths. The actual distance travelled by photons is therefore much greater than the source–detector separation. This behaviour forms the basis for applying diffusion theory to model photon transport in tissue, as described in the later subsection.

4.3.2 Absorption

Absorption refers to the process by which the energy of incident photons is transferred to tissue chromophores, resulting in attenuation of the light signal. In the visible and near-infrared (NIR) region, the dominant absorbers in biological tissue include oxyhaemoglobin (HbO_2), deoxyhaemoglobin (Hb), water, melanin, and lipids. Each chromophore has a characteristic absorption spectrum, and their concentrations influence the spectral dependence of tissue absorption. The absorption coefficient, μ_a [cm^{-1}], quantifies the probability of photon absorption per unit pathlength.

In diffuse optical measurements, changes in absorption are often used to estimate physiological parameters such as blood oxygen saturation, haemoglobin concentration, and tissue hydration. For instance, pulse oximeters utilise the differential absorption of HbO_2 and Hb at specific wavelengths to estimate arterial oxygen saturation non-invasively.

The relationship between light attenuation, chromophore concentration, and pathlength is described by the Beer–Lambert law in exponential form[156]:

$$I(\lambda) = I_0(\lambda)\, e^{-\varepsilon(\lambda)\, c\, l} \tag{4.17}$$

where $I_0(\lambda)$ and $I(\lambda)$ are the incident and transmitted light intensities, respectively, $\varepsilon(\lambda)$ is the molar extinction coefficient [$\mathrm{cm}^{-1}\cdot(\mathrm{mol/L})^{-1}$], c is the chromophore concentration [mol/L], and l is the optical pathlength through the sample [cm].

In biological tissues, where scattering dominates and the path of light is no longer straight, the Beer–Lambert law is extended to the modified Beer–Lambert law, which accounts for scattering-related pathlength enhancement[157]:

$$I(\lambda) = I_0(\lambda)\, e^{-\mu_a(\lambda)\cdot L(\lambda)\cdot DPF(\lambda)} \tag{4.18}$$

where $I(\lambda)$ is the detected intensity, $\mu_a(\lambda)$ is the absorption coefficient, $L(\lambda)$ is the source–detector separation, and $DPF(\lambda)$ is the differential pathlength factor, which corrects for the increased effective pathlength due to scattering. The modified Beer–Lambert law is commonly applied in functional near-infrared spectroscopy (fNIRS) and pulse oximetry to quantify relative changes in chromophore concentrations in vivo.

4.3.3 Diffusion Theory

In highly scattering media such as biological tissue, the propagation of photons becomes randomised due to frequent scattering events. When scattering significantly outweighs absorption ($\mu_s' \gg \mu_a$), light transport can be effectively described by the diffusion approximation to the radiative transport equation (RTE). This approximation treats photon fluence as a diffusive process and provides the theoretical foundation for many diffuse optical techniques.

The time-dependent diffusion equation for photon fluence rate in a homogeneous, isotropic medium is expressed as[158]:

$$\frac{1}{c}\frac{\partial \Phi(\mathbf{r},t)}{\partial t} = \nabla\cdot[D\nabla\Phi(\mathbf{r},t)] - \mu_a\Phi(\mathbf{r},t) + S(\mathbf{r},t) \tag{4.19}$$

where $\Phi(\mathbf{r},t)$ is the photon fluence rate [$\mathrm{W\cdot cm}^{-2}$] at position $\mathbf{r}$ and time t, c is the speed of light in the medium, D is the diffusion coefficient given by $D = 1/[3(\mu_a + \mu_s')]$, μ_a is the absorption coefficient [cm^{-1}], μ_s' is the reduced scattering coefficient [cm^{-1}], and $S(\mathbf{r},t)$ is the light source term [$\mathrm{W\cdot cm}^{-3}$].

This equation is particularly relevant in time-resolved spectroscopy, where the temporal spread of photons is measured to retrieve tissue optical properties with high sensitivity and spatial resolution.

For continuous-wave (CW) or steady-state conditions, where the illumination is constant over time, the time derivative term becomes zero. The diffusion equation then simplifies to[147]:

$$\nabla^2\Phi(\mathbf{r}) - \frac{\mu_a}{D}\Phi(\mathbf{r}) = -\frac{S(\mathbf{r})}{D} \tag{4.20}$$

This steady-state equation describes how photon fluence distributes spatially within tissue under constant illumination. The solution depends on the source configuration, boundary conditions, and the geometry of the medium.

Diffusion theory is fundamental to the modelling and analysis of many diffuse optical imaging and spectroscopy methods, including fNIRS, diffuse optical tomography (DOT), and spatially resolved spectroscopy. These techniques rely on the assumption of multiple scattering and use solutions of the diffusion equation to interpret measured light attenuation and recover the optical properties of tissue.

4.3.4 Pulse Oximetry

Pulse oximetry is a widely used non-invasive method for estimating arterial oxygen saturation (SpO_2), providing insight into respiratory function by analysing changes in light absorption in pulsatile blood. The technique is based on photoplethysmography (PPG), which detects the periodic modulation of transmitted or reflected light caused by cardiac-induced changes in arterial blood volume.

The principle of pulse oximetry relies on the different optical absorption spectra of oxygenated haemoglobin (HbO_2) and deoxygenated haemoglobin (Hb) in the red and NIR wavelength regions. Typically, red light at approximately 660 nm and infrared light at around 940 nm are used. At 660 nm, Hb absorbs more strongly, whereas at 940 nm, HbO_2 is the dominant absorber. The absorption spectra of HbO_2 and Hb are shown in Figure 4.4. A photodetector measures the light intensity after it has passed through or reflected from tissue, commonly a fingertip or earlobe.

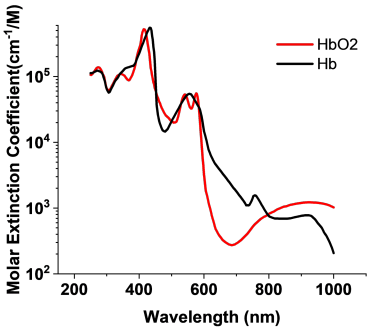

Figure 4.4: Absorption spectra of the oxygenated and deoxygenated haemoglobin molecules.

The measured PPG signal consists of a pulsatile component (AC), attributed to arterial blood volume changes during the cardiac cycle, and a non-pulsatile component (DC), due to absorption by static tissues and venous blood. An example of measured PPG signal is shown in Figure 4.5. The ratio of the normalised pulsatile signals at the two wavelengths is defined as[159]:

$$R = \frac{(AC/DC)_{\text{red}}}{(AC/DC)_{\text{infrared}}} \tag{4.21}$$

This ratio R is empirically correlated to arterial oxygen saturation (SpO_2) using a calibration function derived from measurements in healthy volunteers, where R is recorded simultaneously with in vitro SaO_2 using co-oximetry. A general form of this calibration is given by[160]:

$$SpO_2 = f(R) = \frac{k_1 - k_2 R}{k_3 - k_4 R} \tag{4.22}$$

where k_i are constants specific to the sensor and device.

Pulse oximeter is a crucial tool for detecting oxygen saturation and is widely used in clinical settings due to its simplicity, portability, and real-time monitoring capability.

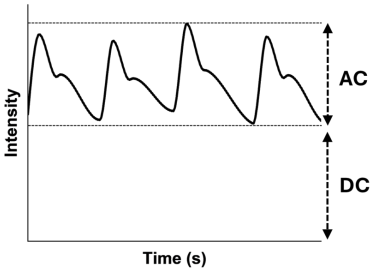

Figure 4.5: Schematic diagram of light absorbance by a pulse oximeter.

4.4 Monte Carlo Simulation

Monte Carlo (MC) simulation is a probabilistic computational method that utilises random sampling to model complex physical systems. The technique traces its origins to the mid-20th century, when it was developed during the Manhattan Project by scientists including Stanislaw Ulam and John von Neumann. The method was named after the Monte Carlo Casino in Monaco, reflecting its reliance on randomness and statistical sampling[161].

Monte Carlo simulation models light transport through a statistical approach by simulating the propagation of a large number of photon packets, each undergoing scattering and absorption events governed by probabilistic rules. These rules are derived from the macroscopic optical properties of the tissue, including the absorption coefficient μ_a, scattering coefficient μ_s, anisotropy factor g, and refractive index n.

Each photon packet is launched into a defined geometry, typically a multilayered tissue slab, with an initial weight of unity. As it travels through the medium, the photon undergoes a series of interactions. At each step, its path length is sampled from an exponential distribution:

$$s = -\frac{\ln(\xi)}{\mu_t} \tag{4.23}$$

where ξ is a uniformly distributed random number between 0 and 1, and $\mu_t = \mu_a + \mu_s$ is the total interaction coefficient.

Upon reaching an interaction site, a fraction of the photon's weight is absorbed and recorded in the associated voxel. The remaining weight is updated, and the direction of the photon is altered based on a scattering phase function, most commonly the Henyey–Greenstein function:

$$P(\cos\theta) = \frac{1 - g^2}{2(1 + g^2 - 2g\cos\theta)^{3/2}} \tag{4.24}$$

where θ is the scattering angle. The azimuthal scattering angle ϕ is uniformly sampled between 0 and 2π. The photon's directional cosines are updated accordingly in a local spherical coordinate system aligned with its previous direction.

When a photon reaches the boundary between two layers or the outer interface with ambient media, Fresnel equations are applied to determine the probabilities of reflection and transmission, depending on the refractive index mismatch and angle of incidence. If transmitted, the photon continues in the adjacent layer with updated direction; if reflected, the direction is modified accordingly.

Several computational implementations have been developed to efficiently simulate photon transport in biological tissues. Two widely used tools are Monte Carlo Modelling of Light transport in Multi-Layered tissues (MCML), a classic and highly customisable CPU-based code, and Monte Carlo eXtreme (MCX), a GPU-accelerated platform capable of performing fast, three-dimensional simulations in highly complex tissue geometries[162, 163].

In this thesis, the MCX platform was applied to model light propagation in iSORS. By modelling photon transport in layered tissue geometries, MCX enabled the estimation of Raman signal contributions from subsurface regions at varying source–detector separations. This approach was used to determine the optimal spatial offset that maximises signal recovery from the target layer, supporting the experimental design and interpretation of iSORS measurements.

The biophotonics modalities described in this chapter establish the detection principles used throughout this thesis. Building on this foundation, the next chapter focuses on the design and implementation of a Köhler integrator–based top-hat illumination system optimised for UCNP imaging. This approach enables uniform and efficient excitation, improving both image quality and quantitative performance in microscopic imaging.

Chapter 5

Köhler integrator for wide field imaging

Uniform and controlled illumination is fundamental to the performance and reliability of optical imaging systems, particularly in microscopy and quantitative imaging applications. The Köhler integrator is an optical beam homogeniser that uses two microlens arrays and a condenser lens to produce uniform, spatially averaged illumination at the sample plane, independent of the source's spatial structure. This chapter presents the theoretical foundation, optical design, and application of the Köhler integrator for quantitative imaging of Human Epidermal Growth Factor Receptor 2 (HER2) using UCNPs. The experimental validation of this approach, along with its application to breast cancer biomarker quantification, has been reported in our published work Paper **I**.

5.1 Theoretical Background

The Köhler integrator is an optical beam homogenisation system that provides spatially uniform and angularly controlled illumination at the sample plane. It originates from the Köhler illumination principle, which was initially developed to enhance illumination uniformity in brightfield microscopy. The Köhler integrator has been adapted to achieve flat-top beam profiles, reduce speckle artefacts, and ensure consistent excitation across the field of view.

The Köhler integrator consists of two microlens arrays (MLAs), LA1 and LA2, and a condenser lens. The schematic layout of the Köhler integrator is shown in Figure 2.3. The first microlens array (LA1) splits the incident beam into multiple beamlets, each representing a sub-aperture of the incoming wavefront. These beamlets are then re-imaged by the second microlens array (LA2). The condenser lens collects and overlaps the images of these beamlets in the object plane, producing a spatially uniform intensity distribution.

The diameter of the flat-top illumination D_{FT} at the object plane depends on the geometrical configuration of the Köhler integrator. Specifically, it is influenced by the pitch of the microlens arrays p_{LA}, the focal lengths of the condenser lens f_{FL}, and the focal length of two microlens arrays f_{LA1} and f_{LA2}, as well as the axial separation a_{12} between LA_1 and LA_2. The general expression for the flat-top size is given by:

$$D_{\mathrm{FT}} = p_{\mathrm{LA}} \cdot \frac{f_{\mathrm{FL}}\left(f_{\mathrm{LA1}} + f_{\mathrm{LA2}} - a_{12}\right)}{f_{\mathrm{LA1}} \cdot f_{\mathrm{LA2}}} \tag{5.1}$$

To satisfy the imaging condition of the Köhler integrator, the spacing between the microlens arrays is typically set such that $a_{12} = f_{\mathrm{LA2}}$. Under this condition, Equation 5.1 simplifies to:

$$D_{\mathrm{FT}} = p_{\mathrm{LA}} \cdot \frac{f_{\mathrm{FL}}}{f_{\mathrm{LA2}}} \tag{5.2}$$

5.2 Experimental Setup Design

A custom widefield microscope was developed to provide spatially uniform excitation for quantitative HER2 imaging using UCNPs. The illumination system uses a Köhler integrator to produce a homogenised top-hat beam, critical for minimising variability in illumination across the field of view. A schematic of the optical setup is shown in Figure 5.1.

A laser diode (DST11-T193-H2O, Ostech) emitting at 976 nm was first collimated using an achromatic doublet lens, L1 (AC254-050-B-ML, Thorlabs), and directed into a Köhler integrator. The integrator consisted of two identical MLAs (10×10 mm, 500 µm pitch, 1.2° divergence, Edmund Optics), each with a focal length of 13.8 mm. The MLAs were separated by a distance equal to their focal length to satisfy the imaging condition for effective beam homogenisation.

Assuming the homogenised beam was directly focused by a 20× microscope objective (CFI60 TU Plan Epi ELWD, Nikon) with a focal length of 10 mm, the resulting spot size at the sample plane would be:

$$D_{\mathrm{FT}} = \frac{f_{\mathrm{FL}}}{f_{\mathrm{LA}}} \cdot p_{\mathrm{LA}} = \frac{10\,\mathrm{mm}}{13.8\,\mathrm{mm}} \cdot 0.5\,\mathrm{mm} = 0.362\,\mathrm{mm} \tag{5.3}$$

The scientific CMOS camera used in the imaging system had a resolution of 2048×2048 pixels and a pixel size of 6.5 µm. With a 20× objective, the effective field of view at the sample plane was:

$$\mathrm{FOV}_{\mathrm{sample}} = \frac{2048 \times 6.5\,\mu\mathrm{m}}{20} = 665.6\,\mu\mathrm{m} = 0.6656\,\mathrm{mm} \tag{5.4}$$

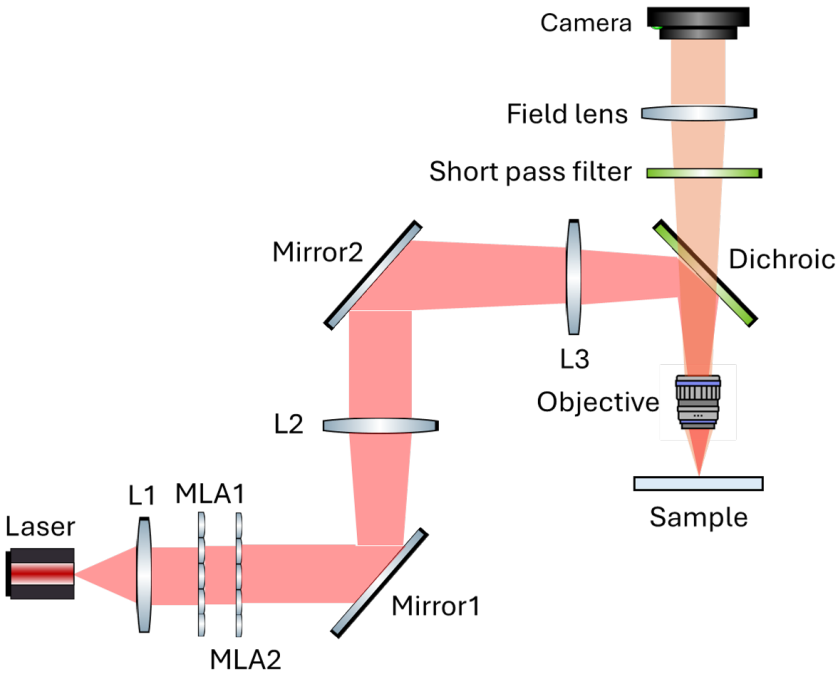

Figure 5.1: Schematic layout of the illumination system for the microscope.

To match the illumination spot with the camera's field of view, a telescope system was introduced after the Köhler integrator. This was achieved by incorporating lenses L2 (LA1484-B-ML, Thorlabs) and L3 (LA1433-B-ML, Thorlabs), arranged to provide a magnification factor of 2×. This adjustment ensured that the homogenised beam appropriately filled the sample area imaged by the camera while maintaining sufficient irradiance for quantitative UCNP imaging.

To support the optical design and validate the performance of the Köhler integrator-based illumination system, ray-tracing simulations were conducted using Zemax OpticStudio in non-sequential mode. This approach was chosen because of the need to model beam propagation through multiple discrete optical surfaces, including MLAs and their associated ray splitting and overlapping behaviour. The full optical path, from the laser source through the MLAs and condenser optics to the sample plane, was modelled to evaluate key parameters such as beam homogenisation, spot size, and intensity distribution. Irradiance maps were generated at the sample plane to evaluate uniformity and quantify flat-top performance. The Zemax simulations also provided tolerance insights related to microlens alignment, array pitch variation, and spacing errors. These results were used to guide the physical alignment procedure and helped to ensure that the experimental setup closely followed the designed optical behaviour. The irradiance map is shown in Figure 5.2.

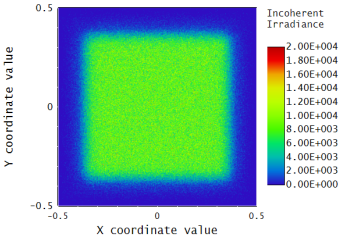

Figure 5.2: Irradiance map of the Zemax simulation

5.3 Sample Preparation and UCNP Labelling Protocol

Formalin fixed paraffin embedded (FFPE) breast cancer tissue samples were sectioned into 4 µm thin slices using a microtome (Microm HM-360, Marshall Scientific, USA) and mounted onto SuperFrost™ Plus microscope slides (HistoLab, Sweden). Dewaxing was performed by immersing the sections twice for 5 min in xylene, followed by a graded rehydration series consisting of two immersions of 5 min in absolute ethanol, then 5 min each in 96% ethanol, 70% ethanol, and distilled water. Heat induced antigen retrieval (HIER) was subsequently performed to unmask the HER2 epitopes. Slides were transferred into a container with antigen retrieval buffer (250 mL, EnVision FLEX high pH, Agilent, USA) preheated to 95 °C in a water bath and incubated for 20 min at 95 °C. The container was then removed from the water bath and allowed to cool for 20 min at room temperature.

All subsequent steps were conducted at room temperature. Depending on the size of the tissue section, 150 to 350 µL of reagent was applied to ensure complete coverage of each sample. Slides were transferred into Tris buffered saline containing 1 mM sodium fluoride (TBSF). Sections intended for counterstaining with hematoxylin were immersed in Mayer's Hematoxylin for 3 min followed by washing in TBSF for 2×1 min. Sections intended for labelling with antibody horseradish peroxidase (HRP) conjugates were quenched with 0.3% H_2O_2 in TBSF for 10 min followed by a washing step in TBSF. All sections were then encircled with a liquid blocker (ImmEdge Pen, Vector Laboratories, USA) and transferred to a Coplin jar containing TBSF. A blocking buffer was applied to each section and incubated for 45 min, followed by washing in TBSF for 1 min.

For UCNP labelling, endogenous biotin was first blocked using a ready-to-use streptavidin solution (20 min, SP-2002, Vector Laboratories) followed by a biotin solution (20 min, SP-2002, Vector Laboratories), with a wash of twice for 1 min in TBSF after each blocking step. Non-specific binding sites were then blocked using TBSF containing 10% SuperBlock (37535, ThermoFisher Scientific), followed by the same wash-

ing procedure. The primary anti-HER2 antibody (A0485, Agilent) was diluted to 1 µg/mL in dilution buffer (TBSF supplemented with 0.05% Tween20 and 10% SuperBlock), applied to the sections, and incubated for 60 min. Negative controls were incubated with dilution buffer without the primary antibody to assess non-specific background. Following a further wash of twice for 1 min in TBSF, a biotinylated anti-rabbit secondary antibody (711-005-152, Jackson Immunoresearch, USA) was applied at a concentration of 2 µg/mL in dilution buffer and incubated for 60 min. After washing twice for 1 min in TBSF, a UCNP streptavidin conjugate (SCIZYS reagent, Lumito, Sweden) was applied in dilution buffer and incubated for 45 min. This conjugate binds selectively to the biotinylated secondary antibody, forming a sandwich structure that localises the UCNPs to HER2 expressing membrane regions. Three final washes of 1 min each in TBSF were performed to remove unbound UCNPs, after which sections were mounted using an aqueous mounting medium (Fluoroshield™, Sigma Aldrich). Sections counterstained with DAPI were instead mounted with a DAPI containing mounting medium (ab104139, Abcam, UK).

For comparison with the conventional chromogenic method, parallel sections were labelled using the HRP/DAB protocol. After primary antibody incubation, slides were incubated with a ready-to-use anti-rabbit secondary antibody HRP conjugate (ImmPress® HRP Goat Anti-Rabbit IgG Polymer Detection Kit Peroxidase, Vector Laboratories) for 45 min and washed three times for 1 min with TBSF. The DAB substrate was prepared by adding one droplet of DAB substrate per millilitre of substrate buffer (EnVision Flex Mini Kit, High pH, Agilent). Slides were incubated with this substrate for 10 min, washed three times for 1 min with TBSF, and dehydrated through a graded ethanol series of three immersions for 1 min each in 70%, 96%, and absolute ethanol, followed by 5 min in xylene, before being mounted using Pertex as a mounting medium. The signal to background ratio for DAB was calculated as the ratio of the average intensity in an unlabelled background region to the average intensity in a DAB labelled region of a HER2 3+ breast cancer section, with the signal averaged across RGB channels, yielding a signal to background ratio of 1.6.

5.4 Application for UCNP Imaging

Using the sample preparation and labelling workflow described above, the Köhler integrator based microscope system was applied to widefield UCNP imaging for semi quantitative HER2 assessment in breast cancer tissues. The system provided spatially uniform excitation and high contrast imaging, facilitating accurate visualisation of UCNP-labelled HER2 in both control pellet arrays (CPAs) and tissue sections. A Fourier transform-based image processing algorithm was developed to analyse the spatial distribution and completeness of membrane-localised HER2 expression, enabling semi-quantitative assessment across four HER2 levels (0, 1+, 2+, 3+). The high signal-to-background ratio achieved with UCNPs, compared to conventional DAB (3,3′-Diaminobenzidine) staining, demonstrated the potential of this method for digital pathology. The detailed methodology and results of HER2 quantification are presented in Paper **I**.

This chapter introduces the uniform illumination through the Köhler integrator system, which is beneficial for quantitative imaging of UCNPs. In contrast, structured illumination techniques can retrieve subsurface information that uniform illumination cannot access. Therefore, the next chapter presents a ring-shaped structured illumination geometry

designed for iSORS, enabling selective probing of bone beneath overlying tissues with improved sensitivity.

Chapter 6

Ring illumination for dual wavelength inverse spatially offset Raman spectroscopy

In vivo bone characterisation using Raman spectroscopy presents significant challenges due to the complex tissue layers overlying the bone. Inverse spatially offset Raman spectroscopy (iSORS) has emerged as a powerful approach to selectively enhance signals from subsurface structures by collecting Raman photons from the central region while illuminating the surrounding area. To provide comprehensive biochemical information of bone, a dual-wavelength configuration using 730 and 830 nm excitations is applied to access both finger print and high wavenumber spectral regions. This chapter presents the theoretical basis of ring illumination through axicon lenses and its implementation for iSORS to enable label-free, non-invasive biochemical assessment of bone. The concepts and methods described here provide the foundation for Paper **III**, where ring-illumination iSORS was experimentally realised and applied for in vivo bone characterisation.

6.1 Theoretical Background of Axicon Lens and Ring Illumination

An axicon is a conical optical element that transforms a collimated beam into a focal line or a ring-shaped intensity distribution around the optical axis. The schematic layout is shown in Figure 6.1. When a collimated Gaussian beam enters the axicon, each annular segment of the beam is refracted by a fixed angle determined by the axicon's apex angle and the refractive index of the material. The result is the formation of a Bessel-like beam in the near field and a ring-shaped intensity distribution in the far field. In the near field, the beam consists of a central bright core surrounded by concentric rings and remains nearly non-diffracting over a defined distance, known as the depth of focus (DOF). The DOF is given by:

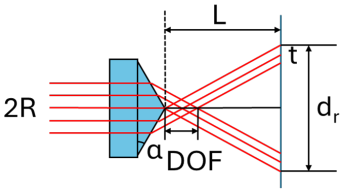

Figure 6.1: Schematic layout of an axicon

$$\mathrm{DOF} = \frac{R\sqrt{1-n^2\sin^2\alpha}}{\sin\alpha\cos\alpha\left(n\cos\alpha-\sqrt{1-n^2\sin^2\alpha}\right)} \approx \frac{R}{(n-1)\alpha} \tag{6.1}$$

where R is the input beam radius, n is the refractive index of the axicon material, and α is the base angle of the axicon.

Beyond the Bessel beam region, the light propagates into a ring-shaped distribution, the ring thickness remains approximately constant

and is equal to the radius of the incident beam:

$$t = \frac{R\sqrt{1 - n^2 \sin^2 \alpha}}{\cos \alpha \left(n \sin^2 \alpha + \cos \alpha \sqrt{1 - n^2 \sin^2 \alpha} \right)} \approx R \tag{6.2}$$

where t is the thickness of the ring. The diameter can be calculated as:

$$d_r = 2L \left[\frac{\sin \alpha \left(n \cos \alpha - \sqrt{1 - n^2 \sin^2 \alpha} \right)}{n \sin^2 \alpha + \cos \alpha \sqrt{1 - n^2 \sin^2 \alpha}} \right] \approx 2L \tan \left[(n - 1)\alpha \right] \tag{6.3}$$

where d_r is the diameter of the ring formed at a propagation distance L from the axicon.

6.2 Experimental Setup for iSORS system

Figure 6.2(a) illustrates the schematic of the DWiSORS system. A dual-wavelength laser diode (model #0811A100-B Fat Boy, Innovative Photonics Solutions) provides excitation wavelengths of 730 nm and 830 nm. The output from the laser is fibre-coupled (M43L02, Thorlabs) and collimated using a fibre collimator C1 (CFC-2X-A, Thorlabs). The collimated beam passes through a pair of achromatic doublets, L1 (AC254-030-A, Thorlabs) and L2 (AC254-040-B-ML, Thorlabs), to focus the beam on the sample plane.

Ring illumination is generated using an axicon lens (AX1220-B, Thorlabs). The ring diameter on the sample plane can be tuned by adjusting the axial position of the axicon. A short-pass filter (SP, FF01-842/SP-25, Semrock) removes any longer wavelength background from the excitation source. The cleaned excitation beam is reflected by a dichroic mirror (DM, DI02-R830-25X36, Semrock) and projected onto the sample to form a ring pattern, as shown in the inset photograph of Figure 6.2(a).

The Raman signal backscattered from the centre of the ring is collected in an inverse-SORS configuration using a lens L3 (AC254-100-AB-ML, Thorlabs) and filtered through a long-pass filter (LP, BLP01-830R-25, Semrock, USA) to block residual Rayleigh scattered light. The filtered signal is coupled into a custom fibre bundle (BFL200LS02, Thorlabs) by a fibre coupler C3 (F810SMA-780, Thorlabs). The fibre bundle transforms the circular collection area into a linear array suitable for the spectrometer slit.

The signal is analysed by a spectrometer (Acton LS785, f/2, Teledyne Princeton Instruments), equipped with a fixed grating and a deep-depletion CCD camera (Blaze: 400HR, Teledyne Princeton Instruments)[164]. The detection range of 858–1015 nm allows simultaneous coverage of both the fingerprint and high-wavenumber Raman regions. As shown in Figure 6.2(b), this range corresponds to 393–2195 cm^{-1} for 830 nm excitation and 2043–3846 cm^{-1} for 730 nm excitation. The detection configuration enables effective mapping of the spectral content from both excitation wavelengths within the same acquisition window.

6.3 Application for in vivo Bone Characterisation

The DWiSORS system was applied to assess its capability for non-invasive in vivo bone characterisation. A metric, named enhancement to noise ratio (ENR), was introduced to determine the optimal offset for the SORS configuration. Measurements on tissue and bone mimicking phantoms, together with Monte Carlo simulation, were conducted to validate the proposed metric. The identified optimal offset was then

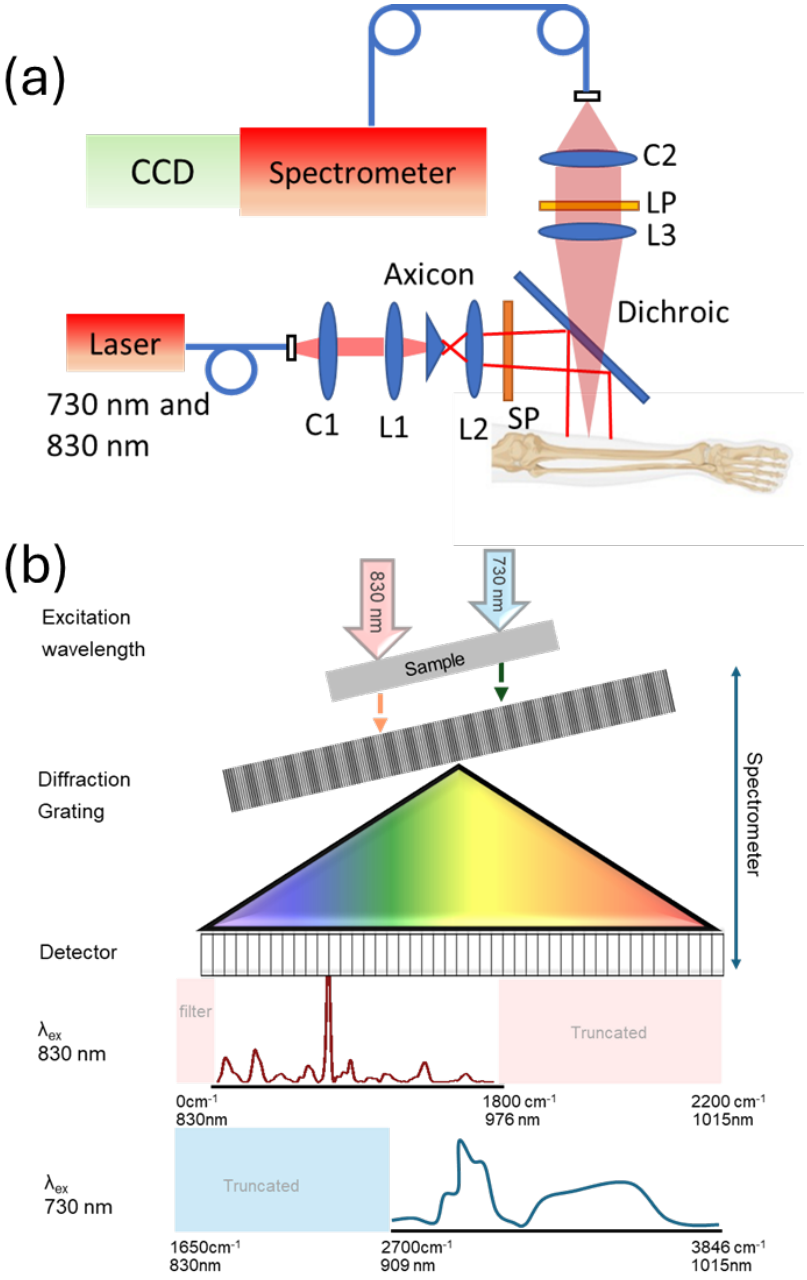

Figure 6.2: (a) Schematic layout of the Raman system. (C: collimator, L: lens, SP: short pass filter, LP: long pass filter) (b) Wavelength-dependent mapping of fingerprint and high-wavenumber Raman regions on the detector for 730 nm and 830 nm excitations.

applied to in vivo measurements on healthy volunteers to assess the system's performance under realistic physiological conditions. The results are described in Paper **III**.

Having introduced all the modalities and the associated beam shaping applications, the next chapter presents the design of a light-guided dynamic phantom system for characterisation and validation. This platform provides a controlled, reproducible environment for assessing the performance of the developed systems and ensuring their reliability in practical applications.

Chapter 7

A light-guide based dynamic phantom for system validation

Phantoms are artificial models that replicate the optical and physical properties of biological tissues, providing a controlled and repeatable environment for the development, testing, and calibration of biophotonics systems. As the precision of optical sensing increasingly relies on engineered illumination and dynamic signal interpretation, the need for realistic and responsive validation tools has become more apparent. While conventional static phantoms are useful for structural assessment, they are inherently limited in their ability to reproduce physiological dynamics such as pulsatile blood flow or fluctuations in oxygen saturation. To address this limitation, this chapter introduces a light-guided dynamic phantom capable of replicating time-varying optical signals, offering a more realistic and standardised platform for the evaluation of advanced optical detection systems. The design and characterisation of this system have been reported in our publication Paper **II**.

7.1 Introduction on Optical Phantom

Biophotonics phantoms are artificial structures designed to simulate the optical properties of biological media[165]. They are essential tools in biomedical optics, enabling researchers to study light-tissue interactions in a safe, controllable, and repeatable environment. By replicating parameters such as absorption, scattering, and fluorescence, phantoms allow the simulation of light distribution with geometries of biological tissue and provide a standard reference for validating and characterising the performance of optical devices. They are widely used for system calibration, optimisation, and quality control, offering a reliable approach to benchmark instrumentation without relying on biological samples[166–169].

Conventional optical phantoms are typically static, which means they are designed to represent tissue properties that do not change over time. These static models are well suited for characterising spatial resolution, optical penetration depth, signal-to-noise ratio, and other steady-state performance metrics of optical systems. However, many biomedical optics applications involve time-varying physiological signals. Haemoglobin concentration is a critical physiological parameter, reflecting the oxygen-carrying capacity of blood. Monitoring haemoglobin levels provides valuable clinical insights for disease diagnosis, preoperative and postoperative care, treatment evaluation, and even athletic performance assessment[170–175]. With the emergence of portable and wearable health monitoring systems, there is an increasing demand for optical

standards that can dynamically simulate changes in haemoglobin oxygen saturation during physiological processes such as breathing and heartbeat cycles.

Various liquid phantoms have been developed using materials such as whole blood or extracted erythrocytes to replicate changes in oxygen saturation. However, the use of blood components raises ethical and safety concerns, while also reducing the stability and shelf life of the phantoms. To ensure appropriate measurement conditions, both temperature and pH must be continuously monitored throughout the experimental process. The incorporation of temperature and pH sensors, along with peristaltic pumps and membrane oxygenators, significantly increases the cost and complexity of the setup. Oxygen saturation levels in liquid phantoms are typically modulated by introducing oxygenating compounds such as oxygen, and deoxygenating compounds such as yeast, nitrogen bubbling, or enzymatic mixtures comprising D-glucose, glucose oxidase, and catalase. Blood circulation within the phantom is maintained using a peristaltic pump, while a membrane oxygenator is used to regulate oxygenation levels. However, these methods are time-consuming: yeast requires approximately 20 to 30 minutes to gradually reduce oxygen saturation[176], and nitrogen bubbling takes around 30 minutes to achieve effective deoxygenation[177]. Such delays significantly limit the feasibility of real-time control in dynamic phantom applications.

To overcome these challenges associated with liquid phantoms, solid dynamic phantoms have been developed to offer more stable, controllable, and reproducible alternatives for simulating dynamic optical responses. *Koh et al.*[178] introduced a dynamic phantom design in which a modified liquid crystal display (LCD) is embedded between two solid epoxy resin layers that mimic the absorption and scattering properties of biological tissue. The LCD enables spatially and temporally modulations that simulate haemodynamic responses. This design supports flexible control over attenuation patterns, making it suitable for evaluating system resolution, dynamic range, and sensitivity to different activation region sizes and shapes. *Funane et al.*[179] developed a two-layer solid dynamic phantom with independently driven absorbers mounted on motorised linear stages. These absorbers are embedded within a polyoxymethylene matrix and are positioned at depths corresponding to superficial and deep tissues. The movement of each absorber modulates the optical path length and, consequently, the effective absorption at specific depths. *Hebden et al.*[180] introduced an electrically-activated solid dynamic phantom based on thermochromic dye embedded in a resin matrix. This design enables reversible, localised changes in optical absorption by heating regions containing thermochromic pigment using internal resistive elements. The pigment transitions from black to white around an activation temperature of 47 °C, mimicking variations in absorption. However, the performance of the LCD-based phantom is influenced by the angular dependence of the LCD's optical attenuation, which is further affected by the scattering properties of the top phantom layer. The phantom with moving stages creates only macroscopic absorption changes and cannot replicate microvascular complexity. The mechanical system also limits speed and spatial fidelity, and its layered geometry does not fully reflect the heterogeneity of in vivo tissue structures. For the thermochromic dynamic phantom, each activation cycle requires approximately 70 seconds to transition from room temperature, which is too slow for rapid modulation. In addition, the smallest allowable spacing between neighbouring targets is 11.2 mm to prevent thermal crosstalk, which limits the spatial resolution.

In this chapter, we introduce a novel light-guided solid dynamic phantom that overcomes these limitations by decoupling the LCD from the scattering layer using a polymer optical fibre light guide. This configura-

tion avoids angular dependence, enables fine spatial control, and allows rapid modulation of absorption properties. The phantom can generate realistic biological signals such as photoplethysmography (PPG) waveforms at multiple wavelengths (455, 530, 660, and 940 nm), including different heart rates and oxygen saturation levels, offering a solid platform for standardising and validating biomedical optical devices such as pulse oximeters, imaging systems, and spectroscopy platforms.

7.2 Design of the Light-guided Dynamic Phantom

A dynamic phantom system was developed to modulate light transmission through a static, tissue-mimicking silicone layer. The photo and the optical design are shown in Figure 7.1. Light transmitted through the static silicone phantom was collected using a 4 cm long, 3 mm diameter polymer optical fibre (OMPF3000, The Optoelectronic Manufacturing Corporation Ltd.). This light was subsequently collimated using a condenser lens (ACL2520U, Thorlabs), creating a parallel beam profile to remove the angular dependence of the downstream modulation element. The collimated beam was modulated by an LCD (FOS-NIR (1100), LC-Tec Displays AB), which was electronically driven by a National Instruments data acquisition device (USB-6212, National Instruments). The modulated light was then reflected back through the phantom using a silver mirror (PF10-03-P01, Thorlabs), enabling dynamic control of light patterns incident on the tissue-mimicking layer.

The static superficial layer was a silicone-based tissue phantom fabricated in a round shape with a 9 cm diameter and a thickness of 0.5 mm. The phantom composition followed the protocol described in Ref. [169], consisting of SiliGlass (MB Fibreglass) as the bulk matrix, polycraft black silicone pigment (MB Fibreglass) as the absorber, and silica microspheres (440345, Sigma-Aldrich) as the scattering agent. Optical characterisation was performed using a time-domain diffuse optical spectrometer, targeting an absorption coefficient (μ_a) of 0.1 cm^{-1} and a reduced scattering coefficient (μ_s') of 10 cm^{-1}.

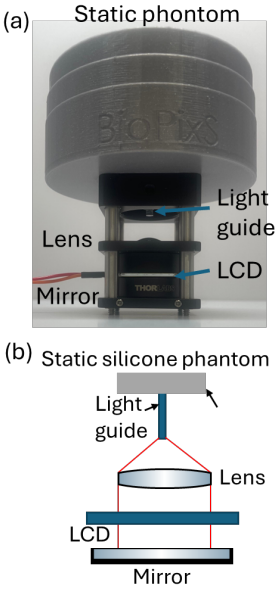

Figure 7.1: (a) Photo of the dynamic phantom. (b) Scheme of the dynamic phantom.

7.3 Dynamic Phantom Characterisation Using Camera

To characterise and validate the dynamic phantom, two separate validation systems were developed. The first system used a camera for detection and demonstrated the capability for multispectral imaging. The second system used a photodiode as the detector and was designed to explore the phantom's application in pulse oximeter characterisation. This section presents the design and results of the camera-based detection system.

Validation System Design

The design of the system is illustrated in Figure 7.2. The illumination module comprised four light-emitting diodes (LEDs) with central wavelengths of 455, 530, 660, and 940 nm (LED1: M530L4, LED2: M455L4, LED3: M660L4, LED4: M940L4; Thorlabs). These LEDs were optically combined into a single beam using a set of dichroic mirrors: D1 (490 nm longpass, DMLP490R, Thorlabs), D2 (605 nm shortpass, DMSP605R, Thorlabs), and D3 (805 nm shortpass, DMSP805R, Thorlabs). Specific illumination wavelengths were selected by selectively activating individual LEDs or defined combinations. Reflected light from the phantom positioned above the light guide was captured by a monochrome camera (Flea3 FL3-U3-32S2M, FLIR) for analysis with a frame rate of 60 fps.

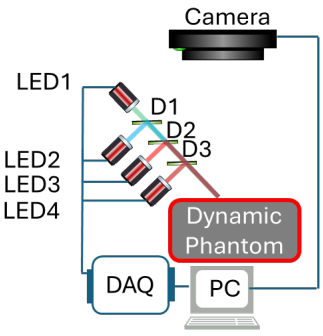

Figure 7.2: Scheme of the validation system using the camera.

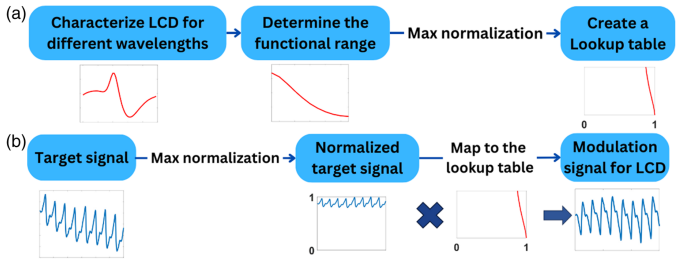

Figure 7.3: (a) Flowchart of dynamic phantom characterisation. (b) Flowchart of modulation signal synthesis.

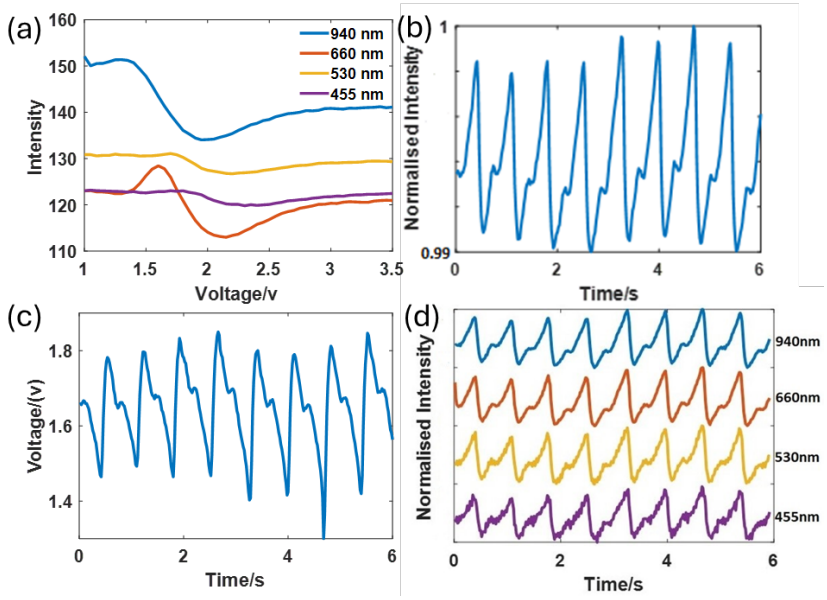

Figure 7.4: (a) Phantom characterisation results in reflection mode. (b) Rescaled PPG signal to be simulated. (c) Input signal to modulate LCD for 940 nm. (d) PPG signal measured by camera at 940 nm, 660 nm, 530 nm, and 455 nm.

Dynamic Signal Synthesis

The calibration procedure of the dynamic phantom is illustrated schematically in Figure 7.3(a). To characterise the optical response, the intensity of diffusely reflected light was measured while varying the voltage applied to the LCD from 0.5 to 3 V in 0.05 V increments. The voltage range in which the reflected intensity exhibited a negative correlation with the applied voltage was identified as the functional range. This response was then normalised to its maximum value to generate a lookup table. The signal synthesis process is summarised in the flowchart shown in Figure 7.3(b). The target signal was similarly normalised to its peak value and mapped onto the lookup table to produce the corresponding modulation pattern for the dynamic phantom. A PPG signal of 6 seconds from a healthy person[181] was used to generate the modulation signal for LCD.

Results

Figure 7.3 presents the characterisation and validation of the dynamic phantom. As shown in Figure 7.3(a), the intensity of the reflected light decreases with increasing voltage over a specific range. This range, where attenuation is inversely related to the applied voltage, is defined as the functional range of the system. In Figure 7.3(b), a target PPG signal is

rescaled and normalised. By mapping this signal to the phantom's response curve in Figure 7.3(a), a corresponding input voltage sequence was generated for the LCD, as shown in Figure 7.3. This input allowed the phantom to reproduce the shape and dynamics of the original signal. Figure 7.3(d) shows the validation result acquired using the camera-based detection system. The dynamic phantom successfully reproduced the PPG signal, although higher noise levels were observed at 530 nanometres and 455 nanometres. This is likely due to the limited modulation performance of the LCD at shorter wavelengths.

This design demonstrates the phantom's ability to simulate biological signals in a controllable and repeatable way. With further development, such as the integration of multiple light guides, the system has the potential to mimic vascular structures and support more advanced biomedical optical testing.

7.4 Application on Pulse Oximeter Characterisation

In this section, the light-guided dynamic phantom was further developed to replicate PPG signals for the purpose of pulse oximeter characterisation. The validation system used a photodiode for signal detection to better simulate the sensing mechanism used in commercial pulse oximeters. Synthetic PPG signals representing various heart rates (80 to 120 beats per minute) and oxygen saturation levels (86% to 100%) were generated and validated using the photodiode-based system. The results confirmed the phantom's ability to accurately reproduce dynamic biological signals in real time, demonstrating its potential for standardising and validating pulse oximeters. The application on pulse oximeter characterisation is described in Paper **II**.

The development of the light-guided dynamic phantom demonstrates how a controllable and repeatable platform can be used for the characterisation and validation of diverse biophotonics systems. Having presented the individual modalities, beam shaping strategies, and validation methods, the following chapter discusses these results in the context of current methodologies, highlighting their impact, limitations, and potential future directions.

Papers

Paper I

High contrast breast cancer biomarker semi-quantification and immunohistochemistry imaging using upconverting nanoparticles

S. Konugolu Venkata Sekar, H. Ma, K. Komolibus, G. Dumlupinar, M. J. Mickert, K. Krawczyk and S. Andersson-Engels.

Biomedical Optics Express **15**, 900-909 (2024).

High contrast breast cancer biomarker semi-quantification and immunohistochemistry imaging using upconverting nanoparticles

Sanathana Konugolu Venkata Sekar,[1,*,†] Hui Ma,[1,2,†] Katarzyna Komolibus[1], Gokhan Dumlupinar,[1,2] Matthias J. Mickert,[3] Krzysztof Krawczyk,[3] Stefan Andersson-Engels[1,2]

[1]*Biophotonics@Tyndall, IPIC, Tyndall National Institute, Lee Maltings Complex, Dyke Parade, T12R5CP, Cork, Ireland*
[2]*Department of Physics, University College Cork, College Road, Cork, T12 K8AF, Ireland*
[3]*Lumito AB, Mårtenstorget 5, SE-223 51 Lund, Sweden*
[†]*These authors contributed equally to this work*
**sanathana.konugolu@tyndall.ie*

Abstract: Breast cancer is the second leading cause of cancer death in women. Current clinical treatment stratification practices open up an avenue for significant improvements, potentially through advancements in immunohistochemistry (IHC) assessments of biopsies. We report a high contrast upconverting nanoparticles (UCNP) labeling to distinguish different levels of human epidermal growth factor receptor 2 (HER2), in HER2 control pellet arrays (CPAs) and HER2-positive breast cancer tissue. A simple Fourier transform algorithm trained on CPAs was sufficient to provide a semi-quantitative HER2 assessment tool for breast cancer tissues. The UCNP labeling had a signal-to-background ratio of 40 compared to the negative control.

1. Introduction

Accounting for 0.5 million deaths per year internationally, breast cancer is the most common form of cancer among women and constitutes a significant global health issue [1]. This high death toll persists even though the majority of women are now diagnosed with early-stage breast cancer, which is often curative with surgery, radiation therapy, and systemic therapy. Standard immunohistochemistry (IHC) labeling of tumor tissue biopsies, obtained by imaging molecular targets such as the estrogen receptor (ER), progesterone receptor (PR), and human epidermal growth factor receptor 2 (HER2) facilitates oncologists in determining both prognosis and treatment strategies for individual patients with breast cancer. The main advantages of the IHC technique lie in its high sensitivity and specificity, application to routinely available formalin fixed paraffin embedded samples, correlation to morphology and cost effectiveness [2]. However, despite its widespread use and incorporation into clinical practice guidelines, standard IHC has inherent limitations including low dynamic range, issues with quantification, subjectivity, multiplexing and co-localization [3-6].

For example, in a typical IHC workflow to determine the HER2 expression level a horseradish peroxidase 3,3'-diaminobenzidine (DAB) staining is used. The enzymatic oxidation of DAB generates an insoluble brownish precipitate at the location of the analyte. The completeness of the DAB precipitation along the cell membrane and the strength of the brown color are analyzed visually by pathologists to rather subjectively determine the HER2 level in a four category scoring system (0 to 3+) according to the current guidelines of American Society of Clinical Oncology/College of American Pathologists (ASCO/CAP) [7,8]. According to those guidelines, only HER2 3+ case, with complete and intense circumferential membrane staining for over 10% of the tumor cells, is considered HER2 positive. Currently, approximately 15% of women are diagnosed with HER2 positive breast cancer and receive HER2-targeted therapies such as trastuzumab, pertuzumab, or lapatinib [9]. The remaining 85% of diagnosed women fall into the negative category despite the fact that they can express weak to moderate

staining in over 10% of tumor cells (cases of HER2 1+ and 2+). Since the detection of HER2 3+ cases has been of greatest clinical significance so far, the optimization of HER2 testing has always been focused on differentiating positive from negative cases rather than four distinct categories [10, 11]. The recent introduction of new therapies, for example antibody conjugates like trastuzumab-deruxtecan, successfully targeting the sub-group of patients with lower HER2 levels [10, 12-14], poses a new challenge of accurate and reproducible assessment of HER2 scoring at its lower end. The high rate of discordance among pathologist scoring lower HER2 levels (0, 1+, 2+) and poor interrater reliability suggest that traditional IHC doesn't provide sufficient accuracy for clinical decision making [5, 15].

The challenges associated with chromogenic staining, such as DAB, open up a new avenue for improved quantifiable labling schemes and intelligent image analysis techniques to enable extraction of previously hidden information. In the last decade vast efforts have been undertaken to utilize machine learning (ML) and artificial intelligence (AI) algorithms based on conventional histopathological staining to obtain more objective diagnostic results, including prediction of diagnosis, prognosis and treatment response [16-22]. At the same time, immunofluorescence (IF) using fluorophore-labeled antibodies has become an alternative approach. Nevertheless, organic dyes typically used in IF exhibit quenching and broad emission, which makes them not suitable for quantitative analysis and multiplexing [23]. Advances in nanoparticle functionalization and bioconjugation, however, has laid the foundation for a new generation of fluorescent nanoprobes [24]. Numerous groups have explored the possibility of using quantum dots (QDs) [25-28] and Raman probes [29,30] for improved profiling of multiple biomarkers, but ideal label providing high contrast and high dynamic range imaging has yet to be found.

Upconverting nanoparticles (UCNPs) have recently emerged as a versatile fluorescence imaging platform with unique photophysical properties desirable in biomarker detection and imaging applications [31-34]. Due to their anti-Stokes shift, the autofluorescence of the background can be avoided yielding very high sensitivity, even down to single particle detection [35, 36]. This, in turn, enables high contrast measurements providing quantitative information about biomarker concentration and together with the narrow emission lines opens up the possibility of biomarker multiplexing. Moreover, the extremely high photostability of UCNPs is an advantage in comparison to other fluorescent dyes [37, 38]. These features make UCNPs ideal candidates to explore the avenue of digital pathology with multiplexed, sensitive and highly specific molecular detection. To date, the application of UCNP conjugates with different breast cancer cell lines have demonstrated excellent results with highly specific detection of the HER2 biomarker, yielding a 50-fold improvement in signal-to-noise ratio as compared to conventional fluorescent labeling under the same experimental conditions [39]. In addition, a multiplexed detection scheme of three common biomarkers, ER, PR and HER2, has been successfully demonstrated by employing the UCNP platform on breast cancer cell lines [40]. However, the majority of UCNP-biomarker labeling studies presented thus far use cancer cell lines rather than more complex histological samples and do not address the issue of biomarker quantification.

This study demonstrates the feasibility of using UCNPs as a promising candidate for high contrast breast cancer tissue labeling and brings up the potential for quantification of HER2 expression as opposed to standard DAB labeling. The novelty of the present work lies in the detection and semi-quantification of four distinct levels of HER2 (0, 1+, 2+, 3+) expressions in HER2 control pellet arrays (CPA), and in the demonstration of HER2 mapping in breast cancer tissue slides. In addition, a Fourier-transform-based image analysis method was developed to address the challenge of quantification of various levels of HER2 expressions. The imaging contrast achieved in the UCNP-labeled breast cancer tissue is compared with DAB-labeled slides and the contrast gain of UCNP over DAB is quantified.

2. Experiment description

We will here give a brief description of the study, with full details provided in the supplementary material S1. To investigate the suitability of UCNPs for the quantification of HER2 presence, CPAs (HistoCyte Laboratories Ltd, HCL028) with different levels of HER2 expression were incubated with anti-HER2 rabbit antibody, biotinylated anti-rabbit antibody, and finally labelled with streptavidin-PEG-UCNPs (NaYF4, with 2% Tm3+ and 18% Yb3+ doping). The average size (diameter inner circle) of UCNPs were around of 54 nm ± 1.7 nm (N = 155) as verified by TEM (Figure 1a). The UCNP-streptavidin labeling scheme is depicted in Figure 1b. In the first step, a primary rabbit anti-HER2 antibody binds to the HER2 antigen localized in the cell membrane. A secondary anti-rabbit antibody modified with biotin acts as an anchor to the UCNP-streptavidin conjugates. The excess UCNP labels are removed in a washing step. In addition, samples were counterstained with DAPI. For demonstrating on real HER2 breast cancer tissue, HER2 3+ breast cancer tissue slides were used for this study and they were labelled using the same process as described above.

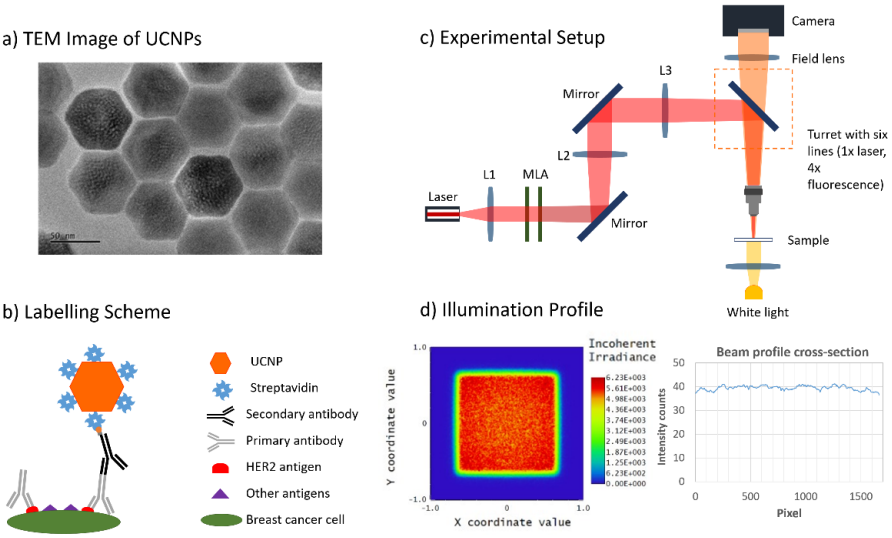

Fig. 1: a) TEM images of UCNPs used in this study b) scheme of the HER2 labeling with UCNP-streptavidin conjugates c) multimodal laser illumination microscope system d) uniform beam profile (Zemax simulation) and characterization of the beam profile of the 976 nm laser excitation line on the sample plane of the microscope.

The slides are subsequently analyzed employing a Köhler-illumination type user-built microscope system. The schematic of the microscope system is shown in Figure 1c. The system and its optical components were optimized in the Zemax OpticsStudio software to provide a uniform beam profile. Figure 1d shows the results of simulations and experimentally measured uniform beam profile on a UCNP test sample. The microscope includes additional excitation lines to perform H&E, DAPI, and DAB imaging.

To semi-quantify the UCNP labeling in the CPAs, the camera dark counts were first subtracted from recorded luminescence images. A schematic layout of the subsequent steps for semi-quantitatively assess the HER2 score in small sub-areas across the analysed images is shown in Figure 2. First, a subset of macro images of 201 x 201 pixels with centre at each pixel to be analysed were generated. The size of the macro images was selected to include a number of neighbouring cells, minimize any distortion to the subsequent Fourier transform due to the finite size of the image and to also have one center pixel. In step 1, each macro image was 2D Fourier transformed and a band-pass filter was applied in the spatial frequency domain. This

operation suppresses contributions of low frequency components, like background signals, while retaining the high-frequency components like the UCNP labeling of the cell membranes, and the completeness of UCNP HER2 labeling around the cell membrane. The parameters of the Fourier bandpass filter (inner and outer radius) were optimized to maximize the variation among the HER2 expression levels and capture the frequencies corresponding to circular HER2 expression around the cell membrane. Hence, the circular, high HER2 expression like 3+ has a relatively high contribution to filtered Fourier domain image as compared to non-circular lower HER2 expression (e.g. 1+, 0).

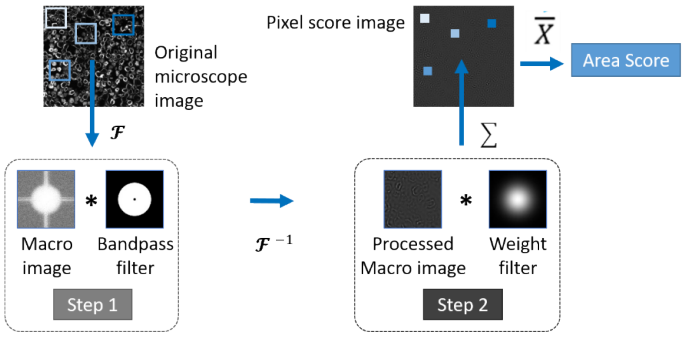

Fig. 2: Flow chart of the Fourier-transform image processing algorithm for the semi-quantification of the HER2 expression.

In step 2, the information is subsequently transformed back to the spatial domain and multiplied with a Gaussian weight filter with sigma value of 34 pixels. The weight filter ensures that the contribution of centre pixels in the macro image are dominating. All the 201x201 pixel values are then summed to create a single value for each macro image. This value is defined as the pixel score for the centre pixel, and the corresponding image generated by processing all macro images to pixel scores is called the pixel score image. Then area score is calculated as the mean of all pixels in pixel score image.

3. Results and discussion

For the bandpass filter in the spatial frequency domain of the images, an inner radius of 0.015 μm^{-1} and an outer radius of 0.92 μm^{-1}. The lower limit was chosen to eliminate the zero DC frequency and the upper limit is chosen as the highest frequency seen in HER2 3+ expression. Figure 3 a-d shows the results of UCNP labeled CPAs with Fourier transformed image and line profile of frequencies. Here, the completeness of the cell membrane and intensity of labeling is decreased with declining HER2 level from 3+ to 2+ which decreases further in HER2 1+, 0 samples as expected by the ASCO/CAP guidelines [41]. In other words, fewer UCNPs are bound to cells in the HER2 control pellets exhibiting lower HER2 expressions. The area score with standard deviation across the pixel score images for different HER2 expressions in CPA samples is shown in Figure 4. The area score provides a quantitative estimate of the HER2 expression for the entire CPA and increases with elevated HER2 expression levels. Thanks to the choice of the bandpass filter, the difference in area score for HER2 3+ and 2+ takes into account both the intensity of UCNP emission and the circular nature of HER2 expression as required by ASCO guidelines [41]. A similar area score of HER2 1+ and 0 was obtained. This can possibly be related to a minor amount of remaining UCNP clusters (non-specifically bound) present in the HER2 0 sample. Another explanation is the similarity of HER 1+, 0 expression making them hard to distinguish and quantify [10, 42]. Improved washing steps to remove the UCNP clusters from the tissue slides and a better filtering procedure could help in optimizing the quantification at low HER2 expression levels. Though these minor clusters are present in all slides, they make more impact on results obtained for HER2 1+ and 0 as these slides have a

minimal expression of HER2 receptors. However, our results in Figure 4 show that we can measure the expression despite the presence of traces of UCNP clusters in the slides.

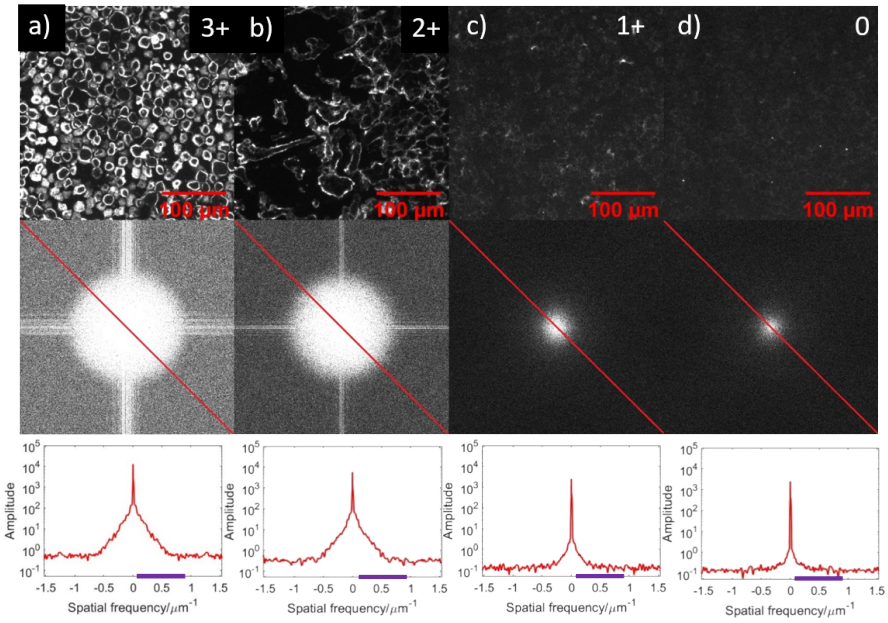

Fig. 3 Microscope images, corresponding 2D Fourier transforms of the images, and cross sections line profile through these transforms (band pass filter range is highlighted with a violet bar at the axis) for UCNP labeled HER2 CPA samples with different levels of HER2 expression a) 3+, b) 2+, c) 1+, and d) 0. Note: Top row images (c, d) has different intensity scale as compared to a, b to improve visualization of the images

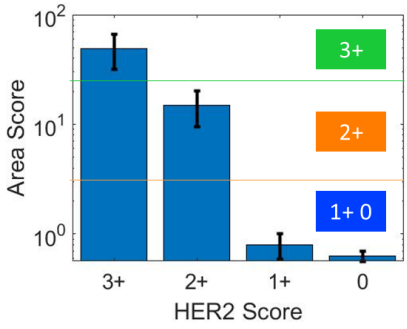

Fig. 4: Results of the HER2 quantification for different HER2 expression levels in a CPA with standard deviation as error bars and thresholds for semi-quantification of HER2 expression.

To demonstrate the novel approach of the semi-quantified analysis of the HER2 expression in breast cancer tissue, a HER2 3+ breast cancer tissue slide was labeled with UCNPs as described in Figure 1b. The UCNP image of the slide is shown in Figure 5a. The cancer tissue was also counterstained with 4′,6-diamidino-2-phenylindole (DAPI), which stains the nuclei of cells. An overlap between the UCNP labeling and the counterstain is provided in Figure 5b. UCNP labeling along with DAPI staining helps to demarcate the HER2 overexpressed cells in relation to HER2 negative cells. The HER2 expression in UCNP images was semi-quantified by the

Fourier method developed on the CPAs (Figure 2). The pixel score image of breast cancer tissue was generated using the data in Figure 5a. The pixel scores are further color coded based on the HER2 expression thresholds estimated in Figure 4. These HER2 expression levels are color coded and shown in Figure 5c. This provides a heat map of regions of different levels of HER2 expression. From this heat map it is evident that over 10% of cell area exhibits levels corresponding to HER2 3+ area scores. This is in line with the expected result for the imaged HER2 3+ breast cancer tissue. In addition, the signal-to-background value was calculated by taking the ratio of the peak counts in a UCNP labeled breast cancer image to the average of unspecific binding signal from a negative control breast cancer image acquired under the same experimental conditions. The signal-to-background value for the UCNP labeling was found to be 40.

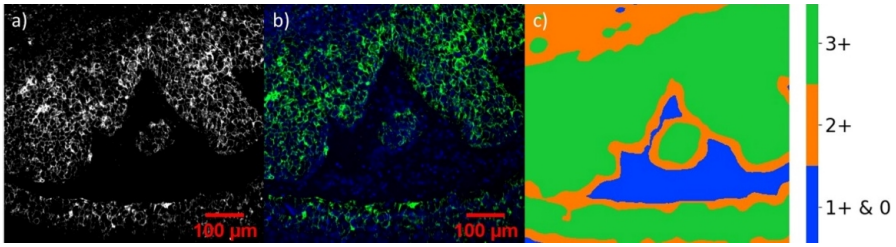

Fig. 5: a) UCNP labeled HER2 3+ breast cancer tissue image taken at 976 nm excitation of UCNP and 800 nm emission b) overlay of UCNP (green) with DAPI (blue) emission. c) Area score assessment of a HER2 3+ breast cancer tissue labeled with UCNP.

In order to make a meaningful comparison, the breast cancer tissue was also labeled with classical DAB. The DAB precipitation was found in the cell membrane of HER2 positive breast cancer cells. The signal-to-background for DAB was calculated by taking the ratio of average background with no labeling to DAB labeled section of the breast cancer image. The signal-to-background for DAB was found to be 1.6, more details regarding the calculation can be found in the supplementary material S1. The current clinical practice for breast cancer treatment stratification relies on gold standard IHC using the HRP/DAB visualization system to provide information about the overexpression of HER2 and other biomarkers in breast cancer tissue41. DAB is renowned for high thermal and chemical stability making it an ideal choice for labeling in these aspects. However, in the DAB labeling, the signal is generated by the absorption of white light by the chromogen. The light attenuated by the DAB is fundamentally limited by the pathlength of white light in the tissue slide. Hence, at high DAB concentrations, no light gets through the slide. The only way is then to reduce the primary antibody concentration and redo the labeling but this influences the sensitivity on the lower end, thus the overall dynamic range is limited. This implies that image contrast provided by any absorption-based agent is relatively poor, requiring expert pathology experience and complicating the diagnosis and stratification processes. DAB imaging with white light further complicates the quantification process as it will require calibration of color, possibly drifting over time. On the contrary, the contrast in UCNP-labeling is obtained by the emission process which allows it to be limited only by the non-specific labeling of surrounding tissue. In this work, the contrast of the UCNP images with respect to background was found to be 40. This gives an enhancement factor of 25 for UCNP labeling as compared to DAB labeling. The signal-to-background, achieved in this work, can be further improved by optimizing the labeling process.

In addition, breast cancer severity and treatment stratification is assessed based on the expression levels of multiple receptors like ER, PR, HER2, Ki-67. It is difficult to co-localize DAB labeling together with another chromogen to simultaneously provide expressions of multiple receptors - a new way to interpret breast cancer types for treatment stratification [43].

In contrast, the narrow emission lines of UNCPs can be designed to easily multiplex biomarkers on the same tissue slide. Alternatively, fluorophores can be considered substitutes for DAB, however, the key challenges constitute autofluorescence background and photo-bleaching. Novel fluorophores like quantum dots can partially address photo-bleaching, but they still pose the challenge of auto-fluorescence background [44]. On the contrary, UCNP anti-Stokes' shifted emission eliminates the challenge of Stokes-shifted auto-fluorescence. UCNPs are also known for their high photostability even at high excitation powers.

In recent times, the increase in computation power has given rise to the development of novel AI/ML tools for pathological image analysis. The AI/ML tools are foreseen to create a new paradigm in histopathology to provide accurate predictions and aid pathologists in decision-making [8, 16, 45, 46]. The performance of AI/ML models is enhanced when the contrast is high allowing models to effectively distinguish target receptors from the background. The above discussion highlights some of the key advantages of UCNPs in terms of multiplexing for multi-receptor labeling, high contrast for enhanced ML/AI training methods, zero auto-fluorescence background and high photo-stability as compared to other emerging fluorophores like quantum dots.

4. Conclusions

For the first time, we have reported the use of high contrast UCNP labeling to distinguish different levels of HER2 expression in HER2 CPA and HER2 positive breast cancer tissue. A simple Fourier transform algorithm trained on CPAs was sufficient to provide an objective semi-quantitative HER2 tissue assessment tool as demonstrated on a tissue sample. The UCNP breast cancer labeling was found to have a signal-to-background of 40 compared to the negative control, which is an enhancement of 25 times as compared to conventional DAB labeling. With an urgent need for better biomarker quantification and multiplexing methods for improved treatment stratification, the development of UCNP imaging and advancements in labeling processes shows great promise to be included in the clinical practice in the future as a reliable and accurate diagnostic tool.

Funding. Science Foundation Ireland SFI/15/RP/2828.

Disclosures. Lumito AB is developing histopathology products based on UCNPs. SAE is a co-founder and shareholder of Lumito AB.

Data availability. Data underlying the results presented in this paper are not publicly available at this time but may be obtained from the authors upon reasonable request.

Supplemental document. See supplementary S1 for supporting content.

References

1. S. Lei, R. Zheng, S. Zhang, S. Wang, R. Chen, K. Sun, H. Zeng, J. Zhou, W. Wei, "Global Patterns of Breast Cancer Incidence and Mortality: A Population-Based Cancer Registry Data Analysis from 2000 to 2020." Cancer Commun 41 (11), 1183–1194 2021.
2. AACR Pathology Task Force, "Pathology: hub and integrator of modern, multidisciplinary [precision] oncology." Clinical Cancer Research 28.2, 265-270 (2022).
3. D. Furrer, F. Sanschagrin, S. Jacob, C. Diorio, "Advantages and Disadvantages of Technologies for HER2 Testing in Breast Cancer Specimens." Am J Clin Pathol 144 (5), 686–703 (2015).
4. D.L. Rimm, "What Brown Cannot Do for You" Nature biotechnology 24.8, 914-916 (2006).
5. C. J. Robbins et al. "Multi-institutional assessment of pathologist scoring HER2 immunohistochemistry." Modern Pathology 36.1, 100032 (2023).
6. H. Nitta, B. Kelly, C. Allred, S. Jewell, P. Banks, E. Dennis, T. Grogan, "The Assessment of HER2 Status in Breast Cancer: The Past, the Present, and the Future." Pathol Int 66 (6), 313–324 (2016).

7. A. Wolff, et al. “Human Epidermal Growth Factor Receptor 2 Testing in Breast Cancer: American Society of Clinical Oncology/College of American Pathologists Clinical Practice Guideline Focused Update.” Arch Pathol Lab Med 142 (11), 1364–1382 (2018).
8. M. Bui, et al. "Quantitative image analysis of human epidermal growth factor receptor 2 immunohistochemistry for breast cancer: Guideline from the College of American Pathologists." Archives of pathology & laboratory medicine 143.10, 1180-1195 (2019).
9. S. Loibl, L. Gianni, L. “HER2-Positive Breast Cancer.” The Lancet 389 (10087), 2415–2429 (2017).
10. X. Baez-Navarro, R. Salgado, C. Denkert, J. Lennerz, F. Penault-Llorca, G. Viale, J. Bartlett, C. van Deurzen, “Selecting Patients with HER2-Low Breast Cancer: Getting out of the Tangle.” Eur J Cancer 175, 187–192 (2022).
11. T. J. A. Dekker, “HER2-Targeted Therapies in HER2-Low-Expressing Breast Cancer.” Journal of Clinical Oncology 38 (28), 3050–3051 (2020).
12. C. Molinelli, F. Jacobs, C. Marchiò, F. Pitto, M. Cosso, S. Spinaci, E. De Azambuja, F. Schettini, E. Agostinetto, M. Lambertini, “HER2-Low Breast Cancer: Where Are We?” Breast Care 17 (6), 533–545 (2022).
13. D. Eiger, E. Agostinetto, R. Saúde-Conde, E. de Azambuja, “The Exciting New Field of HER2-Low Breast Cancer Treatment.” Cancers (Basel) 13 (5), 1–18 (2021).
14. P. Tarantino et al., “HER2-Low Breast Cancer: Pathological and Clinical Landscape.” Journal of Clinical Oncology 38 (17), 1951–1962 (2020).
15. D. L. Rimm, S. Dacic, S. J. Schnitt. "The Pathologists' Conundrum." Archives of Pathology & Laboratory Medicine 147.1 17-18 (2023).
16. M. Yousif, P. J. van Diest, A. Laurinavicius, D. Rimm, J. van der Laak, A. Madabhushi, S. Schnitt, L. Pantanowitz, “Artificial Intelligence Applied to Breast Pathology.” Virchows Archiv 480:1 2021, 480 (1), 191–209 (2021).
17. A. Kleppe, O. Skrede, S. De Raedt, K. Liestøl, D. Kerr, H. Danielsen, “Designing Deep Learning Studies in Cancer Diagnostics.” Nature Reviews Cancer 21:3 2021, 21 (3), 199–211 (2021).
18. J. van der Laak, G. Litjens, F. Ciompi, “Deep Learning in Histopathology: The Path to the Clinic.” Nature Medicine 27:5 2021, 27 (5), 775–784 (2021).
19. A. Echle, N. Rindtorff, T. Brinker, T. Luedde, A. Pearson, J. Kather, “Deep Learning in Cancer Pathology: A New Generation of Clinical Biomarkers. British Journal of Cancer.” Springer Nature pp 686–696 (2021).
20. L. Roszkowiak, A. Korzynska, K. Siemion, J. Zak, D. Pijanowska, R. Bosch, M. Lejeune, C. Lopez. „System for Quantitative Evaluation of DAB&H-Stained Breast Cancer Biopsy Digital Images (CHISEL).” Scientific Reports 11:1 2021, 11 (1), 1–14 (2021).
21. Y. Fu, A. Jung, R. Torne, S. Gonzalez, H. Vöhringer, A. Shmatko, L. Yates, M. Jimenez-Linan, L. Moore, M. Gerstung, “Pan-Cancer Computational Histopathology Reveals Mutations, Tumor Composition and Prognosis.” Nature Cancer 1 (8), 800–810 (2020).
22. S. Wu et al. “The Role of Artificial Intelligence in Accurate Interpretation of HER2 Immunohistochemical Scores 0 and 1+ in Breast Cancer.” Mod Pathol 36 (3), 100054 (2023).
23. U. Resch-Genger, M. Grabolle, S. Cavaliere-Jaricot, R. Nitschke, and T. Nann, "Quantum dots versus organic dyes as fluorescent labels," Nat. Methods 5(9), 763–775 (2008).
24. M. Yezhelyev et al. "Emerging use of nanoparticles in diagnosis and treatment of breast cancer." The lancet oncology 7.8 657-667 (2006).
25. P. Zrazhevskiy, X. Gao, “Quantum Dot Imaging Platform for Single-Cell Molecular Profiling.” Nature Communications 4 (1), 1–12 (2013).
26. J. Liu et al., “Molecular Mapping of Tumor Heterogeneity on Clinical Tissue Specimens with Multiplexed Quantum Dots.” ACS nano 4.5 2755-2765 (2010).
27. X. Wu, H. Liu, J. Liu, K. Haley, J. Treadway, J. Larson, N. Ge, F. Peale, M. Bruchez, “Immunofluorescent Labeling of Cancer Marker Her2 and Other Cellular Targets with Semiconductor Quantum Dots.” Nature Biotechnology 21 (1), 41–46 (2002).
28. M. Miyashita, K. Gonda, H. Tada, M. Watanabe, M. Kitamura, T. Kamei, H. Sasano, T. Ishida, N. Ohuchi, “Quantitative Diagnosis of HER2 Protein Expressing Breast Cancer by Single-Particle Quantum Dot Imaging.” Cancer Med 5 (10), 2813–2824 (2016).
29. C. Chen, Z. Zhao, N. Qian, S. Wei, F. Hu, W. Min, “Multiplexed Live-Cell Profiling with Raman Probes.” Nature Communications 12 (1), 1–13 (2021).
30. T. Nayak, C. Andreou, A. Oseledchyk, W. Marcus, H. Wong, J. Massagué, M. Kircher, “Tissue Factor-Specific Ultra-Bright SERRS Nanostars for Raman Detection of Pulmonary Micrometastases.” Nanoscale 9 (3), 1110–1119 (2017).
31. A. Hlaváček, Z. Farka, M. Mickert, U. Kostiv, J. Brandmeier, D. Horák, P. Skládal, F. Foret, H. H. Gorris, “Bioconjugates of Photon-Upconversion Nanoparticles for Cancer Biomarker Detection and Imaging.” Nature Protocols. Nature Research pp 1028–1072 (2022).
32. C. Chen et al., “Multi-Photon near-Infrared Emission Saturation Nanoscopy Using Upconversion Nanoparticles.” Nature Communications 9 (1), 1–6 (2018).
33. C. Liu, Y. Qi, R. Qiao, Y. Hou, K. Chan, Z. Li, J. Huang, L. Jing, J. Du, M. Gao, “Detection of Early Primary Colorectal Cancer with Upconversion Luminescent NP-Based Molecular Probes.” Nanoscale 8 (25), 12579–12587 (2016).
34. B. Del Rosal, D. Jaque. "Upconversion nanoparticles for in vivo applications: limitations and future perspectives." Methods and Applications in Fluorescence 7.2 022001 (2019).

35. Z. Farka, M. Mickert, A. Hlaváč, H. Ek, P. Skládal, H. H. Gorris, “Single Molecule Upconversion-Linked Immunosorbent Assay with Extended Dynamic Range for the Sensitive Detection of Diagnostic Biomarkers.” Analytical chemistry 89.21 11825-11830 (2017).
36. M. Mickert, et al. "Measurement of sub-femtomolar concentrations of prostate-specific antigen through single-molecule counting with an upconversion-linked immunosorbent assay." Analytical chemistry 91.15 9435-9441 (2019).
37. S. Wu, G. Han, D. Milliron, S. Aloni, V. Altoe, D. Talapin, B. Cohen, J. Schuck, “Non-Blinking and Photostable Upconverted Luminescence from Single Lanthanide-Doped Nanocrystals.” Proc Natl Acad Sci U S A 106 (27), 10917–10921 (2009).
38. M. Haase, H. Schäfer,“Upconverting Nanoparticles.” Angewandte Chemie - International Edition 2011, 50 (26), 5808–5829 (2011).
39. Z. Farka, M. Mickert, Z. Mikušová, A. Hlaváček, P. Bouchalová, W. Xu, P. Bouchal, P. Skládal, H. H. Gorris, “Surface Design of Photon-Upconversion Nanoparticles for High-Contrast Immunocytochemistry.” Nanoscale 12 (15), 8303–8313 (2020).
40. L. Zhou, R. Wang, C. Yao, X. Li, C. Wang, X. Zhang, C. Xu, A. Zeng, D. Zhao, F. Zhang, “Single-Band Upconversion Nanoprobes for Multiplexed Simultaneous in Situ Molecular Mapping of Cancer Biomarkers.” Nat Commun 6 (2015).
41. S. Ahn, J. Woo, K. Lee, S. Park, “HER2 Status in Breast Cancer: Changes in Guidelines and Complicating Factors for Interpretation.” J Pathol Transl Med 54 (1), 34–44 (2020).
42. I. Rubin, Y. Yarden,”The Basic Biology of HER2.” Annals of Oncology 12 (SUPPL. 1), S3–S8 (2001).
43. W. Tan et al. “Overview of Multiplex Immunohistochemistry/Immunofluorescence Techniques in the Era of Cancer Immunotherapy.” Cancer Commun 40 (4), 135–153 (2020).
44. J. Bailes, “Photostability of Semiconductor Quantum Dots in Response to UV Exposure.” In Methods in Molecular Biology (2020).
45. H. Masmoudi, S. Hewitt, N. Petrick, K. Myers, M. Gavrielides, “Automated Quantitative Assessment of HER-2/Neu Immunohistochemical Expression in Breast Cancer.” IEEE Trans Med Imaging 28 (6), 916–925 (2009).
46. B. Hall, M. Ianosi-Irimie, P. Javidian, W. Chen, S. Ganesan, D. Foran, “Computer-Assisted Assessment of the Human Epidermal Growth Factor Receptor 2 Immunohistochemical Assay in Imaged Histologic Sections Using a Membrane Isolation Algorithm and Quantitative Analysis of Positive Controls.” BMC Med Imaging 8, 1–13 (2008).

Paper II

Light-guided dynamic phantom to mimic microvasculature for biomedical applications: an exploration for pulse oximeter

H. Ma, D. Angelone, C. N. Guadagno, S. Andersson-Engels and S. Konugolu Venkata Sekar.

Journal of Biomedical Optics **29(S3)**, S33312 (2024).

Light-guided dynamic phantom to mimic microvasculature for biomedical applications: an exploration for pulse oximeter

Hui Ma,[a,b] Dario Angelone,[a,b] Claudia Nunzia Guadagno,[d] Stefan Andersson-Engels,[a,c,d] Sanathana Konugolu Venkata Sekar [a,c,d,*]

[a]Biophotonics@Tyndall, Tyndall National Institute, Cork, Ireland
[b]School of Engineering Science, University College Cork, Cork, Ireland
[c]School of Physics, University College Cork, Cork, Ireland
[d]BioPixS Ltd., Cork, Ireland

Abstract

Significance: Dynamic phantoms capable of changing optical properties by control are essential for standardizing and calibrating spectroscopy systems such as the pulse oximeter. However, current liquid dynamic phantoms containing human blood have a short shelf life and require complex experimental setups. Some solid dynamic phantoms are influenced by the angular dependent performance of the liquid crystal display (LCD), some have a low spatial resolution, and some have slow control of optical properties.

Aim: This work aimed to develop a solid dynamic phantom which can overcome these obstacles by changing the optical properties rapidly and generating dynamic biological signals.

Approach: The absorption properties of the phantom can be controlled in real time by modulating an LCD. A light guide was employed to avoid the angular-dependent performance of the LCD by isolating the scattering top-layer tissue-mimicking silicone phantom from the LCD.

Results: The dynamic phantom were characterized at 940 nm, 660 nm, 530 nm, and 455 nm to create a lookup table. Photoplethysmography signals of different heart rates from 80 to 120 beats per minute were synthesized and oxygen saturation levels at 86%, 90%, 95%, and 100% were generated at multiple wavelengths.

Conclusions: The design, characterization, and potential applications of the dynamic phantom have been presented. This dynamic phantom can simulate various biological signals by applying corresponding modulation signals and has the potential of calibrating and validating pulse oximeter, imaging, and spectroscopy systems.

Keywords: dynamic phantom, pulse oximeter, photoplethysmography, standardization, near infrared spectroscopy, diffuse optics

* Sanathana Konugolu Venkata Sekar**,** E-mail: sanathana.konugolu@tyndall.ie
Hui Ma, E-mail: hui.ma@tyndall.ie

1 Introduction

Biomedical sensing and imaging play a crucial role in modern clinical analysis, providing visualizations of body tissues, facilitating non-invasive or minimally invasive diagnostic information, and offering real-time surgical guidance[1,2]. It helps to reduce the time and cost of diagnosis and treatment, as well as improve patient satisfaction. However, the lack of standards

for evaluating devices and comparing systems across the field hampers both technological advancement and the clinical translation of optical sensing and imaging systems[3,4]. Hemoglobin concentration in human blood is an important parameter to monitor the physiological condition. It gives information on the capability of oxygen transportation in blood, provides preoperative and postoperative care, helps to diagnose diseases like anemia, evaluates treatment response, and assesses the performance of athletes[5-10]. With the emergence of portable and wearable health monitoring devices, there is an increasing demand for optical standards capable of dynamically changing their optical properties to replicate changes in hemoglobin oxygen saturation during the respiratory and heart-beat cycle. Biophotonics phantoms are artificial structures designed to simulate the optical properties of biological media. They are essential tools for simulating light distribution with the geometry of physical tissues, validating, and characterizing the performance of optical devices, and recording reference measurements[11]. Many different phantoms with high stability, controllability, and repeatability have been developed for device calibration, optimization, and quality control[12-16].

Researchers have developed liquid phantoms using whole blood or extracted erythrocytes to mimic changes in oxygen saturation. However, the use of blood components could raise ethical and safety concerns and limit the stability and shelf life of the phantoms. Also, biological variability in blood components reduces the reproducibility of the phantom. To maintain the appropriate conditions, temperature and pH must be monitored throughout the entire measurement process. The use of temperature and pH monitors, peristaltic pumps and membrane oxygenators increases the cost and complexity of the experimental setup. Oxygen saturation levels are modulated by adding oxygenating compounds like oxygen and deoxygenating compounds such as yeast or nitrogen bubbling or a mixture of D-glucose, glucose oxidase and catalase[17-23]. A

63 peristaltic pump is used for blood circulation, and a membrane oxygenator is applied to control
64 blood oxygenation. Yeast takes 20 -30 minutes to gradually deoxygenate the phantom[21], and
65 nitrogen bubbling takes 30 minutes to effectively deoxygenate the phantom[22], which limits the
66 potential for real-time control.

67 Several solid dynamic phantoms have been developed to control changes in the absorption
68 coefficient with high stability and reproducibility. Koh et al.[24] designed a dynamic phantom with
69 a liquid-crystal display (LCD) sandwiched between the solid tissue-mimicking phantom. The
70 absorption at each pixel is electronically controlled to be on or off state. Funane et al.[25] developed
71 a phantom with two stage-driven absorber layers to realize gradual absorption changes by tuning
72 the position of the absorber. Hebden et al.[26] proposed a phantom with embedded targets comprising
73 a black thermochromic pigment. The pigment changes from black to white when heated to 47 °C.
74 However, the performance of the LCD-based dynamic phantom was largely influenced by the
75 scattering properties of the top layer phantoms since the attenuation of LCD is angular dependent.
76 The phantom with moving stages only creates macroscopic changes in tissue, it lacks the potential
77 of simulating complex structures such as vascular systems. For the thermochromic dynamic
78 phantom, the smallest spacing between targets is 11.2 mm to avoid crosstalk from the neighboring
79 target, thereby limiting the spatial resolution. Additionally, it takes approximately 70 seconds to
80 change the color from room temperature, which is not appropriate for fast control.

81 In this work, we implemented a novel light guide-based dynamic phantom to overcome the
82 challenges mentioned above[27]. This phantom utilized a polymer optical fiber to isolate the LCD
83 from the top layer tissue mimicking phantom and avoid angular dependent performance. The
84 absorption was tuned gradually by applying different voltages to the LCD. The phantom was
85 characterized at 4 wavelengths: 455 nm, 530 nm, 660 nm, and 940 nm, covering both visible and

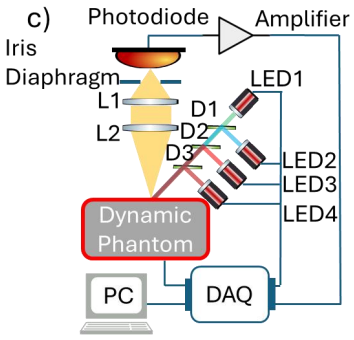

Fig. 1 c) Scheme of the validation system.

near-infrared ranges. As case studies, photoplethysmography (PPG) signals of different heart rates and oxygen saturation levels were generated by the dynamic phantom and tested by a photodiode. This dynamic phantom can be a helpful tool for calibrating and validating pulse oximeter, imaging system, and spectroscopy devices.

2 Method and Material

2.1 Phantom Design

Fig. 7.1(a) from Chapter 7 shows the photo of the dynamic phantom. Fig. 7.1(b) from Chapter 7 illustrates the schematic layout of the dynamic phantom. The light passing through a static tissue-mimicking silicone phantom was collected by a 4 cm long 3 mm diameter polymer optical fiber (OMPF3000, The Optoelectronic Manufacturing Corporation (UK) Ltd.) and collimated by a condenser lens (ACL2520U, Thorlabs) to avoid the angular dependent performance of the LCD. The parallel beam was modulated by the LCD (FOS-NIR (1100), LC-Tec Displays AB) and then reflected through the phantom by a silver mirror (PF10-03-P01, Thorlabs). The LCD was

100 controlled by a NI DAQ (USB-6212, National Instrument). The thickness and optical properties
101 of the static superficial silicone phantom can vary depending on the application. In our
102 demonstration, a 9 cm diameter, 0.5 mm thick round shape silicone phantom was used based on
103 the recipe described in Ref. 15. Briefly, the silicone phantom consisted of SiliGlass (MB
104 Fibreglass, UK) as bulk material, polycraft black silicone pigment (MB Fibreglass, UK) as
105 absorber, and silica microspheres (440345, Sigma-Aldrich) as scatterer. The optical properties of
106 this silicone phantom were characterized by a time-domain diffuse optical spectrometer[28,29]. The
107 target absorption coefficient (μ_a) was 0.1 cm^{-1}, and the reduced scattering coefficient (μ_s') was 10
108 cm^{-1}.

109 *2.2 Phantom Characterization System*

110 The full dynamic phantom was further characterized by an in-house system described in Fig. 1c).
111 The illumination part of the system consisted of four LEDs at 455 nm, 530 nm, 660 nm, and 940
112 nm (LED1: M530L4, LED2: M455L4, LED3: M660L4, and LED4: M940L4, Thorlabs). Dichroic
113 mirrors (D1: 490 nm longpass dichroic mirror (DMLP490R, Thorlabs), D2: 605 nm shortpass
114 dichroic mirror (DMSP605R, Thorlabs). D3: 805 nm shortpass dichroic mirror (DMSP805R,
115 Thorlabs)) were employed to combine these LEDs into one single beam. The illumination
116 wavelengths were selected by switching on or off any LED or any combination of LEDs. The
117 reflected light from the phantom above the light guide was collected by a two-lens system (L1:
118 AC254-050-AB-ML, L2: LB1676-ML, Thorlabs) and measured by a photodiode (S3590-08,
119 Hamamatsu Photonics) with an amplifier (DLPCA-200, FEMTO Messtechnik GmbH) and fed
120 into the DAQ (USB-6212, National Instrument).

2.3 Dynamic Signal Synthesis

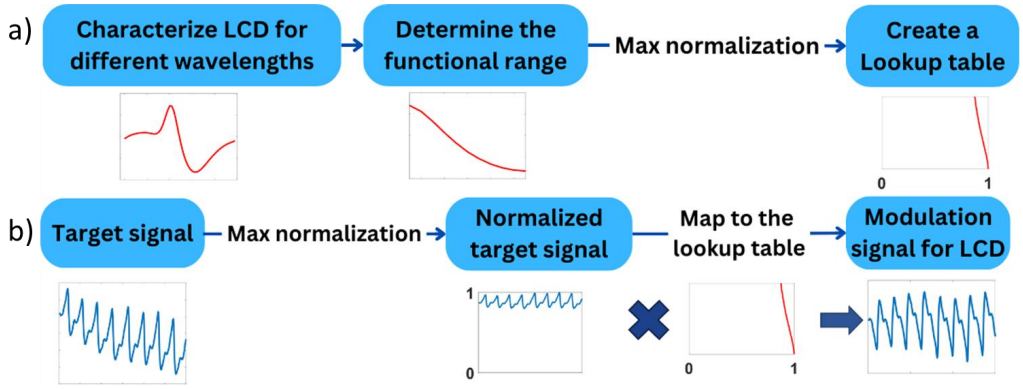

Fig. 2 a) Flowchart of dynamic phantom characterization. b) Flowchart of modulation signal synthesis

The process flow of phantom calibration is schematically described in Fig. 2a). The intensity of the diffusely reflected light from the dynamic phantom was characterized by applying a voltage over the LCD from 0.5 V to 3 V with a 0.05 V step size. The range in which this intensity was negatively correlated to the applied voltage was determined as the functional range. The response of this functional range was normalized to the maximum value to create a lookup table. The flowchart of the synthesis of the target signal is illustrated in Fig. 2b). The target signal was also normalized to its maximum value to allow it to be mapped to the lookup table to get the modulate signal for the dynamic phantom.

2.4 Photoplethysmography Simulation

Two application case studies were implemented to demonstrate the dynamic phantom's ability to reproduce different PPG signals at multiple wavelengths. One case study focused on generating PPG signals at various heart rates, while the other showcased the generation of PPG signals at different oxygen saturation levels.

For the heart rate simulation case study, the target synthetic PPG signals with heart rates ranging from 80 to 120 beats per minute (bpm) in steps of 10 bpm were generated using the Python toolbox NeuroKit2[30]. Each PPG signal contains 20,000 data points (20 seconds) sampled at 1000 Hz. The phantom modulation voltage signals were generated by mapping synthetic PPG signals to the lookup table as described in Section 2.3. The dynamic phantom was modulated and measured by the phantom characterization system as described in Section 2.2 at 50 Hz sampling rate. The measured signals were then processed by NeuroKit2 to recover the heart rate[30].

For the oxygen saturation case study, the wavelengths 660 nm and 940 nm were selected for the characterization to enable an evaluation of different oxygen saturation levels, as these wavelengths are commonly used in commercial medical pulse oximeters. A single measured PPG signal recording of six seconds from a healthy volunteer[31] was used. It was normalized to the maximum value. Targeted signal traces for two selected wavelengths and five tested blood oxygenation levels were then generated from this normalized single trace by adjusting the modulation depth according to the blood attenuation.

These traces were then mapped to the lookup table to generate the modulated voltage signal for the dynamic phantom input. The phantom was measured by using the phantom characterization system as described in section 2.2 at a 50 Hz sampling rate. The oxygen saturation can be obtained from measured PPG signals at these wavelengths through a double ratio of the pulsatile and non-pulsatile components of the measured red and near infrared light[32,33]

$$R = \frac{ln\frac{I_{\max}(\lambda_{660})}{I_{min}(\lambda_{660})}}{ln\frac{I_{\max}(\lambda_{940})}{I_{min}(\lambda_{940})}} \quad , \qquad (1)$$

where $I_{\max}(\lambda_{660})$ is the maximum amplitude of the pulse at 660 nm, $I_{min}(\lambda_{660})$ is the minimum amplitude of the pulse at 660 nm, $I_{\max}(\lambda_{940})$ is the maximum amplitude of the pulse at 940 nm, and $I_{min}(\lambda_{940})$ is the minimum amplitude of the pulse at 940 nm.

158 In the region of 86% to 100%, oxygen saturation (SpO_2) shows a linear correlation with the R
159 rate[34]

160 $$SpO_2 = -24.87R + 113.8 \quad . \tag{2}$$

161 The R rate can thus simply be calculated by

162 $$R = (113.8 - SpO_2)/24.87 \tag{3}$$

163 The linear range was simulated in this case study. The R rate was calculated at every pulse,
164 and then the values were averaged over a 6-second sample. Target signals of different wavelengths
165 and oxygen saturation levels were measured one by one. The relative change in the absorption
166 coefficient of arterial component of blood at 660 nm is 130% when changing from 100% to 86%
167 oxygen saturation level, while at 940 nm, the relative absorption coefficient variation is only 6%.[35]
168 Since the extinction coefficient of blood does not change significantly from 86% to 100% SpO_2 at
169 940 nm, we kept the amplitude constant at 940 nm and modulated the amplitude at 660 nm to
170 simulate SpO_2 level at 86%, 90%, 95%, and 100%.

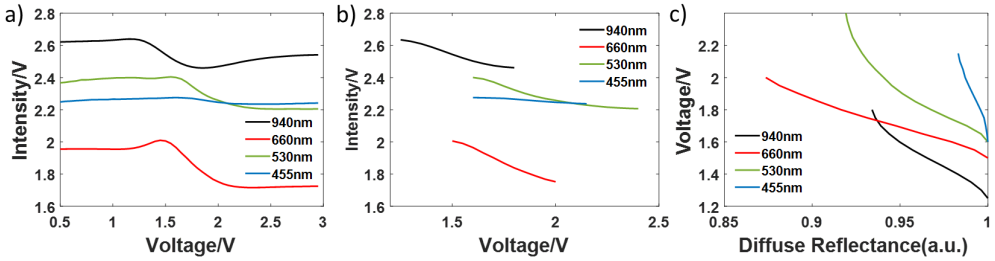

Fig. 3 a) Characterization results of the dynamic phantom. b) Characterization results of the dynamic phantom in the functional range. c) Lookup table for the dynamic phantom.

3 Results

3.1 Dynamic Phantom Characterization

The results of the full dynamic phantom characterization are presented in Fig. 3a). Here the diffusely reflected light intensity from the phantom was measured at four wavelengths as a function of the voltage applied over the LCD. Within a certain voltage range (1.2 V - 2.4 V), this intensity was negatively correlated to the applied voltage. This voltage range was identified as the functional range, as illustrated in Fig. 3b). The lookup tables formed after normalizing the curve within the functional range for each wavelength are shown in Fig. 3c). The maximal modulation depths are 7% at 940 nm, 13% at 660 nm, 8% at 530 nm, and 2% at 455 nm. The measured optical

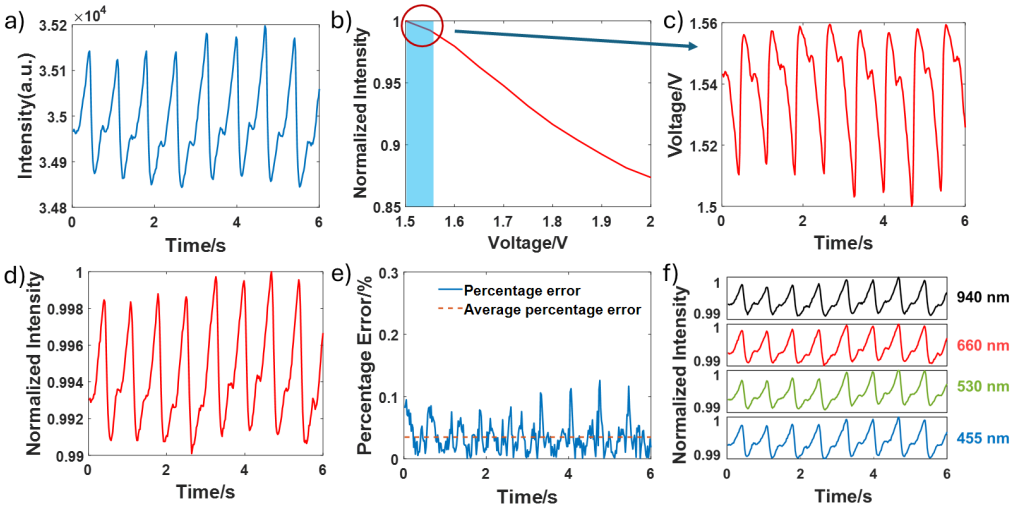

Fig. 4 a) Target PPG signal from literature. b) Normalized diffuse reflectance response at 660 nm. c) Modulation signals for LCD at 660 nm to generate PPG signals. d) PPG signals generated by the dynamic phantom and measured at 660 nm. e) Percentage error between target and measured signal after max normalization of target signal and the average percentage error. f) PPG signals generated by the dynamic phantom and measured at 940 nm, 660 nm, 530 nm, and 455 nm.

properties of the static top-layer silicone phantom were found to be μ_a = 0.12 cm^{-1}, μ_s' = 10.2 cm^{-1} at 660 nm, and μ_a = 0.1 cm^{-1}, μ_s' = 6.5 cm^{-1} at 940 nm, close to the targeted values.

3.2 Photoplethysmography signals synthesis

Next, we demonstrate the capability of the dynamic phantom to replicate a targeted PPG trace using 660 nm as an example. Fig. 4 shows the steps taken to generate a PPG trace at 660 nm, using the above-mentioned experimentally measured trace from Ref. 31 as a target (Fig. 4a). The normalized diffuse reflectance response within the functional range of the dynamic phantom at 660 nm is shown in Fig. 4b). The resulting modulation signal required for the LCD to generate the targeted diffuse reflectance from the dynamic phantom is presented in Fig. 4c). This trace is generated by mapping the normalized original signal to the generated lookup table. Fig. 4d) shows the reproduced PPG signals measured by the photodiode at 660 nm, while the percentage error and average percentage error between the target signal (Fig. 4a) and the measured signal after max normalization of the target signal are shown in Fig. 4e). The average percentage errors are 0.03% at 940 nm, 0.03% at 660 nm, 0.05% at 530 nm, and 0.3% at 455 nm. Measured diffuse reflectance traces at four wavelengths are given in Fig. 4f). The results demonstrate that the dynamic phantom can successfully simulate PPG signals at multiple wavelengths.

To demonstrate the phantom's ability to generate dynamic biological signals, two case studies were conducted to generate PPG signals of different heart rates and oxygen saturation levels at multiple wavelengths.

3.3 Case study 1: PPG signals of different heart rates

Fig. 5a) shows 20-second PPG-like signal traces measured from the dynamic phantom for heart rates of 80, 90, 100, 110, and 120 bpm at 940 nm. Each trace shows clear periodicity

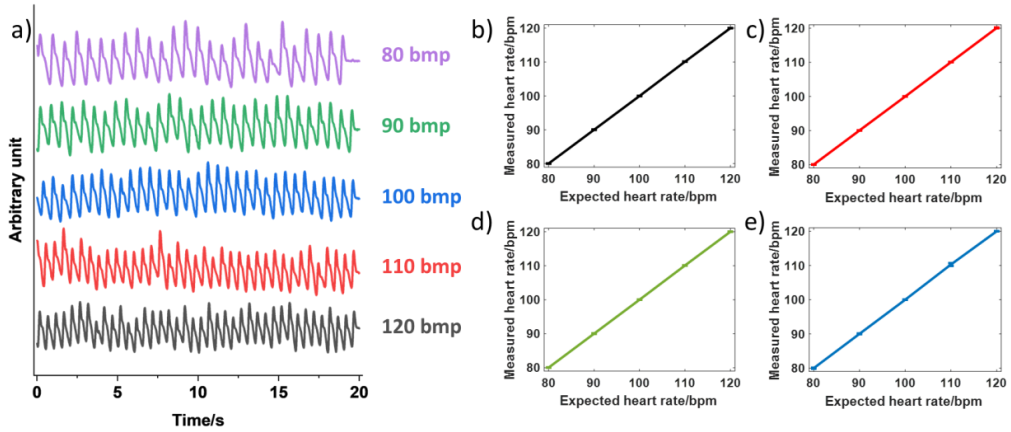

Fig. 5 a) Offset plot of measured signals at 940 nm. Expected vs. measured heart rate at b) 940 nm, c) 660 nm, d) 530 nm, and e) 455 nm.

corresponding to the designated heart rates, indicating the ability of the dynamic phantom to realistic cardiac rhythms. Figs 5b-5e) compare the expected heart rates to the measured heart rates at 940 nm, 660 nm, 530 nm, and 455 nm. The R^2 values of the linear regression at these four wavelengths are 0.999. The good agreement between the expected and measured values validates the accuracy of the dynamic phantom in replicating various heart rates, demonstrating its potential for calibrating and validating heart rate monitors.

3.4 Case study 2: PPG signal of different oxygen saturation levels

Fig. 6a) shows the target signals at different oxygen saturation levels. Fig. 6b) illustrates the measurement results at different oxygen saturation levels. The measured signals demonstrate clear amplitude variations that correlate with the specified oxygen saturation levels. Fig. 6c) presents the measured R-value as a function of the expected SpO_2 levels, indicating a linear decrease in the R-value with increasing SpO2. This result aligns with the conclusion of Ref. 35, which states that the R-value should be 1.12, 0.96, 0.76, and 0.55 at 86%, 90%, 95%, and 100% oxygen saturation levels, respectively. Fig. 6.d) shows the measured SpO_2 against the expected SpO_2, confirming the

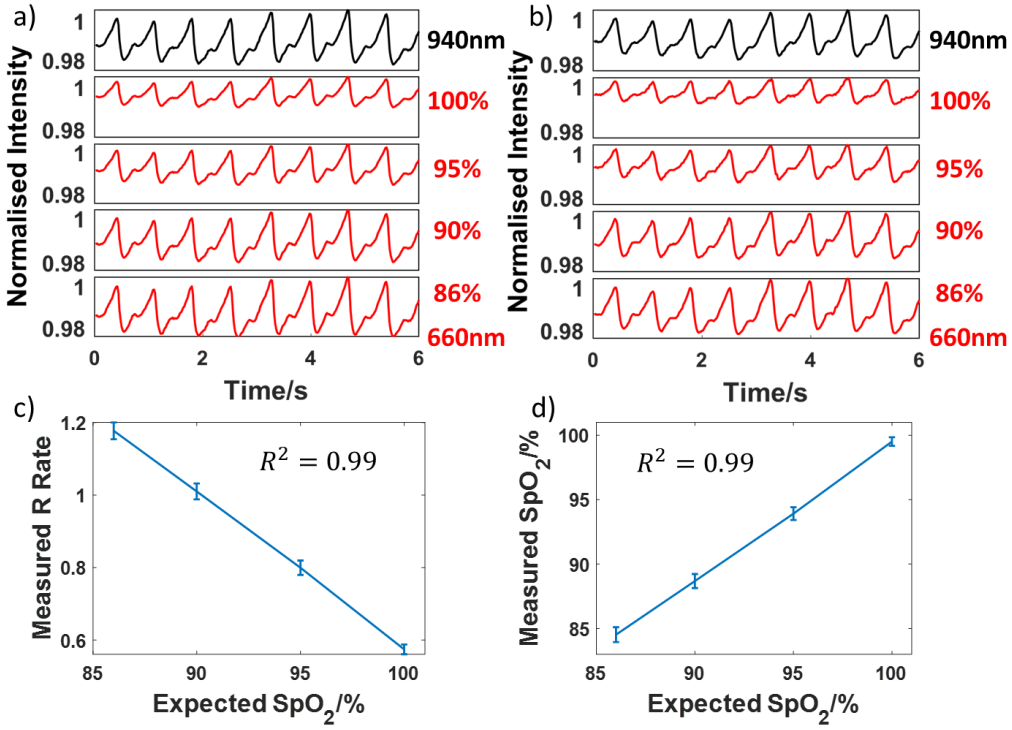

Fig. 6 a) Target signals at different oxygen saturation levels. b) Measurement results at different oxygen saturation levels. b) Expected SpO_2 vs. measured R value. c) Expected SpO_2 vs measured SpO_2.

accuracy of the dynamic phantom in simulating realistic SpO2 levels. These results validate the capability of the dynamic phantom to accurately mimic hemodynamics signals and its potential application in calibrating and validating pulse oximeters.

4 Discussion

Two case studies mentioned above demonstrate the ability of the dynamic phantom to generate PPG signals at different wavelengths and different oxygen saturation levels. For the characterization of the phantom, the functional range and contrast vary for different wavelengths due to the wavelength-dependent performance of the LCD. The operational wavelength range of

224 the dynamic phantom is thereby determined by the specifications of the LCD. In this setup, the
225 LCD provides broadband visual to near-infrared (400 – 2000 nm) operation with high open-state
226 transmittance optimized for wavelengths around 1100 nm. Consequently, the LCD response shows
227 larger contrast at 940 nm, 660 nm and 530 nm at 455 nm. It is also worth noting that only a small
228 fraction of the dynamic range of the functional voltage range has been used to generate the
229 modulation depth in the targeted PPG trace. The maximal modulation depth at 455 nm is 2% while
230 the perfusion index of the PPG signal from a health volunteer is around 1%[31]. The noise levels are
231 similar at all wavelengths when simulating a 1% perfusion index. The modulation frequency of
232 the phantom is limited by the operation rates of the LCD (1000 Hz) and NI DAQ (400 kHz). In
233 this study, a 50 Hz modulation frequency was used to match the sampling rate in Ref. 31. However,
234 with an upper modulation frequency limit of 1000 Hz, the device can simulate any feasible human
235 heart rate. This allows accurate reproduction of PPG pulse shape features, including the systolic
236 peak, diastolic peak and dicrotic notch. These capabilities highlight the phantom's potential to
237 simulate diverse PPG signal shapes for pulse shape analysis in cuffless blood pressure monitoring
238 applications[36]. In addition to the PPG signal, other dynamic variations in biological tissue, such as
239 hemodynamics, can be simulated by applying the corresponding modulation signals. Compared to
240 the phantom described in Ref. 24 which only characterizes spatial differentiation in attenuation for
241 optical topography, our phantom demonstrates the ability to gradually modulate attenuation with
242 a 153 μV step size voltage modulation and simulate realistic biological signals, making it a more
243 flexible tool for various biomedical applications.

244 When simulating the PPG signals, various noise signals can be added to simulate motion
245 artefacts introduced by physical movement during the measurement or low intensity signals due
246 to low blood perfusion. If the phantom is tested using a commercial pulse oximeter, the

transmission configuration should be used instead of the reflection configuration. Also, the illumination and phantom modulation must be synchronized since the typical pulse oximeter quickly switches between two wavelengths[32]. This can be achieved by having a sync input from the pulse oximeter to the phantom making it possible to dynamically change the phantom modulation to the corresponding wavelength of the pulse oximeter. The other approach is to have two individual light guides and LCDs, one for 660 nm modulation and the other for 940 nm modulation, separately.

In addition to generating dynamic signals, this setup could be used to characterize the spatial resolution of imaging or spectroscopy systems by varying the diameter of the light guide. Multiple light guides can be integrated to create specific patterns to mimic complex biological structures, such as vascular systems. There is no minimum space requirement between neighboring light guides. Compared to the thermochromic dynamic phantom described by Ref. 26, which has a target size of 4.5 mm, and requires 11.2 mm spacing between targets, and the phantom presented in Ref. 25, which only provides macroscopic absorption changes, our phantom shows better potential for simulating small and structured biological features with various target size. In future research, we intend to incorporate an additional thin-layer phantom with varying melanin concentrations to create a multilayer phantom. This multilayer phantom would mimic different skin colors, facilitating the characterization of skin color bias in pulse oximeters[37]. The phantom's low cost makes it widely applicable for both industrial and academic research. The estimated bill of material cost of our demonstration setup is approximately 5000 euros, though this may vary depending on the specifications of the LCD and NI DAQ. Currently, the dynamic phantom cannot simulate vascular compliance during the cardiac cycle due to its fixed geometric structure. To address this limitation, future enhancements could incorporate fiber bundles to mimic the vascular structure.

The geometry of the dynamic area of the phantom can be controlled by activating or deactivating specific fibers inside the fiber bundle.

5 Conclusion

In this study, we have reported the design, characterization, and potential applications of a dynamic phantom capable of generating dynamic biological signals. The absorption properties of the phantom can be controlled in real-time by modulating the LCD. The phantom was characterized at four wavelengths: 940 nm, 660 nm, 530 nm, and 455 nm. This dynamic phantom can simulate various biological signals by applying corresponding modulation signals. Clinically relevant case studies were conducted to prove the ability to generate PPG signals of different heart rates and oxygen saturation levels. This dynamic phantom shows the potential of calibrating and validating pulse oximeter, imaging, and spectroscopy systems.

Disclosures

Sanathana Konugolu Venkata Sekar and Stefan Andersson-Engels are shareholders of BioPixS Ltd with an interest in tissue optical phantoms. The other authors declare no conflicts of interest.

Code, Data, and Materials

The code used in this study is available on GitHub: https://github.com/Hui0930/Dynamic-phantom.git

Acknowledgements

The research work was supported by Science Foundation Ireland IPIC Biomedical theme (Grant No. SFI-12/RC/2276_P2, SFI/22/RP-2TF/10293), European Research Council (ERC) grant agreement No 101164780, European projects VASCOVID (101016087), and TinyBrains (101017113). We would like to acknowledge Konstantin Grygoryev for his assistance in proofreading this manuscript.

References

1. Q. Li et al., "Review of spectral imaging technology in biomedical engineering: achievements and challenges," *J. Biomed. Opt.* **18**(10), 100901 (2013) [doi:10.1117/1.JBO.18.10.100901].
2. Y. Hoshi and Y. Yamada, "Overview of diffuse optical tomography and its clinical applications," *J. Biomed. Opt.* **21**(9), 091312 (2016) [doi: 10.1117/1.JBO.21.9.091312].
3. L. Hacker et al., "Criteria for the design of tissue-mimicking phantoms for the standardization of biophotonic instrumentation," *Nat. Biomed. Eng.* **6**(5), 541-558 (2022) [doi:10.1038/s41551-022-00890-6].
4. W. S. Tummers et al., "Regulatory aspects of optical methods and exogenous targets for cancer detection," *Cancer Res.* **77**(9), 2197-2206 (2017) [doi:10.1158/0008-5472.CAN-16-3217].
5. C. D. Karakochuk et al., "Measurement and interpretation of hemoglobin concentration in clinical and field settings: a narrative review," *Ann. N. Y. Acad. Sci.* **1450**(1), 126-146 (2019) [doi: 10.1111/nyas.14003].
6. G. Lee, S. Choi, and K. Kim, "Association of hemoglobin concentration and its change with cardiovascular and all-cause mortality," *J. Am. Heart Assoc.* **7**(3), e007723 (2018) [doi: 10.1161/JAHA.117.007723].

7. S.-K. Park et al., "Noninvasive hemoglobin monitoring for maintaining hemoglobin concentration within the target range during major noncardiac surgery: A randomized controlled trial," *J. Clin. Anesth.* **93**, 111326 (2024) [doi: 10.1016/j.jclinane.2023.111326].
8. J. Kraitl et al., "Non-invasive measurement of blood components: Sensors for an in-vivo haemoglobin measurement," in *Advancement in Sensing Technology: New Developments and Practical Applications*, S. C. Mukhopadhyay and N. Krishnamurthy, eds., pp. 237-262, Springer, Berlin (2013). [https://doi.org/10.1007/978-3-642-32180-1_14].
9. J. A. Calbet et al., "Importance of hemoglobin concentration to exercise: acute manipulations," *Respir. Physiol. Neurobiol.* **151**(2-3), 132-140 (2006) [doi: 10.1016/j.resp.2006.01.014].
10. L. M. Neufeld et al., "Hemoglobin concentration and anemia diagnosis in venous and capillary blood: biological basis and policy implications," *Ann. N. Y. Acad. Sci.* **1450**(1), 172-189 (2019) [doi: 10.1111/nyas.14139].
11. S. Prahl, "Project: Optical Phantoms," *Oregon Medical Laser Center* (accessed December 29th 2023) [https://omlc.org/~prahl/projects/phantoms.html].
12. M. Z. Vardaki and N. Kourkoumelis, "Tissue phantoms for biomedical applications in Raman spectroscopy: a review," *Biomed. Eng. Comput. Biol.* **11**, 1179597220948100 (2020) [doi: 10.1177/1179597220948100].
13. L. Ntombela, B. Adeleye and N. Chetty, "Low-cost fabrication of optical tissue phantoms for use in biomedical imaging," *Heliyon* **6**(3), e03602 (2020) [doi: 10.1016/j.heliyon.2020.e03602].
14. B. W. Pogue and M. S. Patterson, "Review of tissue simulating phantoms for optical spectroscopy, imaging and dosimetry," *J. Biomed. Opt.* **11**(4), 041102 (2006) [doi: 10.1117/1.2335429].
15. S. K. V. Sekar et al., "Solid phantom recipe for diffuse optics in biophotonics applications: a step towards anatomically correct 3D tissue phantoms," *Biomed. Opt. Express* **10**(4), 2090-2100 (2019) [doi: 10.1364/BOE.10.002090]
16. A. B. Walter and E. D. Jansen, "Development of a platform for broadband, spectra-fitted, tissue optical phantoms," *J. Biomed. Opt.* **28**(2), 025001 (2023) [doi: 10.1117/1.JBO.28.2.025001].

17. S. Kleiser et al., "Comparison of tissue oximeters on a liquid phantom with adjustable optical properties," *J. Biomed. Opt.* **7**(8), 2973-2992 (2016) [doi: 10.1364/BOE.9.000086].
18. H. Isler et al., "Liquid blood phantoms to validate NIRS oximeters: yeast versus nitrogen for deoxygenation," in *Oxygen Transport to Tissue XL,* O. Thews, J. LaManna, and D. Harrison, eds., pp. 381-385, Springer, Cham (2018) [doi: 10.1007/978-3-319-91287-5_61].
19. X. Lv et al., "Design of a portable phantom device to simulate tissue oxygenation and blood perfusion," *Appl. Opt.* **57**(14), 3938-3946 (2018) [doi: 10.1364/AO.57.003938].
20. C. D. Kurth et al., "A dynamic phantom brain model for near-infrared spectroscopy," *Phys. Med. Biol.* **40**(12), 2079 (1995) [doi: 10.1088/0031-9155/40/12/006].
21. E. L. Hull, M. G. Nichols, and T. H. Foster, "Quantitative broadband near-infrared spectroscopy of tissue-simulating phantoms containing erythrocytes," *Phys. Med. Biol.* **43**(11), 3381 (1998) [doi: 10.1088/0031-9155/43/11/014].
22. T. O. McBride et al., "Spectroscopic Diffuse Optical Tomography for the quantitative assessment of hemoglobin concentration and oxygen saturation in breast tissue," *Appl. Opt.* **38**(25), 5480 (1999) [doi:10.1364/ao.38.005480].
23. R. Zhang et al., "Čerenkov radiation emission and excited luminescence (CREL) sensitivity during external beam radiation therapy: Monte Carlo and Tissue Oxygenation Phantom Studies," *Biomed. Opt. Express* **3**(10), 2381 (2012) [doi:10.1364/boe.3.002381].
24. P.H. Koh, C.E. Elwell, and D.T. Delpy, "Development of a Dynamic Test Phantom for Optical Topography," in *Oxygen Transport to Tissue XXX*, P. Liss, P. Hansell, D.F. Bruley, and D.K. Harrison, eds., pp. 141-146, Springer, Boston, MA (2009) [doi: 10.1007/978-0-387-85998-9_22].
25. T. Funane et al., "Dynamic phantom with two stage-driven absorbers for mimicking hemoglobin changes in superficial and deep tissues," *J. Biomed. Opt.* **17**(4), 047001-047001 (2012) [doi: 10.1117/1.JBO.17.4.047001].

26. J. C. Hebden et al., “An electrically-activated dynamic tissue-equivalent phantom for assessment of Diffuse Optical Imaging Systems,” *Phys. Med. Biol.* 53(2), 329–337 (2007) [doi:10.1088/0031-9155/53/2/002].
27. H. Ma et al., “Light-guided dynamic phantom to mimic microvascular for biomedical applications,” Optica Biophotonics Congress: Biomedical Optics 2024 (Translational, Microscopy, OCT, OTS, BRAIN) (2024) [doi:10.1364/ots.2024.ow3d.2].
28. S. Konugolu Venkata Sekar et al., "Diffuse optical characterization of collagen absorption from 500 to 1700 nm," *J. Biomed. Opt.* **22**(1), 015006 (2017) [doi: 10.1117/1.JBO.22.1.015006].
29. S. Konugolu Venkata Sekar et al., "Broadband time domain diffuse optical reflectance spectroscopy: a review of systems, methods, and applications," *Appl. Sci.* **9**(24), 5465 (2019) [doi: 10.3390/app9245465].
30. D. Makowski et al., "NeuroKit2: A Python toolbox for neurophysiological signal processing," *Behav. Res. Methods* **53**(4),1689-1696 (2021) [doi:10.3758/s13428-020-01516-y].
31. A. I. Siam et al., “Real-World PPG dataset,” Mendeley Data, V3 (2022) (accessed January 31, 2024) [doi: 10.17632/yynb8t9x3d.3].
32. E. D. Chan, M. M. Chan and M. M. Chan, "Pulse oximetry: understanding its basic principles facilitates appreciation of its limitations," *Respir. Med.* **107**(6), 789-799 (2013) [doi: 10.1016/j.rmed.2013.02.004].
33. S. Kästle et al., "A new family of sensors for pulse oximetry," *Hewlett Packard J.* **48**, 39-47 (1997).
34. N. Stubán and N. Masatsugu, "Non-invasive calibration method for pulse oximeters," *Period. Polytech. Electr. Eng. (Archives)* **52**(1-2), 91-94 (2008) [doi: 10.3311/pp.ee.2008-1-2.11].
35. S. Prahl, "Summary of hemoglobin spectra," Oregon Medical Laser Center, https://omlc.org/spectra/hemoglobin/summary.html (accessed January 31, 2024).
36. 1.J.-R. Hu et al., “Validating cuffless continuous blood pressure monitoring devices,” *Cardiovasc. Digit. Health J.* **4**(1), 9–20 (2023) [doi:10.1016/j.cvdhj.2023.01.001].

386 37. R. Al-Halawani et al., "A review of the effect of skin pigmentation on pulse oximeter accuracy,"
387 *Physiol. Meas.* **44**(5) (2023) [doi:10.1088/1361-6579/acd51a].

Paper III

Raman Spectroscopy based framework for In-Vivo Assessment of Bone Composition

H. Ma, P. Lanka, S. Kothuri, B. Jayet, A. Mahadevan Jansen, S. Andersson-Engels, S. Konugolu Venkata Sekar and R. Gautam.

Journal of Physics: Photonics **8(1)**, 015065 (2026).

IOP Publishing *Journal* **vv** (yyyy) aaaaaa Author *et al*

Journal Name

Crossmark

RECEIVED
dd Month yyyy

REVISED
dd Month yyyy

ARTICLE TYPE

Raman Spectroscopy based framework for In-vivo Assessment of Bone Composition

Hui Ma[1,2,*], Pranav Lanka[1], Suraj Kumar Kothuri[1,2], Baptiste Jayet[1], Anita Mahadevan Jansen[3], Stefan Andersson-Engels[1,4,5], Sanathana Konugolu Venkata Sekar[1,4,5], and Rekha Gautam[1,*]

[1]Biophotonics@Tyndall, Cork, Ireland
[2]Engineering Science, University College Cork, Cork, Ireland
[3]Vanderbilt Biophotonics Center, Vanderbilt University, Nashville, TN, USA
[4]School of Physics, University College Cork, Cork, Ireland
[5]BioPixS Ltd, Cork, Ireland
*Author to whom any correspondence should be addressed.

E-mail: hui.ma@tyndall.ie and rekha.gautam@tyndall.ie

Keywords: Raman spectroscopy, bone, high wavenumber, enhancement to noise ratio

Abstract

Bone-related disorders, including osteoporosis, lead to decreased bone density and altered microarchitecture, significantly increasing the risk of fragility fracture. There is an urgent need for innovative early detection methods, as conventional techniques like dual-energy X-ray absorptiometry offer limited insights into bone quality, often overlooking critical microstructural changes. In this study, we present a novel dual-wavelength inverse spatially offset Raman spectroscopy (DWiSORS) system specifically designed to enhance the assessment of transcutaneous bone signals. This innovative approach utilizes ring illumination to deliver adequate power while minimizing the fluorescence background, and dual-wavelength excitation to capture a broader molecular profile (spectral range). We introduce a novel metric, enhancement-to-noise ratio (ENR),which provides a quantitative and robust strategy to identify the optimal offset for accurate assessment at specified depths, addressing a significant limitation in existing in-vivo SORS methodologies. The metric efficacy was validated through in-vivo measurements on ten healthy volunteers, where the ENR was analyzed against increasing source-detector offsets, with tissue thickness determined by ultrasound imaging. Notably, optimal signal-to-noise ratio for bone signals were achieved at offsets of 7 or 9 mm, even beneath 10-14 mm of overlaying tissue, reinforcing increasing the offset beyond this threshold does not necessarily enhance bone signals detection. In-vivo measurements demonstrate the technical feasibility and robustness of the proposed DWiSORS framework for depth-resolved bone Raman measurements. This study indicates the potential of Raman spectroscopy to complement conventional imaging techniques and support future approaches for non-invasive assessment and longitudinal monitoring of bone-related disorders.

1 Introduction

Bone-related conditions such as osteoporosis are characterized by reduced bone mineral density (BMD) and changes in the matrix and microarchitecture, increasing the likelihood of fragility fractures. This condition affects nearly 32 million people in Europe, resulting in 4.3 million fractures annually and an economic burden of € 57 billion[1, 2]. The standard clinical method for diagnosing osteoporosis is dual-energy X-ray absorptiometry (DEXA), which assesses BMD[3]. However, relying solely on BMD does not fully reflect bone strength, leading to low accuracy in predicting fracture risk, particularly in early postmenopausal women and patients with type 2 diabetes[4, 5]. Alternative methods like quantitative-computed tomography (QCT) and magnetic resonance imaging (MRI) provide insights into bone microstructure but are limited by high radiation doses, costs, and accessibility issues[6, 7]. These methods are also unsuitable for certain implants and for monitoring in children and pregnant women[8]. While quantitative ultrasound (QUS) is a safer option, it faces challenges related to precision and specificity[9]. Notably, studies

show that 82% of women with fragility fracture had normal BMD per DEXA, missing the crucial window for timely intervention[10]. Consequently, while DEXA remains the standard for osteoporosis diagnosis, its sensitivity for predicting fractures in individuals is recognized as limited, with meta-analyses reporting a wide range (35% to 75%) depending on the population and fracture site studied[11, 12, 13]. Given the high prevalence and economic impact of fragility fractures, there is a critical need for improved diagnostic approaches that can provide a comprehensive biochemical, structural, and functional assessment of bone for the early detection of bone degeneration.

Optical techniques, such as Raman spectroscopy, are capable of providing biochemical profile by simultaneous assessment of various components within bone, covering matrix elements and mineral[14, 15]. Currently, Raman research in bone disorder diagnosis primarily focuses on the fingerprint (FP) region (400–1800 cm^{-1}) due to its rich biochemical information on proteins, lipids, nucleic acids, and minerals[16, 17]. However, the high wavenumber (HW) region (2800–3800 cm^{-1}) provides valuable information on biochemicals such as proteins, lipids, and especially water content[18, 19, 20]. This is particularly critical for probing deep tissue, as the HW region offers a spectral window less congested by overlapping peaks, enabling clearer isolation of key biomarkers from subsurface layers. The integration of FP and HW spectra has shown potential in improving early disease diagnosis in-vivo and will enable new insights into how age, gender, disease conditions, and mechanical damage influence bone strength[20, 21, 15]. There are several ways to acquire both FP and HW spectra with single wavelength near infrared excitation, generally used for biological system. One is using low groove density grating, which results in low spectral resolution[21], the other one is changing the setting (e.g. angle) of the grating when measuring different spectrum regions. For in-vivo clinical applications, this is impractical as it necessitates disengaging the probe from the sample to perform a wavelength recalibration after each move, increasing measurement time and complexity. An expensive and complex dual transmission grating has also been explored to acquire the FP and stretch regions onto different vertical segments of the detector[22]. A dual-wavelength unit excitation is a simpler alternative solution to measure FP and HW regions sequentially without compromising spectral resolution[23]. However, existing dual-wavelength systems predominantly sample superficial tissue volumes, which limits their in-vivo applicability and leaves a significant unmet need for reliable measurements of deep tissues such as bone, where signals are overwhelmed by contributions from superficial layers. Inverse spatially offset Raman spectroscopy (iSORS) addresses this by introducing a spatial offset between excitation and collection, thereby enhancing sensitivity to subsurface signals while reducing surface power density [24, 25]. A central challenge in iSORS is that while a larger offset probes deeper, the signal-to-noise ratio (SNR) concurrently decreases [26]. Consequently, identifying the ideal offset that balances penetration depth and SNR is critical for accurate depth-resolved assessment.

To address this, we developed a dual-wavelength iSORS (DWiSORS) system combined with a novel, quantitative enhancement-to-noise ratio (ENR) metric. This work presents the first in-vivo demonstration of a unified framework that: (i) objectively determines the optimal spatial offset for deep-layer Raman measurements; (ii) simultaneously acquires both FP and HW spectra at high resolution without hardware reconfiguration, enabling co-registered assessment of mineral, matrix, and hydration biomarkers; and (iii) validates the robustness of the ENR metric against noise, spectral processing parameters, and variability in tissue optical properties. Our results highlight the potential of Raman spectroscopy as a non-invasive method for evaluating bone quality by effectively probing locations with tissue thickness below 5 to 14 mm, as an increase in offset beyond 10 mm does not necessarily enhance the bone signals.

2 Method and material

2.1 Chemicals

Gelatine (G2500, Sigma-Aldrich USA), Intralipid 20% w/v (Fresenius Kabi, Ltd), India ink (Higgins, 44201 Chartpak Inc., USA), Hydroxyapatite nano powder (677418, Sigma-Aldrich, USA), Hydroxyapatite granules (912204, Sigma-Aldrich, USA) and Ammonium chloride (213330, Sigma-Aldrich, USA) were used. All solutions were prepared using deionised water.

2.2 Phantom fabrication

Bottom layer bone phantom was prepared by mixing 25 g of hydroxyapatite (HA) granules and 25 g of ammonium chloride (NH_4Cl), grinded by a mortar and pestle. The mixture was then placed in a Petri dish and covered with a CaF_2 window (CAFP50-1R, Crystran, UK). Silicone-based B2 phantom ($\mu_a = 0.1\,cm^{-1}$ and $\mu_s' = 10\,cm^{-1}$) from MEDPHOT (BioPixS, Ireland)[27] matrix was used as top layer tissue mimicking phantom. This phantom was chosen because its optical properties closely match those of the tissue described in [28]. Hydration phantoms of water

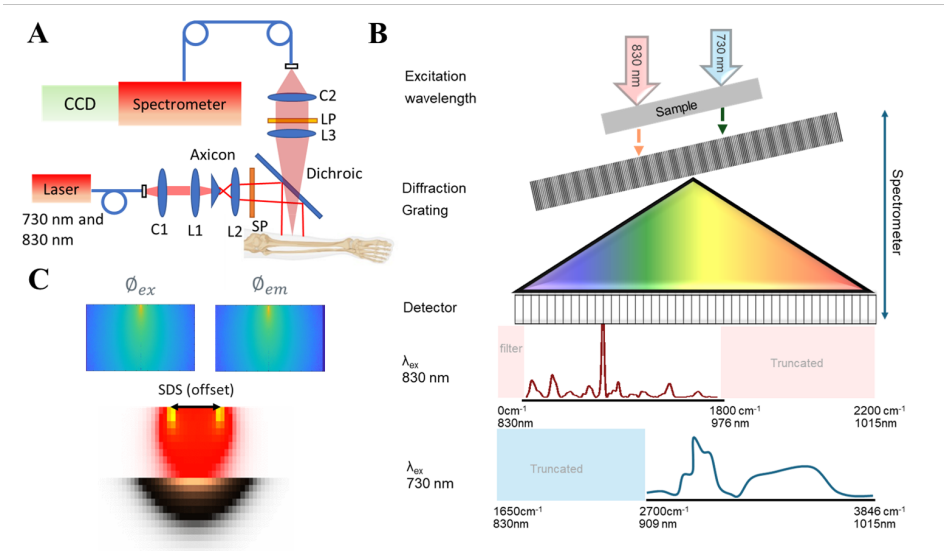

Figure 1. (A) Schematic layout of the DWiSORS system. SP: 830 nm short pass filter, LP: 830 nm long pass filter, L: lens, C: collimator. (B) The mapping of fingerprint and high wavenumber regions on the detector corresponding to each excitation wavelength. (C) Layout of adjoint Monte Carlo simulation.

concentrations at 82% and 89% (w/v) were made using gelatine, intralipid, and India ink. For gelatine based bone phantom, 4% and 7% (w/w) hydroxyapatite nano power were dispersed in the 0.1 M HCl solution and vortexed and added to the bulk gelatine matrix described in [29].

2.3 Raman spectroscopy system design

Figure 1A illustrates the dual-wavelength inverse SORS system. The dual-wavelength laser source (model #0811A100-B Fat Boy, Innovative Photonics Solutions, USA) provides 730 nm and 830 nm laser excitations. The light from the laser diode was coupled into a fibre (M43L02, Thorlabs, USA) and collimated by a collimator C1 (CFC-2X-A, Thorlabs, USA). Achromatic doublets L1 (AC254-030-A, Thorlabs, USA) and L2 (AC254-040-B-ML, Thorlabs, USA) were used to adjust the focus of the laser on the sample plane.

The ring illumination was generated using an axicon (AX1220-B, Thorlabs, USA), and the ring size could be adjusted by changing the position of the axicon [30]. The excitation light was cleaned with a short-pass filter SP (FF01-842/SP-25, Semrock, USA). The light was then reflected by a dichroic mirror (DI02-R830-25X36, Semrock, USA), and the ring illumination pattern was generated on the sample plane (Figure 2A).

The backscattered light was collected from the centre of the ring by L3 (AC254-100-AB-ML, Thorlabs, USA), then filtered by a long-pass filter LP (BLP01-830R-25, Semrock, USA), and coupled into a (bundle-to-line) fibre (BFL200LS02, Thorlabs, USA) using a coupler C3 (F810SMA-780, Thorlabs, USA). The long pass filter has a high transmission efficiency ($> 95\%$) for wavelengths on and above 847 nm, corresponds to a Raman shift of roughly 250 cm^{-1} at $\lambda_{ex} = 830$ nm allowing the transmission of whole fingerprint region and $\sim 1900\,\mathrm{cm}^{-1}$ at $\lambda_{ex} = 730$ nm. The signal was detected by a Raman spectrometer (Acton LS785, f/2, Teledyne Princeton Instruments, USA) equipped with a deep-depletion CCD camera (Blaze: 400HR, Teledyne Princeton Instruments, USA) [31].

The spectrometer, equipped with a fixed grating, has a detection range of 858 - 1015 nm, which corresponds to 394 - 2200 cm^{-1} relative to 830 nm excitation, and 2045 - 3850 cm^{-1} relative to 730 nm excitation. Figure 1B shows the mapping of FP and HW regions on the detector corresponding to each excitation wavelength.

2.4 Raman measurement and data processing

The spectral axis of the system was calibrated with a NeAr lamp (IntelliCal, Teledyne Princeton Instruments) and subsequently verified using a silicon reference featuring a line at 520.5 cm^{-1}

before obtaining the sample spectra. Raman spectra were acquired using a dual-wavelength system with 830 nm and 730 nm excitation at 100 mW, with integration times of 8 s and 4 s, respectively. All room lights were turned off during the measurements. (i) Different thicknesses of the B2 phantom were overlaid on top of the bone (HA + NH_4Cl) phantoms. The relation between the penetration depth and the ring size was characterised using 3 mm, 5 mm, 7 mm, 9 mm, and 11 mm radius ring sizes. (ii) To evaluate the sensitivity of the system towards changes in bone quality, Raman data was measured from the (4% and 7%) HA and (82% and 89%) hydration phantoms with and without 5 mm pork tissue using selected (ideal) offset. Five spectra were recorded for each configuration.

Fluorescence background in the spectra was removed using the Asymmetric Least Squares method with lambda = 1000000 and p = 0.00001 at 730 nm, and lambda = 5000 and p = 0.001 at 830 nm [29]. Next we would like to estimate the source-detector distance that would perform best to measure bone signals. This was done by comparing the relative signal of the bone and superficilal layer and compare that to the signal variation due to noise in the signal. First we defined the signal variation as coefficient of variation 'CV':

$$CV = \frac{std}{signal} \tag{1}$$

where *signal* is the mean value of five measurements at each configuration and *std* is the standard deviation. The CV provides a standardized measure of precision that is independent of absolute signal intensity and allows for robust comparison across measurements with widely varying photon counts. The metric enhancement-to-noise ratio (ENR) to define the ideal offset thus is:

$$ENR = \frac{I_{bottom}}{I_{top} \cdot CV_{bottom}} \tag{2}$$

where I_{bottom} is the integrated intensity under the peak of the bottom layer (e.g. 955–969 cm^{-1}, 3011–3101 cm^{-1}), I_{top} is the integrated intensity under the peak of the top layer (e.g. 684–694 cm^{-1}, 2960–2997 cm^{-1}), and CV_{bottom} is the CV at the peak location of the bottom layer. The selected peaks are spectrally distinct, with a minimum overlap between the top and bottom contributions. An ideal offset was selected based on the experimental data by plotting ENR against spatial offsets.

For the in-vivo measurement, healthy participants were enrolled in a study approved by the Clinical Research Ethics Committee (CREC) of University College Cork (CREC ref.: ECM 4 (s) 20062023 & ECM 5 (5) 20/06/2023 & ECM 3 (aaa) 15/05/2025). Written informed consent was obtained from human participants and study was performed in accordance with the Guidelines of Helsinki. The performance of the Raman system was evaluated with ten healthy participants, with Raman spectra acquired from the tibia (8 cm below the knee head) at varying offsets between 0 and 11 mm. The integration time was set to 10 s at 730 nm and 30 s at 830 nm. The laser power was adjusted for each ring size (i.e., offset) to remain below the maximum permissible exposure (MPE) (see Supplementary Table S1) according to the American national standard for safe use of lasers (ANSI Z136.1)[32]. The measurement site was shaved and wiped with Kimtech tissue. A minimum of five measurements were collected for each offset. The thickness of the overlying tissue at the tibia was measured using ultrasound (US) with a UHF22x transducer (10–22 MHz bandwidth, FUJIFILM VisualSonics), operated at the lowest possible power ($< 190, mW/cm^2$ peak power)[33]. Ultrasonic gel (Aquasonic, Parker Laboratories, USA) was applied to the tibia region, and the US probe was gently placed to acquire images while avoiding excessive pressure. At least six ultrasound images were acquired from each participant, and the median thickness value from the four best images was used as tissue thickness on the tibia bone. The optical and US probe heads were cleaned with isopropyl alcohol in between measurements.

2.5 Optical properties measurement

Optical properties of all the phantoms were measured using home built time doman diffuse optical set-up as described by S. Kothuri et al [34]. Briefly, the powder phantoms were filled into a hollow tube of 1-inch diameter, with the ends connected to two FC/PC (Thorlabs) connectors to house the source and detector fibers, as shown in the Figure S1. Time-of-flight measurements were then carried out in transmission mode.

2.6 Monte Carlo Simulation

Numerical simulations of light propagation in a two-layer model were performed using Monte Carlo eXtreme V2024.2[35]. The model configuration was simplified to a ring source with a ring width

(outer radius – inner radius) of 1 mm for excitation and a 1 mm diameter disk detector for collection concentric to the ring. The bottom layer was modelled as a cube with a side length of 10 cm, with a voxel size of 0.5 mm used as the sample resolution. A top layer with variable thickness, ranging from 1 to 10 mm in 1 mm increments, was added above the bottom layer. The optical properties used in the simulations for different excitation and emission wavelengths are based on experimental phantom data as summarized in Table 1. The simulation process is illustrated in Figure 1C. For each simulation, 10^8 photon packets were launched. For a given source–detector separation, the net diffuse reflectance was estimated using the adjoint Monte Carlo (aMC) method, by taking the product of the fluence maps generated with the source at its true position and at the detector position (treated as a virtual source) [36, 37]. The fractional contribution of each layer to this effective Jacobian was then used as a proxy for the relative Raman signal originating from that layer. This is based on the assumption that the Raman-active material is uniformly distributed within each layer. For high-performance Raman CCDs, the noise is assumed to be dominated by photon shot noise, which is proportional to the square root of the total photon count. The total simulated photon signal reaching the detector is then adjusted to account for Raman noise due to fluorescence background photons by borrowing from experimental data, using the following relation:

$$N_{\text{lay,sim,total}} = N_{\text{lay,sim,Raman}} \cdot \frac{N_{\text{lay,exp,Raman\_peak}} + N_{\text{lay,exp,Raman\_bkg}}}{N_{\text{lay,exp,Raman\_peak}}}. \quad (3)$$

where $N_{\text{lay,sim,Raman}}$ is the value obtained from the aMC method described above, while $N_{\text{lay,exp,Raman\_peak}}$ and $N_{\text{lay,exp,Raman\_bkg}}$ are the experimentally measured Raman peak and background counts for that layer. Since experimental data were only available up to a 12.5 mm offset, the Raman background fraction at larger offsets was estimated by extrapolating the 0–12.5 mm data. This approach allowed us to simulate the ENR beyond the range measured experimentally. To evaluate the robustness of the ENR trends to assumptions in experiment noise extrapolation, a sensitivity analysis was performed by varying $N_{\text{lay,exp,Raman\_peak}}$ by ±20%.

Table 1. Optical properties of top and bottom layers.

Wavelength (corresponding wavenumber)	**Bottom layer (HA + NH_4Cl)**				**Top layer (silicone-based)**			
	μ_a **(cm^{-1})**	μ_s **(cm^{-1})**	g	n	μ_a **(cm^{-1})**	μ_s **(cm^{-1})**	g	n
830 nm	0.0472	96.1	0.9	1.41	0.102	9.07	0.9	1.34
730 nm	0.0500	99.2	0.9	1.41	0.113	10.7	0.9	1.34
Bottom peak at 830 nm (960 cm^{-1})	0.0425	91.1	0.9	1.41	0.165	7.47	0.9	1.34
Top peak at 830 nm (688 cm^{-1})	0.0448	92.9	0.9	1.41	0.114	8.21	0.9	1.34
Bottom peak at 730 nm (3050 cm^{-1})	0.0638	92.1	0.9	1.41	0.105	6.96	0.9	1.34
Top peak at 730 nm (2971 cm^{-1})	0.0609	92.0	0.9	1.41	0.104	7.11	0.9	1.34

3 Results and discussion

In this study a dual-wavelength ring illumination system was developed to acquire transcutaneous Raman spectrum of bone in-vivo for the first time. The system was optimized using bone and tissue mimicking phantoms. The raw Raman spectra of the bone (HA + NH_4Cl) phantoms concealed beneath 5 mm thick tissue phantoms at various source-detector distances are presented in the Supplementary Figure S2. The composition of the bottom layer (HA + NH_4Cl) mixture was carefully formulated to optimize signal acquisition from both (FP and HW) regions and keeping the bottom layer 960 cm^{-1} band strength equivalent to weaker matrix Raman signal in bone. We selected 5 mm thickness for the overlying tissue phantom to illustrate how the proposed ENR framework behaves for a typical in-vivo scenario (e.g., metacarpal and tibial midshaft regions), as indicated by the ultrasound measurements listed in Table S2. As the spatial offset increases, the overall signal intensity decreases and to clearly visualize the percentage contribution from the underlying bone phantoms, all spectra have been normalized to the integrated intensity of the characteristic FP band region (684–694 cm^{-1}) and HW band region (2960 – 2997 cm^{-1}) as illustrated in Figures 2B and D, respectively. Enlarged views highlighting the peaks corresponding to the bottom layer are shown in Figures 2C (961 cm^{-1}) and E (3050 cm^{-1}). As the offset increased, the signal contribution from the top layer decreased more rapidly, while the signals from the bottom layer decreased slowly and exhibited a trend toward levelling off (Figure 2F). This trend is consistent with previously published SORS studies, and primarily occurs because the average photon pathlength increases with offset, leading to greater exponential losses from absorption and scattering. The key outcome is that the slower-decaying bottom-layer signal becomes progressively dominant over the rapidly decaying surface signal, thereby providing the enhanced depth contrast that is the basis of SORS techniques[26, 38, 39].

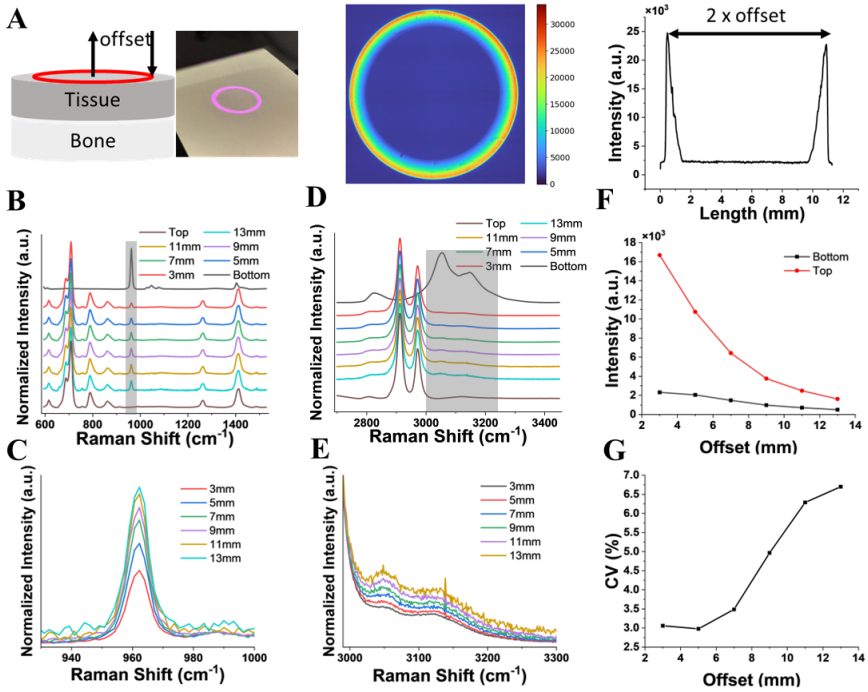

Figure 2. Raman spectra recorded from the bone phantom (HA + NH_4Cl) hidden beneath a 5 mm tissue phantom at varying spatial offsets. (A) Experimental configuration illustrating the iSORS geometry and measured excitation beam profile at the sample surface; the ring illumination exhibited an ellipticity of 0.99, indicating near-circular symmetry. (B) Fingerprint Raman spectra normalized to the integrated intensity of the top-layer Raman peak in the 684–694 cm^{-1} range, setting this peak to unity across all spatial offsets. (C) Enlarged view of the highlighted region within 940–1000 cm^{-1}. (D) High-wavenumber Raman spectra normalized to the integrated intensity of the top-layer Raman peak in the $2960 - 2997$ cm^{-1} range, setting this peak to unity across all spatial offsets. (E) Enlarged view of the highlighted region within 3000-3300 cm^{-1}. (F) Variation of Raman intensity from the top and bottom layers with increasing spatial offset. (G) Coefficient of variation (CV) of the bottom-layer signal as a function of spatial offset.

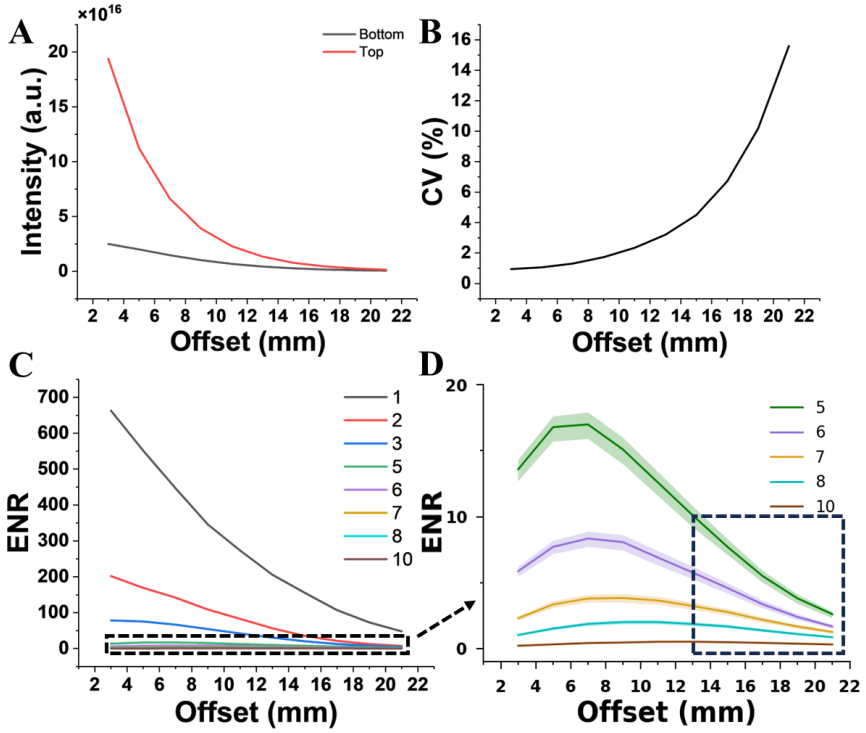

Figure 3. Two layer Monte Carlo simulation results: (A) Raman intensity from the top and bottom layers with a 5 mm top layer. (B) Coefficient of variation (CV) as a function of source-detector offset with a 5 mm top layer. (C–D) Enhancement-to-noise ratio (ENR) as a function source–detector offset for different top layer thicknesses. (C) shows all cases, where the strong signals for top layer of 1-3 mm thicknesses dominate the plot. To better visualise the variation at larger thicknesses, (D) presents enlarged view of the 5–10 mm to layer thicknesses with 20% noise variation, the box indicates the region where noise was extrapolated using experimental data.

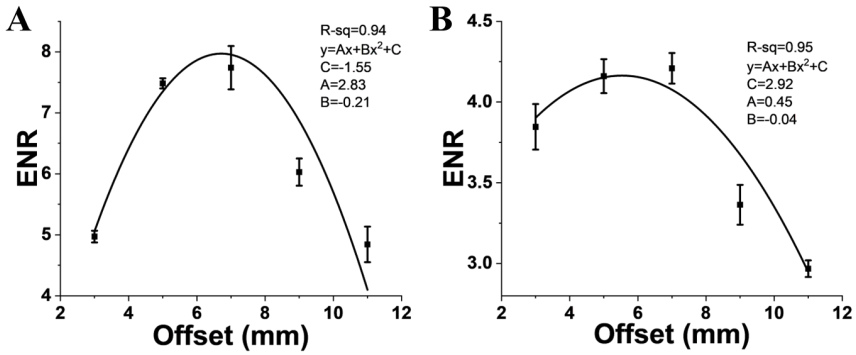

Figure 4. Measurement of Enhancement-to-noise (ENR) ratio as a function of offset for bone phantoms covered with 5 mm top tissue layer with error bar from 5 measurements in (A) fingerprint region, integrated range $955 - 969$ cm^{-1} band, (B) high wavenumber region, integrated range $3011 - 3103$ cm^{-1} band.

Although the bottom-to-top layer ratio increased with offset, confirming the relative enhancement of bottom layer signals, the SNR of the bottom layer at a 12.5 mm offset was poor (sea-green curve in Figure 2C). This reduction in SNR is quantified by the increase in CV values (Figure 2G). However, the maximum offset analyzed is limited by the dimension of the optical components, 25.4 mm (one inch) lenses. Thus, to identify ideal offset metric a wide range of offsets were analyzed using Monte Carlo simulations. Simulations were performed to analyse photon migration at offsets between 0 to 20 mm with varying top layer thicknesses (1-10 mm) in a two layers model. Figure 3 depicts the trends of top and bottom layer signals obtained through simulations for a 5 mm top layer thickness, consistent with experimental data (Figure 2F). Raman intensities from both layers decreased as the offset increased, with the top layer's intensity declining faster, thereby providing better contrast (enhancement) for visualizing the bottom layer (Figure 3A). To account for both the enhancement of bottom layer signals and the increase in noise level with increase in spatial offset (Figure 3B), an ideal offset metric was defined using simulated data: ENR = enhancement/CV (Figure 3C and D). For fixed 5 mm thick top layer, the ENR increased steadily at shorter offsets, indicating that signal enhancement dominated the noise as the offset approached the optimal range. However, beyond this optimal point, ENR decreased due to signal attenuation leading to increased CV. Thus, this metric provides a parabolic peak as the ideal offset. Figure 3C and D shows how these parabolas change with different top layer thicknesses (1 to 10 mm) when the metric is plotted against spatial offset. As expected, smaller offsets, such as a 3 mm ring size, are optimal for detecting signals through a top layer thickness of 3 to 4 mm. To penetrate a top layer thickness of 5 mm, 6 mm, 7 mm, and 8 mm, the optimal offset identified to be approximately 6 mm, 7 mm, 8 mm, and 10 mm, respectively. With greater top-layer thickness, a larger source-detector offset is necessary to retrieve information from the bottom layer, resulting in an increase in the ideal offset value. However, in our set of simulation cases, increasing the offset beyond 12 mm does not yield additional signals from the bottom layer in the detection channel, while the CV values showed steep rise (Figure 3B). To assess the robustness of the identified optimal offset to uncertainties in noise modeling, we performed a sensitivity analysis by varying the experimentally derived noise level as described in Section 2.6. This analysis confirmed the robustness of the optimal offset, as its location remained unchanged despite variations in noise that altered the absolute ENR magnitude by less than ±7%. The resulting ENR uncertainty bands are shown as shaded regions in Figure 3D.

The contrast between the bottom/top layer and the SNR have been used independently for the identification of optimum offset previously. Commonly used metric in SORS experiments to determine ideal offset is the ratio of Raman band intensity from the bottom layer to that from the top layer[39]. Other studies defined SORS ratio as the intensity from the bottom layer at a specific offset divided by the corresponding ratio at zero offset[40]. As noise contribution is not accounted here, these metrics may lead to the misconception that increasing the offset allows for signal retrieval from any depth and that the SORS ratio turns out to be independent of the top layer thickness. An SNR-optimal offset, that maximizes the bottom layer's SNR, has also been suggested previously that also depends on Raman (cross-section) peak strength[26]. This study used the ordinary least squares fit coefficient which requires pure spectra from bottom and top layer as the basis spectra for the fit that may not be applicable for in-vivo measurements.

The ENR metric defined here is balancing both bottom layer's signal enhancement and its quality (i.e. noise levels) and shows a significant match (alignment) to experimental findings for both FP and HW regions (Figure 4A, B). The experimental results demonstrate a trend consistent with the simulation data, showing that ENR increased with offset until reaching a peak value, after which it declined with further increases in offset. The optimal offset for acquiring subsurface layer data through a 5 mm top layer was determined to be approximately 6 mm for both the FP at 961 cm^{-1} (Figure 4A) and HW at 3050 cm^{-1} (Figure 4B) Raman bands. Our system demonstrates improved depth sensitivity with adequate SNR compared to previous SORS systems. To evaluate the robustness of the ENR metric, additional analyses were performed by varying the Raman peak integration window by ±5 cm^{-1} for bottom layer peak and by applying alternative normalization to total area under the curve. These variations resulted in minor changes to absolute ENR values but did not alter the overall ENR trends or the optimal spatial offset, which varied by less than 10% change in integration window as well as normalization method (Figure S3).

The optimal spatial offset determined for probing through a 5 mm thick top layer was utilized to assess the sensitivity of the DWiSORS system to variations in mineral and water content, with validation conducted using gelatin based bone phantoms. The spectra were recorded with 830 nm and 730 nm excitation wavelengths to acquire FP and HW regions respectively, covering the comprehensive biochemical profile of bone. Raman spectra were obtained using a 6 mm ring

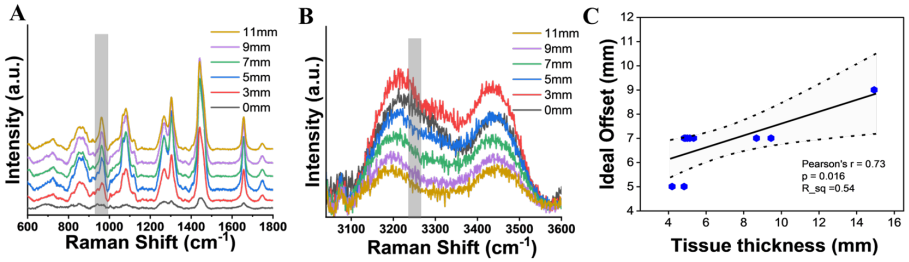

Figure 5. Raman spectra recorded from tibia of healthy participants (A) fingerprint region, (B) high wavenumber region. (C) Correlation between the tissue thickness measured by ultrasound and the ideal offset for Raman, the solid line represents the linear regression fit with 95% confidence interval and significance of the non-zero slope ($p < 0.05$) was confirmed using ANOVA.

.

illumination (offset) from hydroxyapatite (HA) and hydration phantoms concealed beneath a 5 mm thick pork-tissue layer to simulate in-vivo conditions. Raman spectra for phantoms containing 4% and 7% HA showed differences in Raman band intensity at 961 cm^{-1}, reflecting the increased HA concentration (Supplementary Figure S4A). The system is able to detect a 3% difference in HA concentration within the bone phantoms, suggesting that Raman-based mineral measurements could be instrumental in the early detection of bone deterioration, particularly since the gold standard DEXA method typically identifies changes in BMD only after a loss of 15-30%[41]. Additionally, Raman spectra for water phantoms with varying hydration levels indicated that the intensity of the broad O-H band from water decreased as the hydration concentration dropped from 89% to 82%[29] (Supplementary Figure S4B). Previous in-vivo studies on bone have primarily focused on the FP Raman region, often overlooking the hydration region due to instrument limitations such as detector size or static grating. However, Raman microscopy studies have demonstrated significant correlation between hydration and bone strength/quality underscoring the capability of Raman spectroscopy to differentiate between bound and unbound water[20]. The DWiSORS measurements on these phantoms demonstrate that we can acquire hydration signals with sensitivity of differentiation of 7% changes in hydration at 5 mm depth. This provides valuable insights into the composition and hydration state of the bone phantoms.

To further validate the system's performance, in-vivo Raman spectra were recorded from 10 healthy participants (Figure 5). Our modular DWiSORS system allows for the collection of SORS signals with multiple spatial offsets (0-11 mm) from the point of collection, maintaining the same illumination power density (0.23 Wcm^{-2} for 730nm and 0.36 Wcm^{-2} for 830nm) well within the MPE. Ring illumination distributes laser power over a larger area, allowing for higher overall power, which also helps to reduce the fluorescence background that predominantly originates from skin melanin. Any superimposed background e.g. fluorescence introduce noise and limits detector accumulation time [42]. The customized Raman probe employed, equipped with a hollow cylindrical spacer on the head, was gently pressed against the skin over the tibia mid-shaft region (Figure 1A). Overall, the measurement was completed in 45 minutes, including the FP and HW regions at six offsets for each participant. Representative spectra from a participant are shown in Figure 5, depicting Raman bands from both bone minerals, including 961 cm^{-1} and 1030 cm^{-1}, and bone matrix components, including 1260 cm^{-1}, 1660 cm^{-1}, and $3000 - 3600$ cm^{-1}. Although noisier, the HW spectra are vital for quantifying key biomarkers in deep tissue, specifically hydration (O-H stretch) and lipid/protein ratios (C-H/N-H stretch), which provide complementary data to the FP region for characterizing tissue states.

Notably, the zero offset spectrum showed minimal signs of the bone mineral peak (961 cm^{-1}), which increases with spatial offset reaching its maximum around 5 mm spatial offset. From these spectra, ENR metric curves (ENR as a function of spatial offset) were analyzed to identify the ideal offset (Supplementary Figure S5), where the maximum ENR corresponds to the optimal offset (Table S2). Interestingly, for 7 out of the 10 individuals, the ideal offset was identified as 7 mm (Table S3). These values are fairly close to previous in-vivo studies, which identified an 8 mm offset as optimal for the tibial region [11].

To investigate the effect of overlying tissue thickness, US measurements were performed by taking four images from the tibial regions corresponding to Raman measurement sites, and the median thickness was correlated with the ideal spatial offset. A significant correlation (Pearson

$r = 0.73, p < 0.05$) was observed between median tissue thickness and ideal offset values(Figure 5C). Interestingly, bone signals were detected through 14 mm of thick tissue with adequate SNR, where a 9 mm offset was found to be ideal, as increasing the offset further did not enhance the contribution of bone signals but increased overall noise. This aligns with previous in-vivo SORS studies on metacarpal and phalangeal bones, which show that thicker overlying tissue (e.g., in higher-BMI individuals) necessitates larger spatial offsets to optimize the bone-to-noise ratio[43]. It is known that increased tissue thickness marginally enhances superficial layer signals but drastically attenuates deeper (bone) layer contributions. Penetration depth depends on both the fraction of incident light reaching the bone and the detectable return signal from this layer[44, 42, 26].

It should be noted that the ideal offset for some participants with relatively thin overlying tissue (∼5 mm) was still found to be 7 mm, similar to the ideal offset for individuals with thicker tissue (∼7 mm). The discrepancy in optimal offsets for participants with similar tissue thicknesses (e.g., 5 mm vs. 7 mm) is plausibly explained by variations in the optical properties of the overlying tissue. The ideal offset metric value is also governed by the bulk optical properties (μ_a, μ_s', g, n) of the top layer and the relative strength of the bottom layer as described in Figure S6. Varying the spatial offset in Raman spectroscopy directly influences the balance of signals from surface and deeper bone layers, offering opportunities to isolate information from different depths. To assess the influence of inter-subject variability in overlying tissue optical properties, a sensitivity analysis was performed. The absorption coefficient μ_a and reduced scattering coefficient μ_s' of the top layer were scaled simultaneously by ±20% relative to their nominal values listed in Table 1 at both the excitation (830 nm) and Raman emission wavelengths (880 nm). These variations resulted in modest changes to the ENR magnitude and curve width. The optimal spatial offset shifted towards a lower value (by < 1 mm) with reduced attenuation, and towards a higher offset (by < 1 mm) with increased attenuation (Figure S6). This behaviour can be attributed to the fact that reduced attenuation (i.e. decrease in μ_a and μ_s') allows deeper penetration at shorter distances, whereas increased attenuation (i.e. increase in μ_a and μ_s') requires larger separations to achieve equivalent sampling depth. Crucially, the minimal magnitude of this shift demonstrates that the identified optimal offset is robust to realistic inter-subject variations in optical properties. In future work, we plan to develop analytical models that separate these layer-specific signals while incorporating scattering and absorption properties to address attenuation effects, thereby improving accuracy and consistency for quantitative assessment in-vivo.

4 Limitations

While the DWiSORS measurements system developed in this study achieved superior SNR under MPE limits compared to prior in-vivo work[43], enabling comprehensive molecular profiling, several limitations persist. First, the optical properties of overlying tissue (e.g., melanin content, collagen density) were not systematically characterized, despite their known impact on light absorption and scattering. Second, the small cohort size restricts the generalizability of findings, and further experimental work with larger, demographically diverse populations is required to disentangle the effects of body mass, skin pigmentation, and tissue heterogeneity on bone signal acquisition. Additionally, anatomical variations such as bone curvature or surface indents, which may introduce local depth fluctuations exceeding the illumination ring's spatial resolution, were not accounted for, potentially confounding signal consistency. While the current fixed ring geometry and analysis pipeline limit adaptability to such anatomical complexities, emerging advances in machine learning (ML), flexible probe and spectral unmixing techniques, coupled with multi-distance SORS datasets, could refine depth-resolved signal isolation and mitigate these challenges in future iterations.

5 Conclusion

This study demonstrates the design, validation, and application of a novel DWiSORS measurement framework, enabling comprehensive in-vivo molecular profiling of biological tissues—including both the fingerprint ($400 - 1800$ cm^{-1}) and high-wavenumber ($2500 - 3800$ cm^{-1}) spectral regions—in the tibia of healthy volunteers. While validated in the tibial mid-shaft, this framework is generalizable to other superficial bone regions with comparable overlying tissue thicknesses, such as the phalanx, metacarpal, and ulna (key osteoporosis-related fracture site). The novel ENR metric, which integrates bottom signal enhancement and noise, proved instrumental in identifying patient-specific optimal spatial offsets. Overall, this study demonstrates the technical feasibility of a novel DWiSORS framework for acquiring comprehensive, depth-resolved Raman spectra from bone in-vivo. The introduced ENR metric provides a quantitative basis for optimal offset selection. While validated here on a small cohort of healthy volunteers, the results are consistent with simulations and phantom studies, supporting the robustness of the approach. Future studies

involving larger cohorts with diverse body mass indices and skin tones are needed to disentangle the effects of optical properties (e.g., melanin absorption) and tissue thickness on bone Raman signals, advancing the translation of SORS to clinical practice. These findings pave the way for future non-invasive approaches to complement conventional techniques and for the longitudinal monitoring of bone-related disorders.

Acknowledgments
This publication has emanated from research conducted with the financial support of Taighde Éireann – Research Ireland, formerly Science Foundation Ireland (SFI/22/RP-2TF/10293) and Pathway Grant (24/PATH-S/12518). The research work is further supported by the IPIC Emerge Starting Grant (SFI-12/RC/2276_P2_IPIC SAE TP BONE Q Emerge 1). We thank all volunteers for their participation and time.

Conflicts of interest
SKVS and SAE are shareholders of BioPixS Ltd. with an interest in tissue optical phantoms. The other authors declare no conflicts of interest.

Author contributions
HM, PL, SKVS, SAE, RG conceptualization; HM, PL, AMJ, SKVS, SAE, RG, methodology; HM, SK, BJ, RG investigation, experiments; HM, PL, RG formal analysis, data curation ; RG, SKVS, SAE Supervision, Funding acquisition; HM, RG original draft; all authors review & editing

Data availability
The data that support the findings of this study are openly available at the following URL/DOI: https://github.com/Hui0930/DWiSORS.git

Supplementary data
Supplementary information is available online.

References

[1] Willers C, Norton N, Harvey NC, Jacobson T, Johansson H, Lorentzon M, et al. Osteoporosis in Europe: a compendium of country-specific reports. Archives of osteoporosis. 2022;17(1):23.

[2] Yeh EJ, Gitlin M, Sorio F, McCloskey E. Estimating the future clinical and economic benefits of improving osteoporosis diagnosis and treatment among postmenopausal women across eight European countries. Archives of Osteoporosis. 2023;18(1):68.

[3] Unal M, Creecy A, Nyman JS. The role of matrix composition in the mechanical behavior of bone. Current osteoporosis reports. 2018;16(3):205-15.

[4] Trémollieres FA, Pouillès JM, Drewniak N, Laparra J, Ribot CA, Dargent-Molina P. Fracture risk prediction using BMD and clinical risk factors in early postmenopausal women: sensitivity of the WHO FRAX tool. Journal of bone and mineral research. 2010;25(5):1002-9.

[5] Schwartz AV, Sellmeyer DE. Diabetes, fracture, and bone fragility. Current osteoporosis reports. 2007;5(3):105-11.

[6] Wang F, Zheng L, Theopold J, Schleifenbaum S, Heyde CE, Osterhoff G. Methods for bone quality assessment in human bone tissue: a systematic review. Journal of orthopaedic surgery and research. 2022;17(1):174.

[7] Choksi P, Rothberg A, Kraftson A, Miller N, Zurales K, Burant C, et al. Weight loss and bone mineral density in obese adults: a longitudinal analysis of the influence of very low energy diets. Clinical Diabetes and Endocrinology. 2018;4(1):14.

[8] Choksi P, Jepsen KJ, Clines GA. The challenges of diagnosing osteoporosis and the limitations of currently available tools. Clinical diabetes and endocrinology. 2018;4(1):12.

[9] Nguyen TV, Chu J, Sathiakumar C, Pocock NA. Reproducibility and concordance in quantitative ultrasound measurements between densitometers: a comparative study. Journal of Clinical Densitometry. 2003;6(4):337-44.

[10] Siris ES, Chen YT, Abbott TA, Barrett-Connor E, Miller PD, Wehren LE, et al. Bone mineral density thresholds for pharmacological intervention to prevent fractures. Archives of internal medicine. 2004;164(10):1108-12.

[11] Buckley K, Kerns JG, Vinton J, Gikas PD, Smith C, Parker AW, et al. Towards the in vivo prediction of fragility fractures with Raman spectroscopy. Journal of Raman Spectroscopy. 2015;46(7):610-8.

[12] Wang YXJ, Griffith JF, Leung JC, Kwok TC. Majority of hip fragility fractures among older people can be predicted by a DXA examination: an updated analysis of literature results and empirical Chinese data with a focus on the validation of the newly proposed osteofrailia criterion for men. Quantitative Imaging in Medicine and Surgery. 2025;15(1):473-85.

[13] Kanis JA, Cooper C, Rizzoli R, Reginster JY, of the European Society for Clinical SAB, of Osteoporosis (ESCEO) EA, et al. European guidance for the diagnosis and management of osteoporosis in postmenopausal women. Osteoporosis international. 2019;30(1):3-44.

[14] Mandair GS, Morris MD. Contributions of Raman spectroscopy to the understanding of bone strength. BoneKEy reports. 2015;4:620.

[15] Nieuwoudt MK, Shahlori R, Naot D, Patel R, Holtkamp H, Aguergaray C, et al. Raman spectroscopy reveals age-and sex-related differences in cortical bone from people with osteoarthritis. Scientific Reports. 2020;10(1):19443.

[16] Gautam R, Ahmed R, Haugen E, Unal M, Fitzgerald S, Uppuganti S, et al. Assessment of spatially offset Raman spectroscopy to detect differences in bone matrix quality. Spectrochimica Acta Part A: Molecular and Biomolecular Spectroscopy. 2023;303:123240.

[17] Morris MD, Mandair GS. Raman assessment of bone quality. Clinical Orthopaedics and Related Research®. 2011;469(8):2160-9.

[18] Koljenovic S, Bakker Schut T, Wolthuis R, de Jong B, Santos L, Caspers PJ, et al. Tissue characterization using high wave number Raman spectroscopy. Journal of biomedical optics. 2005;10(3):031116-6.

[19] Mo J, Zheng W, Low JJ, Ng J, Ilancheran A, Huang Z. High wavenumber Raman spectroscopy for in vivo detection of cervical dysplasia. Analytical chemistry. 2009;81(21):8908-15.

[20] Unal M, Akkus O. Raman spectral classification of mineral-and collagen-bound water's associations to elastic and post-yield mechanical properties of cortical bone. Bone. 2015;81:315-26.

[21] Wang J, Lin K, Zheng W, Yu Ho K, Teh M, Guan Yeoh K, et al. Simultaneous fingerprint and high-wavenumber fiber-optic Raman spectroscopy improves in vivo diagnosis of esophageal squamous cell carcinoma at endoscopy. Scientific reports. 2015;5(1):12957.

[22] Bergholt MS, Zheng W, Huang Z. Development of a multiplexing fingerprint and high wavenumber Raman spectroscopy technique for real-time in vivo tissue Raman measurements at endoscopy. Journal of biomedical optics. 2013;18(3):030502-2.

[23] Masson LE, O'Brien CM, Pence IJ, Herington JL, Reese J, Van Leeuwen TG, et al. Dual excitation wavelength system for combined fingerprint and high wavenumber Raman spectroscopy. Analyst. 2018;143(24):6049-60.

[24] Mosca S, Conti C, Stone N, Matousek P. Spatially offset Raman spectroscopy. Nature Reviews Methods Primers. 2021;1(1):21.

[25] Matousek P. Inverse spatially offset Raman spectroscopy for deep noninvasive probing of turbid media. Applied spectroscopy. 2006;60(11):1341-7.

[26] Maher JR, Berger AJ. Determination of ideal offset for spatially offset Raman spectroscopy. Applied spectroscopy. 2010;64(1):61-5.

[27] Pifferi A, Torricelli A, Bassi A, Taroni P, Cubeddu R, Wabnitz H, et al. Performance assessment of photon migration instruments: the MEDPHOT protocol. Applied optics. 2005;44(11):2104-14.

[28] Mosca S, Lanka P, Stone N, Konugolu Venkata Sekar S, Matousek P, Valentini G, et al. Optical characterization of porcine tissues from various organs in the 650–1100 nm range using time-domain diffuse spectroscopy. Biomedical optics express. 2020;11(3):1697-706.

[29] Gautam R, Mac Mahon D, Eager G, Ma H, Guadagno CN, Andersson-Engels S, et al. Fabrication and characterization of multi-biomarker optimized tissue-mimicking phantoms for multi-modal optical spectroscopy. Analyst. 2023;148(19):4768-76.

[30] Dépret B, Verkerk P, Hennequin D. Characterization and modelling of the hollow beam produced by a real conical lens. Optics communications. 2002;211(1-6):31-8.

[31] Maryam S, Konugolu Venkata Sekar S, Ghauri MD, Fahy E, Nogueira MS, Lu H, et al. Mobile multi-configuration clinical translational Raman system for oral cancer application. Analyst. 2023;148:1514-23. Available from: http://dx.doi.org/10.1039/D2AN01921C.

[32] Su JW, Wang Q, Tian Y, Madden L, Ling Teo EM, Becker DL, et al. Depth-sensitive Raman spectroscopy for skin wound evaluation in rodents. Biomedical optics express. 2019;10(12):6114-28.

[33] Şen T, Tüfekçioğlu O, Koza Y. Mechanical index. Anatolian journal of cardiology. 2015;15(4):334.

[34] Kothuri SK, MacMahon D, Lanka P, Derwin A, Byrne D, Dwyer RM, et al. Broadband time domain diffuse optical characterization of human cadaver bone from 500 to 1100 nm. Scientific Reports. 2025;15:25931. Available from: https://doi.org/10.1038/s41598-025-06138-y.

[35] Fang Q, Boas DA. Monte Carlo simulation of photon migration in 3D turbid media accelerated by graphics processing units. Optics express. 2009;17(22):20178-90.

[36] Yao R, Intes X, Fang Q. Direct approach to compute Jacobians for diffuse optical tomography using perturbation Monte Carlo-based photon "replay". Biomedical optics express. 2018;9(10):4588-603.

[37] Andersson-Engels S, Enejder AM, Swartling J, Pifferi A. Accelerated Monte Carlo models to simulate fluorescence of layered tissue. In: Photon Migration, Diffuse Spectroscopy, and Optical Coherence Tomography: Imaging and Functional Assessment. vol. 4160. SPIE; 2000. p. 14-5.

[38] Chen K, Sun M, Chen S. Determining ideal offsets of spatially offset Raman spectroscopy for transcutaneous measurements—A Monte Carlo study. Journal of Biophotonics. 2024;17(8):e202300564.

[39] Lux A, Conti C, Botteon A, Mosca S, Matousek P. Theoretical and Practical Considerations of Spatially Offset Raman Spectroscopy (SORS) and Micro-SORS. Applied Spectroscopy. 2025;79(6):919-32.

[40] Matousek P, Morris M, Everall N, Clark I, Towrie M, Draper E, et al. Numerical simulations of subsurface probing in diffusely scattering media using spatially offset Raman spectroscopy. Applied spectroscopy. 2005;59(12):1485-92.

[41] Pape HC, Kates SL, Hierholzer C, Bischoff-Ferrari HA. Senior trauma patients: an Integrated Approach. Springer Nature; 2022.

[42] Matousek P, Draper ER, Goodship AE, Clark IP, Ronayne KL, Parker AW. Noninvasive Raman spectroscopy of human tissue in vivo. Applied spectroscopy. 2006;60(7):758-63.

[43] Chen K, Massie C, Awad HA, Berger AJ. Determination of best Raman spectroscopy spatial offsets for transcutaneous bone quality assessments in human hands. Biomedical Optics Express. 2021;12(12):7517-25.

[44] Matousek P, Clark IP, Draper ER, Morris M, Goodship A, Everall N, et al. Subsurface probing in diffusely scattering media using spatially offset Raman spectroscopy. Applied spectroscopy. 2005;59(4):393-400.

Paper IV

Real-valued Intensity Transmission Matrix Based Multimode Fibre Beamshaping for Biophotonics Applications (Submitted for publication)

H. Ma, R. Gautam,S. Andersson-Engels and S. Konugolu Venkata Sekar.

(2026) *Optics Letters.*

Letter 1

Real-valued Intensity Transmission Matrix Based Multimode Fibre Beamshaping for Biophotonics Applications

HUI MA[1, 2,*], REKHA GAUTAM[1], STEFAN ANDERSSON-ENGELS[1, 3], AND SANATHANA KONUGOLU VENKATA SEKAR[1, 3]

[1] *Biophotonics@Tyndall, Tyndall National Institute, Lee Maltings Complex, Cork T12 R5CP, Ireland*
[2] *Engineering Science, Tyndall National Institute, Lee Maltings Complex, Cork T12 R5CP, Ireland*
[3] *School of Physics, University College Cork, College Road, Cork, Ireland*
[*] *hui.ma@tyndall.ie*

Compiled September 29, 2025

We present a real-valued intensity transmission matrix (RVITM) framework that enables phase-free structured illumination control through multimode fibres, overcoming long-standing challenges of modal scrambling from dispersion and bending. Unlike previous TM-based approaches that require complex-field measurements or interferometric detection, our method relies solely on 16 × 16 Hadamard intensity inputs, achieving deterministic synthesis of circularly symmetric illumination patterns that remain stable under fibre bending. As the first demonstration of intensity-only TM–based structured illumination for Raman spectroscopy, we implemented a 3 mm-radius ring pattern for inverse spatially offset Raman spectroscopy (iSORS) of a two-layer phantom. Compared with point illumination, the ring enhanced subsurface Raman features, confirming improved depth sensitivity without added system complexity. RVITM thus offers a calibration-efficient and mechanically robust route to fibre-delivered structured illumination, advancing minimally invasive spectroscopy and imaging applications.

http://dx.doi.org/10.1364/ao.XX.XXXXXX

Endoscopes are widely used in biomedical imaging for minimally invasive surgical guidance and diagnosis [1, 2]. Conventional endoscopic systems often rely on fibre bundles to project structured illumination patterns at the distal end [3]. While effective, these bundles constrain device miniaturisation due to their physical size, limiting access to narrow regions such as coronary arteries or cerebral vasculature. Reducing the footprint of structured illumination components is therefore critical for advancing the next generation of high-resolution, ultra-thin endoscopes. Multimode fibres (MMFs) provide a promising alternative due to their flexibility and high information capacity. However, light propagation in MMFs is strongly influenced by modal dispersion and mode coupling, which can arise from intrinsic fibre imperfections as well as external perturbations such as bending or movement. These effects redistribute energy among modes, scrambling spatial information and producing seemingly random speckle patterns at the output [4, 5].

The transmission matrix (TM) approach has emerged as a powerful method for characterising and controlling light propagation through complex media. It maps the relationship between input and output fields in a linear optical system, allowing imaging and beam shaping [6, 7]. Popoff et al. experimentally measured the optical TM in 2010 using sequential input patterns and interferometric detection of the corresponding output fields [7]. Since then, TM-based techniques have advanced rapidly, enabling applications such as focusing light through scattering layers, high-resolution imaging with multimode fibres, and customised beam shaping in disordered systems [8–10].

Full-field control through conventional transmission matrix techniques usually requires phase retrieval using holographic methods, which require stable reference arms, careful alignment, and long acquisition times. These limitations compromise system stability and restrict the applicability of such methods in movement-prone or in vivo environments. To address this, alternative approaches have been explored. Adaptive optics–based methods use devices such as SLMs or fibre bending actuators to dynamically compensate for modal perturbations [11, 12]. However, these systems involve complex feedback loops and bulky optics. Machine learning has also been applied to eliminate the requirement for phase retrieval, enabling TM estimation or direct image reconstruction from intensity-only data [13–15]. Although these methods improve robustness, they typically require large training datasets, iterative optimisation, and substantial computational resources, limiting their real-time clinical applicability.

To further simplify the system, researchers introduced the real-valued intensity transmission matrix (RVITM), which assumes a pseudo-linear relationship between input and output intensities [16]. By relying only on intensity measurements, the RVITM eliminates interferometric reference arms and phase stability requirements, making it inherently more tolerant to fibre motion and environmental perturbations. Building on this framework, we propose a method to generate circularly symmet-

ric illumination patterns through an MMF using RVITM. By distributing energy evenly along the azimuth, circularly symmetric illumination is inherently tolerant to angular phase perturbations induced by mode mixing. This rotational invariance suppresses local phase errors and smooths azimuthal fluctuations, leading to more stable output patterns under fibre bending.

In addition, circularly symmetric (ring) illumination is particularly advantageous for biomedical spectroscopy and imaging, as it distributes light azimuthally around the collection region, providing uniform sampling across all radial directions. This geometry naturally matches the cylindrical structures of many tissues, such as bones or blood vessels, and enhances subsurface sensitivity by increasing the average photon path length before collection [17]. Compared with stripe or linear illumination, which excites along a single direction and produces anisotropic sampling, ring illumination offers improved depth selectivity and robustness to local phase variations or speckle in multimode fibres. Despite advances in transmission matrix–based fibre control, circularly symmetric illumination through MMFs has not yet been demonstrated using a RVITM.

In this Letter, we present a method for calibrating a multimode fibre (MMF) using a real-valued intensity transmission matrix (RVITM) to generate circularly symmetric ring illumination at the fibre tip. We demonstrate that the illumination remains robust under controlled bending (radius ≈ 6 cm), and as a proof-of-concept application, apply it to inverse spatially offset Raman spectroscopy (iSORS) on a two-layer phantom, achieving enhanced subsurface sensitivity compared with conventional point-source excitation.

The experimental arrangement is shown schematically in Fig. 1A. A 730 nm laser diode (0811A100-B Fat Boy, Innovative Photonics Solutions) was collimated with a fibre collimator (F220FC-780, Thorlabs) and directed onto a spatial light modulator (SLM, 1920 × 1080 pixels, L3C07U-85G13, Epson). The SLM, consisting of a liquid crystal display (LCD) between crossed polarisers, enabled binary amplitude modulation of the incident beam. The modulated light was coupled into a multimode fibre (MMF, 400 μm core diameter, NA 0.22, length 1 m, M28L01, Thorlabs) via a 20× objective lens (0.4 NA, RMS20X, Thorlabs). At the distal end of the fibre, the output intensity distributions were recorded using a CMOS camera (CS165MU1, Zelux® 1.6 MP Monochrome, Thorlabs).

To characterise the fibre, we employed the real-valued intensity transmission matrix (RVITM), which assumes a pseudo-linear relationship between input and output intensities [16]. A Hadamard basis of order 16×16 was selected as it offers a balance between pattern complexity and acquisition speed, resulting in 256 effective input channels. To match the aperture of the coupling objective, SLM pixels were grouped into macropixels of 37×37, with each macropixel corresponding to one Hadamard element. Each binary Hadamard pattern was sequentially displayed on the SLM, and the corresponding distal output speckle was recorded. Background subtraction was applied to improve the signal-to-noise ratio. The RVITM was obtained directly from these input–output pairs following the procedure in Ref. [16].

The RVITM was then used for beam shaping. To generate a desired target illumination pattern $\mathbf{I}_{\text{target}}$, the corresponding input distribution was computed as

$$\mathbf{I}_{\text{in}} = \text{RVITM}^{+} \cdot \mathbf{I}_{\text{target}}, \quad \textbf{(1)}$$

where RVITM^{+} denotes the Moore–Penrose pseudo-inverse. The calculated input pattern was displayed on the SLM to produce the desired output at the fibre tip, as illustrated in Fig. 1 (b).

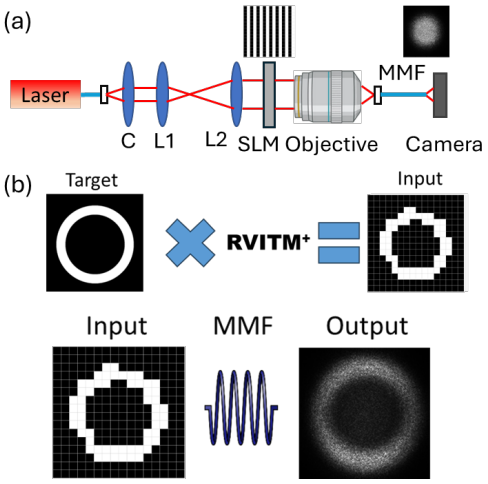

Fig. 1. (a) Experimental setup for TM measurement and beam shaping through a MMF (b) Principle and demonstration of ring illumination synthesis using the RVITM.

Using the RVITM, we first synthesised ring-shaped illumination at the distal end of the fibre. Figure 2 shows representative patterns generated through the multimode fibre. Two single rings with different radii are displayed in Fig. 2(a) and (b), illustrating precise control over the output distribution. Similar behaviour was observed for an intermediate radius (not shown), confirming that ring size can be easily tuned. Figure 2(c) demonstrates a double-ring pattern, highlighting the ability to generate multiple concentric rings simultaneously with minimal cross-talk. Finally, Fig. 2(d) shows a composite pattern featuring a Gaussian-like bright centre, surrounded by a dark ring and an outer halo. This illustrates the flexibility of the RVITM in creating complex illumination profiles, combining central and peripheral structures in a single pattern. In all cases, the measured intensity closely matches the target distribution, validating the effectiveness of the RVITM-based beam shaping.

To evaluate robustness against perturbation, the fibre was wound around a storage reel (FSR3, Thorlabs) with a bending radius of approximately 6 cm. The resulting output patterns were compared with those obtained using a straight fibre. Captured intensity distributions were normalised to [0–1]. Cosine similarity and structural similarity index (SSIM) were calculated on the full two-dimensional images. To account for the circular symmetry, radial intensity profiles were extracted with respect to the ring centre, and Pearson correlation and normalised root mean square error (NRMSE) were computed.

As shown in Fig. 3(a), the ring pattern generated at the fibre output prior to bending serves as the reference. After bending, the output still exhibits a well-defined ring, as seen in Fig. 3(b), although local speckle features appear altered. To quantify the structural preservation, radial intensity profiles were extracted from both images, shown in Fig. 3(c). These profiles overlap almost perfectly, confirming that the ring geometry is maintained. Table 1 summarises the quantitative similarity analysis. The 2D

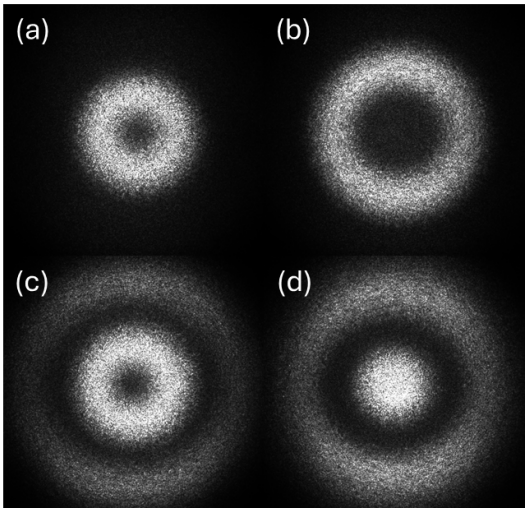

Fig. 2. Beam shaping through a multimode fibre using the RVITM. (a,b) Single rings of different radii, (c) double-ring pattern, (d) composite pattern with a Gaussian-like bright centre, a surrounding dark ring, and an outer halo.

image comparison yields a cosine similarity of 0.926, confirming strong global agreement, while the SSIM value of 0.479 indicates that pixel-wise fidelity is reduced by speckle fluctuations. In contrast, the radial profile analysis demonstrates that the ring geometry is preserved: the Pearson correlation reaches 0.9995, and the NRMSE is as low as 0.034. These results highlight that, although local speckle varies, the overall ring structure remains highly robust under fibre bending.

Table 1. Similarity metrics for robustness evaluation under fibre bending (radius ≈ 6 cm).

Metric	Value
Cosine similarity (2D)	0.926
SSIM (2D)	0.479
Pearson correlation (radial)	0.9995
NRMSE (radial)	0.034

As a case study, the proposed method was applied to an inverse SORS configuration using a two-layer phantom prepared following the protocol described in Ref. [18]. The bottom layer consisted of a compacted mixture of hydroxyapatite (HA) granules (912204, Sigma-Aldrich) and ammonium chloride (213330, Sigma-Aldrich) in a 1:1 weight ratio, ground using a mortar and pestle and sealed with a CaF_2 window (CAFP50-1R, Crystran, UK). The top layer was a 2 mm-thick MedPhot B2 silicone phantom (MEDPHOT, BioPixS) [19]. Raman excitation was provided at 730 nm through a multimode fibre, forming a ring illumination with a 3 mm radius at the phantom surface. The output power at the fibre tip was 3 mW. Backscattered light from the central region of the phantom was collected and delivered to a Raman spectrometer (Acton LS785, f/2, Teledyne Princeton

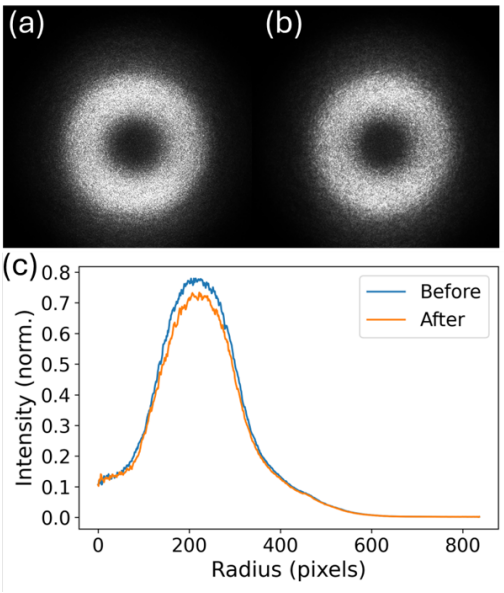

Fig. 3. (a) Ring pattern before fibre bending. (b) Ring pattern after fibre bending, showing that the overall structure is preserved despite local speckle variations. (c) Radial intensity profiles extracted from (a) and (b), aligned to the same centre.

Instruments, USA) equipped with a deep-depletion CCD camera. Spectra were acquired with an integration time of 80 s. For comparison, measurements were also performed on the same phantom using conventional point-source illumination.

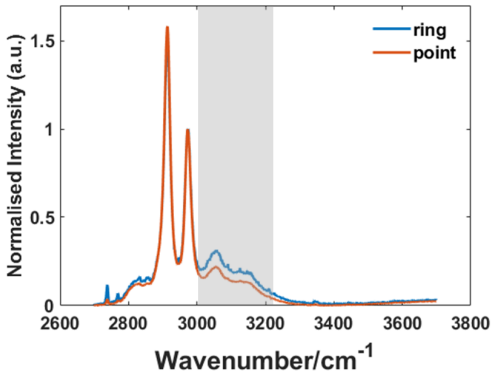

Fig. 4. Raman spectra from the two-layer phantom under ring and point illumination, normalised to the 2973 cm^{-1} silicone peak.

Figure 4 shows the Raman spectra acquired from the two-layer phantom under ring and point illumination. All spectra were normalised to the 2973 cm^{-1} band, which arises from the

silicone phantom and serves as a marker for the top layer. The spectral region between 3000 and 3200 cm^{-1}, characteristic of the hydroxyapatite–ammonium chloride mixture in the bottom layer, is highlighted in gray. This region exhibited a stronger relative contribution when using ring illumination compared with point illumination. This enhancement indicates that the ring illumination geometry increased the sensitivity to subsurface Raman signals while reducing the relative contribution from the overlying silicone. The results therefore demonstrate the capability of the inverse SORS approach to improve layer selectivity in turbid media, while also highlighting one potential application of the beam shaping system in generating tailored illumination profiles. Beyond iSORS, the same platform could be extended to other Raman modalities and multimodal biophotonics techniques where customised excitation patterns are required.

The results demonstrate that RVITM-based beam shaping provides a robust and flexible approach for controlling light propagation through multimode fibres. Unlike conventional transmission matrix techniques, which rely on interferometric phase retrieval and are highly sensitive to fibre bending and environmental perturbations [7, 8], the RVITM approach uses intensity-only measurements, eliminating the need for reference arms and holographic detection [16]. The robustness of the system under fibre bending, verified through controlled tests, ensures stable output patterns and enables reliable implementation in fibre-based Raman probes. Compared with conventional iSORS systems that use fixed optical components such as axicons [20], the RVITM-based method is entirely axicon-free, simplifying the optical design and reducing the system footprint, which is critical for integration into minimally invasive or in-vivo probes. In addition, in contrast to the fixed-angle coupling approach reported in Ref. [21], RVITM allows independent control over both ring radius and thickness, enabling tailored illumination profiles to match specific tissue geometries or target depths and optimise subsurface sensitivity. The ability to generate complex patterns, including double rings or composite structures, further expands the versatility of the system and opens the door to customised excitation in a variety of biomedical imaging and spectroscopy modalities.

Beyond the case study, the RVITM-based platform offers broader applicability across multimode fibre–based biophotonics. Circularly symmetric illumination enhances subsurface sensitivity by distributing light uniformly around the collection region, which is advantageous for transmission Raman, fluorescence imaging, or other multimodal techniques [17]. The combination of compact design, bending robustness, and flexible pattern control establishes a practical framework for ultra-thin endoscopic probes and other minimally invasive imaging systems. Furthermore, the RVITM approach is inherently tolerant to dynamic perturbations, suggesting potential for use in living tissue or other movement-prone environments. While the current implementation relies on sequential Hadamard patterns for calibration, the method lays the groundwork for faster, adaptive, or real-time strategies, potentially combined with machine learning, to further accelerate imaging and extend the range of possible illumination profiles. Overall, RVITM-based beam shaping provides a versatile, robust, and application-ready method for generating customised illumination in complex turbid media, bridging the gap between high-fidelity fibre control and practical in-vivo applications.

We have demonstrated a method for generating circularly symmetric illumination patterns through a multimode fibre using a RVITM. The approach enables flexible beam shaping without interferometric detection, offering robustness against fibre bending and environmental perturbations. Ring illumination was shown to preserve its geometry under perturbation and, when applied to inverse spatially offset Raman spectroscopy, enhanced subsurface sensitivity in a two-layer phantom compared with conventional point-source excitation. The present work therefore lays the groundwork for next-generation fibre-based imaging systems capable of delivering customised illumination profiles, supporting a range of biomedical applications from deep-tissue spectroscopy to multimodal imaging.

Funding. The research work was supported by the Science Foundation Ireland (SFI) IPIC Biomedical theme (Grant Nos. SFI-12/RC/2276_P2 and SFI/22/RP-2TF/10293).

Acknowledgment. The authors would like to thank Baptiste Jayet for helpful discussions on technical aspects of this work.

Disclosures. Sanathana Konugolu Venkata Sekar and Stefan Andersson-Engels are shareholders of BioPixS Ltd. with an interest in tissue optical phantoms. The other authors declare no conflicts of interest.

Data availability. Data underlying the results presented in this paper are not publicly available at this time but may be obtained from the authors upon reasonable request.

REFERENCES

1. G. Berci and K. A. Forde, Surg. endoscopy **14**, 5 (2000).
2. P. Valdastri, M. Simi, and R. J. Webster III, Annu. review biomedical engineering **14**, 397 (2012).
3. J. P. Angelo, M. van de Giessen, and S. Gioux, Biomed. optics express **8**, 5113 (2017).
4. A. W. Snyder, J. D. Love *et al.*, *Optical waveguide theory*, vol. 175 (Chapman and hall London, 1983).
5. D. Gloge, Bell Syst. Tech. J. **51**, 1767 (1972).
6. A. P. Mosk, A. Lagendijk, G. Lerosey, and M. Fink, Nat. photonics **6**, 283 (2012).
7. S. M. Popoff, G. Lerosey, R. Carminati, *et al.*, Phys. review letters **104**, 100601 (2010).
8. S. M. Popoff, G. Lerosey, M. Fink, *et al.*, New J. Phys. **13**, 123021 (2011).
9. Y. Choi, C. Yoon, M. Kim, *et al.*, Phys. review letters **109**, 203901 (2012).
10. S. Turtaev, I. T. Leite, T. Altwegg-Boussac, *et al.*, Light. Sci. & Appl. **7**, 92 (2018).
11. S. Resisi, Y. Viernik, S. M. Popoff, and Y. Bromberg, APL Photonics **5** (2020).
12. R. A. Panicker, J. M. Kahn, and S. P. Boyd, J. Light. technology **26**, 1295 (2008).
13. N. Borhani, E. Kakkava, C. Moser, and D. Psaltis, Optica **5**, 960 (2018).
14. A. Turpin, I. Vishniakou, and J. D. Seelig, Opt. express **26**, 30911 (2018).
15. B. Rahmani, D. Loterie, G. Konstantinou, *et al.*, Light. science & applications **7**, 69 (2018).
16. T. Zhao, S. Ourselin, T. Vercauteren, and W. Xia, Opt. express **28**, 20978 (2020).
17. S. S. Alshahrani, Y. Yan, N. Alijabbari, *et al.*, J. biomedical optics **24**, 046004 (2019).
18. H. Ma, S. K. V. Sekar, P. Lanka, *et al.*, "Noninvasive in-vivo bone characterisation," in *European Conference on Biomedical Optics*, (Optica Publishing Group, 2025), pp. W5A–5.
19. A. Pifferi, A. Torricelli, A. Bassi, *et al.*, Appl. optics **44**, 2104 (2005).
20. P. Matousek, Appl. spectroscopy **60**, 1341 (2006).
21. K. M. Khan, S. B. Dutta, N. Kumar, *et al.*, J. Biophotonics **12**, e201900140 (2019).

Chapter 8

General Discussion

Structured illumination has emerged as a powerful strategy for enhancing the performance of optical diagnostic techniques in biophotonics. This chapter discusses the significance of the structured illumination and beam shaping approaches developed and employed in this thesis. By comparing the implemented systems with conventional technologies, the discussion highlights how precise control over the spatial distribution of light, when combined with various biophotonics modalities, can lead to significant improvements in both imaging and spectroscopic performance.

The RVITM-based multimode fibre platform demonstrates that intensity-only transmission matrix approaches can robustly generate complex illumination patterns with minimal sensitivity to fibre bending or environmental perturbations. Unlike conventional transmission matrix methods that require interferometric phase measurements [117, 118], RVITM eliminates the need for reference arms or holographic detection, enabling practical and compact implementations. The ability to generate rings of varying radius and thickness, double rings, and composite patterns provides versatile illumination control, which is advantageous for fibre-based Raman or fluorescence probes. Compared with fixed-angle or axicon-based systems [19, 113], RVITM reduces optical complexity and footprint while enabling tailored illumination to match specific tissue geometries, laying the groundwork for minimally invasive and bend-tolerant optical probes.

The development and implementation of the Köhler integrator-based illumination system proves that manipulating light enables sensitive and reliable detection in optical imaging. For UCNP imaging, the uniform illumination ensured that measured intensity variations came from differences in biomarker expression rather than fluctuations in the illumination field. Using UCNPs as the labelling agent addressed several limitations of conventional staining methods. The gold standard for breast cancer diagnosis is using immunohistochemistry (IHC) with HRP (horseradish peroxidase)/DAB staining. This method is absorption-based and limited by the optical pathlength of white light through the sample. At high DAB concentrations, the slide becomes opaque to white light. Reducing the primary antibody concentration and repeating the labelling can prevent this saturation, but it lowers sensitivity for weakly expressed targets, thereby restricting the overall dynamic range. On the contrary, the contrast in UCNP labelling is obtained by the emission process which allows it to be limited only by the non-specific labelling of surrounding tissue. In this study, the signal-to-background ratio was found to be 40, showing a 25-fold improvement over DAB. Additionally, UCNPs are highly photostable and resistant to photobleaching compared to conventional fluorescent dyes. Quantum dots can reduce photobleaching but still suffer from autofluorescence background[182]. The UCNP imaging

provides an anti-Stokes emission approach, which eliminates tissue autofluorescence.

While uniformity was key in imaging, selective illumination proved essential for deep tissue spectroscopy. The DWiSORS system demonstrates how manipulation of illumination pattern can enhance detection sensitivity for in vivo measurement. By using axicon-based ring illumination, the system enhances subsurface bone signals while suppressing contributions from overlying tissue layers. By systematically adjusting the source-detector offset and introducing the enhancement-to-noise ratio (ENR) metric, the system identifies the optimal illumination geometry for different tissue thicknesses, achieving sensitive detection of hydroxyapatite concentration and bone hydration through 5–14 mm of tissue. Compared with traditional SORS systems [183, 184], the ENR metric accounts for both signal enhancement and noise, providing reproducible quantitative assessment. These results highlight the critical role of tailored illumination in balancing depth sensitivity and signal quality in turbid media.

Finally, the dynamic phantom demonstrates that engineered illumination can support device calibration and standardization. By modulating light spatially and temporally, the phantom simulates physiologically realistic PPG signals and vascular structures. Unlike previous designs [178, 180], the system offers fine control over target size, modulation depth, and multi-wavelength synchronization, enabling realistic reproduction of biological signals, motion artifacts, and perfusion changes. This allows accurate evaluation of device performance under controlled and reproducible conditions, illustrating how precise illumination can translate into practical tools for both industrial and academic research.

Together, these findings demonstrate that the future of biophotonics will depend not only on improved detectors, algorithms or labelling agents, but on the degree to which illumination can be tailored to the measurement context. Structured illumination provides a unifying framework for achieving this control in multiple modalities, whether the goal is to enhance subsurface signals, standardise clinical devices, or unlock new regimes of minimally invasive diagnostics. By showing that illumination can be adaptive, quantitative, and application-specific, this work lays the foundation for next-generation optical systems where light is no longer treated as a passive input, but as an actively engineered component of the measurement itself.

Chapter 9

Conclusions and future perspective

9.1 Conclusion

This thesis establishes structured illumination and beam shaping as a powerful strategy for improving performance, reproducibility, and depth sensitivity in biophotonic diagnostics. Rather than treating illumination as a passive experimental parameter, this work demonstrates that active control of illumination can enhance both imaging and spectroscopic measurements.

Across a diverse set of modalities, the thesis shows that tailored illumination enables more selective, quantitative, and reliable signal generation without increasing invasiveness or system complexity. In imaging applications, uniform and controlled illumination improves the accuracy of biomarker quantification by ensuring that measured contrast originates from the sample rather than from spatial variations in excitation. In spectroscopic applications, structured illumination geometries enhance sensitivity to subsurface signals while suppressing unwanted contributions from overlying layers. In addition, the use of programmable illumination in dynamic phantoms demonstrates how optical control can be extended beyond measurement to enable standardisation and calibration of diagnostic devices.

The key contribution of this thesis is the demonstration that illumination control provides a unifying framework across biophotonics. The techniques developed here are modality agnostic, experimentally robust, and compatible with translational constraints such as miniaturisation, motion tolerance, and reproducibility. By avoiding reliance on complex interferometric control or fragile alignment, the approaches presented are well suited to real world biomedical environments.

From a broader perspective, this thesis contributes to a shift in how optical systems for biomedical diagnostics are designed. It shows that improvements in performance can be achieved by controlling how light interacts with complex biological media spatially and temporally, rather than by increasing optical power, acquisition time, or system complexity. By demonstrating the impact of structured illumination across multiple applications, this thesis contributes to the development of more robust, quantitative, and clinically relevant optical diagnostic technologies.

9.2 Future Perspective

The systems developed in this thesis have demonstrated the potential of structured illumination and beam shaping for enhancing optical diag-

nostics across a range of biophotonics applications. At present, all experimental setups are implemented in benchtop configurations involving bulky optical components, which limits their use in clinical or portable applications. The direction for future work is to transform these systems into miniaturised, fibre based implementations by using TM based control of the illumination patterns. The RVITM approach demonstrated for beam shaping at the distal end of the MMF provides a promising foundation for integrating various illumination patterns into a single platform for endoscopic applications. For example, ring shaped illumination generated using TM control was applied in the iSORS system to enhance subsurface signal sensitivity, while top hat illumination has potential for endoscopic in vivo multispectral or fluorescence imaging. Future work will explore the generation of additional structured patterns, such as sinusoidal profiles, to support advanced imaging techniques that require spatial frequency modulation.

Future work of the dynamic phantom will focus on enhancing its physiological realism and relevance for device characterisation. Multiple light guides will be integrated within the phantom to replicate more complex and anatomically accurate vascular geometries, enabling the simulation of branching and pulsatile flow patterns that better represent the real tissue vasculature. The optical properties of the static top layer will be modified to mimic a range of skin tones. This will allow systematic investigation of skin pigmentation effects on the performance of pulse oximeters. By extending the functionality of the dynamic phantom in this way, the system can serve as a more comprehensive and standardised platform for the evaluation and calibration of wearable and clinical optical devices.

Together, these future developments aim to bridge the gap between advanced optical system design and clinical translation. By miniaturising the beam shaping platforms and integrating them into fibre based probes, and by enhancing the realism of the dynamic phantom, this research forms the basis for practical, standardised, and sensitive diagnostic tools.

Comments on the Papers

I **High contrast breast cancer biomarker semi-quantification and immunohistochemistry imaging using upconverting nanoparticles**

I am the shared first author of this paper. This paper presents a Köhler-illuminated microscope for high-contrast imaging of upconverting nanoparticles (UCNPs) in breast cancer tissues. A near-infrared laser with beam-shaping optics provides uniform UCNP excitation, while spectral filters isolate emissions captured by a scientific camera. Integrated multimodal imaging (H&E, DAPI, DAB) enables comprehensive tissue analysis. Optical optimisation minimises background interference, enabling precise HER2 biomarker visualisation. The system demonstrates superior sensitivity over conventional chromogenic methods, supporting semi-quantitative HER2 assessment critical for clinical histopathology.

My contributions to this work included the complete design and implementation of the Köhler integrator based microscope, and the development of the imaging scheme. I was also responsible for acquiring and analysing the imaging data, developing the algorithm used for semi-quantitative HER2 assessment, and preparing the manuscript in collaboration with co-authors.

II **Light-guided dynamic phantom to mimic microvasculature for biomedical applications: an exploration for pulse oximeter**

This study presents a light-guided dynamic phantom mimicking microvasculature. An LCD-polymer fibre integration enables real-time absorption control, eliminating angular dependency. Characterised at four wavelengths (455–940 nm), it synthesised PPG signals with adjustable heart rates (80–120 bpm) and SpO_2 levels (86–100%). Validation confirmed accurate physiological replication, outperforming blood-based phantoms. The design offers a stable calibration tool for pulse oximeters, addressing limitations in shelf life, resolution, and response time.

I was responsible for every stage of the project, including the planning, optical and mechanical design, selection and integration of components. I developed the control system for modulating the absorption properties and led the design of the experimental protocol for signal acquisition and physiological signal simulation. I also performed all measurements and data analysis, including signal validation across different wavelengths and physiological conditions. In addition, I authored the manuscript and coordinated feedback from collaborators throughout the publication process.

III **Raman Spectroscopy based framework for In-Vivo Assessment of Bone Composition**

This study introduces a dual-wavelength inverse spatially offset Raman spectroscopy (DWiSORS) framework for in-vivo assessment of bone composition. The system combines ring illumination with dual excitation (730/830 nm) to acquire both fingerprint and high-wavenumber regions, enabling comprehensive molecular profiling beneath turbid tissue. A new enhancement-to-noise ratio (ENR) metric was proposed to determine the optimal spatial offset for subsurface sensing. The framework was validated through Monte Carlo simulations, tissue-mimicking phantoms, and in-vivo measurements on ten healthy participants. Results confirmed patient-specific optimal offsets (5–9 mm), demonstrating the feasibility of Raman-based bone assessment at depths up to 14 mm, with sensitivity to mineral and hydration variations. This approach advances clinical translation of SORS for osteoporosis diagnostics.

I led the full development of the system and methodology. I designed the optical setup, selected and integrated all components. I fabricated and characterised the tissue and bone phantoms, conducted Monte Carlo simulations to derive the ENR metric, and established the experimental protocol for both phantom and in-vivo measurements. I performed all data acquisition and spectral processing, including fluorescence background removal, ENR computation, and validation across different offsets and tissue conditions. I coordinated the in-vivo ethical approval process and participant measurements. In addition, I wrote the manuscript and managed revisions and feedback from collaborators throughout submission.

IV **Real-valued Intensity Transmission Matrix Based Multimode Fibre Beamshaping for Biophotonics Applications (Submitted for publication)**

This study presents a real-valued intensity transmission matrix (RVITM) framework for structured illumination through multimode fibres, enabling controlled ring and composite beam profiles without interferometric detection. By calibrating the fibre response using a 16×16 Hadamard basis, circularly symmetric patterns were synthesised with tunable radii and demonstrated robustness under fibre bending. As a proof-of-concept, a 3 mm ring was deployed in an inverse spatially offset Raman spectroscopy (iSORS) configuration using a two-layer tissue-mimicking phantom, enhancing subsurface Raman sensitivity compared with conventional point illumination. This axicon-free, software-defined beam-shaping strategy offers a compact solution for fibre-based spectroscopy and imaging.

I took an active role in defining the problem and setting the research direction. Noting the limitations of conventional axicon-based iSORS systems, I proposed multimode fibre control as a compact alternative and developed the RVITM strategy. I planned the project, designed the optical architecture, built the experimental setup, and implemented the Hadamard calibration and data processing workflows. I fabricated the tissue phantoms, performed the validation study, conducted all measurements and analysis, and authored and coordinated the manuscript through publication.

Reflection and Perspective

Reflecting on my time as a PhD student, I see a journey defined not only by the research presented in this thesis but also by the development of skills, confidence, and perspective that have shaped who I am today. When I began, I was hesitant to speak up in meetings, unsure of how to present my work confidently, and reluctant to reach out to others. Over time, this PhD became far more than a series of experiments. It became a journey of self-discovery, learning how to communicate ideas, seek collaboration, and situate my work within the broader scientific community.

Attending events such as the Biophotonics Summer School and international conferences provided opportunities to connect with peers and leading researchers across the globe. Initially, these environments felt intimidating, yet I gradually became comfortable asking questions in group meetings, engaging in discussions, and giving oral presentations at conferences. Reaching out for connections became not a source of anxiety but a way to learn, share ideas, and broaden my perspective. These experiences highlighted how meaningful conversations can ignite new ideas and underscored the value of building connections beyond the confines of the laboratory.

Throughout this journey, I have grown from a reserved researcher focused solely on experiments into someone who embraces collaboration, actively seeks feedback, and sees challenges as gateways to innovation rather than obstacles. Looking back, I wish I had explored opportunities for collaboration outside the institute sooner, as they often opened doors to new perspectives and unexpected ideas.

This PhD has also shaped my ambitions. I aspire to bridge academic research with industry-driven innovation, developing technologies that address real-world challenges while pushing the boundaries of scientific understanding. The projects I have worked on, from advanced beam shaping and Raman spectroscopy to dynamic phantom development, have strengthened my conviction that impactful research must remain closely tied to tangible applications. I am excited to continue exploring this space, combining rigorous research with translational impact, and contributing to solutions that could improve human health.

Rather than seeing this thesis as an end point, I view it as a launchpad, a foundation for a career defined by curiosity, collaboration, and the ambition to leave a meaningful mark on the field of biophotonics.

Acknowledgements

First and foremost, I would like to express my deepest gratitude to my supervisors, **Stefan Anderson-Engels**, **Sanathana Konugolu Venkata Sekar** and **Rekha Gautam**, for their invaluable guidance, encouragement and unwavering support throughout my PhD journey. Their expertise and insightful advice have been instrumental in shaping both my research and my growth as a researcher. Their expertise, patience and insightful advice have been instrumental in shaping both my research and my development as a scientist.

I would also like to acknowledge the generous financial support that made this work possible. This research was carried out as part of the Biophotonics@Tyndall team, based at Tyndall National Institute in Ireland, and was kindly supported by Research Ireland (RI) grants SFI-12/RC/2276_P2 and SFI-22/RP-2TF/10293.

I am deeply thankful to my colleagues in Biophotonics@Tyndall, especially **Dario**, **Daniyal** and **Hasti**, for their constant support, collaboration and friendship. We joined the group at a similar time and are now approaching graduation together, and it has been a privilege to share this journey with them, both inside and outside the lab. I would also like to thank **Baptiste** for his invaluable support and guidance on the beamshaping project, **Kasia**, **Simon**, **Ray**, **Shree**, **Pranav**, and **Gokhan** for their thoughtful advice regarding my career plans, and **Suzanne** for her generous help with SEM imaging. Their expertise, insights and encouragement have greatly enriched my research experience and professional development. I would also like to thank **Kon** for kindly proofreading my manuscript. As I am not a native English speaker, his help with the language and clarity of expression has been invaluable. My thanks also go to **Sarah**, our group administrator, for her support, which made my journey much smoother. I am grateful to all the volunteers who participated in my clinical trial. Their willingness to contribute their time and effort made this part of the research possible and is sincerely appreciated. I would also like to thank **Atieh**, **Sumedha** and **Suvam** for their company in the gym, and **Somali** for organising all the outings and social events, which brought fun and balance to the busy research days.

Finally, I would like to thank my dear friend **Viktória** for her constant support and encouragement, which brought me strength and comfort throughout this journey. Above all, I am profoundly grateful to my family, especially my mother, **Yinghong Xie**. Although we are not from a wealthy family, her sacrifices and unwavering support have made it possible for me to pursue my dreams and see the broader world. Her love, patience and belief in me have been my greatest source of strength and motivation, and this achievement would not have been possible without her.

References

[1] Alexis Wise, Emily MacIntosh, Nirusan Rajakulendran, and Zayna Khayat. Transforming health: Shifting from reactive to proactive and predictive care. *Transforming Health MaRS Market Insights*, 2016.

[2] Paul Grant. Proactive care. In *The Virtual Hospital*, pages 87–107. Springer, 2024.

[3] Dempsey S Springfield and Andrew Rosenberg. Biopsy: complicated and risky, 1996.

[4] David J Brenner and Eric J Hall. Computed tomography—an increasing source of radiation exposure. *New England journal of medicine*, 357(22):2277–2284, 2007.

[5] Fred A Mettler Jr, Walter Huda, Terry T Yoshizumi, and Mahadevappa Mahesh. Effective doses in radiology and diagnostic nuclear medicine: a catalog. *Radiology*, 248(1):254–263, 2008.

[6] Girish Katti, Syeda Arshiya Ara, and Ayesha Shireen. Magnetic resonance imaging (mri)–a review. *International journal of dental clinics*, 3(1):65–70, 2011.

[7] Natan T Shaked, Stephen A Boppart, Lihong V Wang, and Jürgen Popp. Label-free biomedical optical imaging. *Nature photonics*, 17 (12):1031–1041, 2023.

[8] Costas Balas. Review of biomedical optical imaging—a powerful, non-invasive, non-ionizing technology for improving in vivo diagnosis. *Measurement science and technology*, 20(10):104020, 2009.

[9] Shanmuga Sundar Dhanabalan, Sharath Sriram, Sumeet Walia, Sivanantha Raja Avaninathan, Marcos Flores Carrasco, and Madhu Bhaskaran. Wearable label-free optical biodetectors: Progress and perspectives. *Advanced Photonics Research*, 2(2): 2000076, 2021.

[10] Silke Aumann, Sabine Donner, Jörg Fischer, and Frank Müller. Optical coherence tomography (oct): principle and technical realization. *High resolution imaging in microscopy and ophthalmology: new frontiers in biomedical optics*, pages 59–85, 2019.

[11] Turgut Durduran, Regine Choe, Wesley B Baker, and Arjun G Yodh. Diffuse optics for tissue monitoring and tomography. *Reports on progress in physics*, 73(7):076701, 2010.

[12] Paul Beard. Biomedical photoacoustic imaging. *Interface focus*, 1 (4):602–631, 2011.

[13] EE Lawson, BW Barry, AC Williams, and HGM Edwards. Biomedical applications of raman spectroscopy. *Journal of Raman Spectroscopy*, 28(2-3):111–117, 1997.

[14] Christoph Krafft and Jürgen Popp. The many facets of raman spectroscopy for biomedical analysis. *Analytical and bioanalytical chemistry*, 407:699–717, 2015.

[15] Yiqun Ji, Chenxin Zeng, Fenli Tan, Anwei Feng, and Jizhou Han. Non-uniformity correction of wide field of view imaging system. *Optics Express*, 30(12):22123–22134, 2022.

[16] Mats GL Gustafsson. Surpassing the lateral resolution limit by a factor of two using structured illumination microscopy. *Journal of microscopy*, 198(2):82–87, 2000.

[17] David J Cuccia, Frederic Bevilacqua, Anthony J Durkin, Frederick R Ayers, and Bruce J Tromberg. Quantitation and mapping of tissue optical properties using modulated imaging. *Journal of biomedical optics*, 14(2):024012–024012, 2009.

[18] Stefan W Hell and Jan Wichmann. Breaking the diffraction resolution limit by stimulated emission: stimulated-emission-depletion fluorescence microscopy. *Optics letters*, 19(11):780–782, 1994.

[19] Pavel Matousek. Inverse spatially offset raman spectroscopy for deep noninvasive probing of turbid media. *Applied spectroscopy*, 60 (11):1341–1347, 2006.

[20] Moonseok Kim, Wonjun Choi, Youngwoon Choi, Changhyeong Yoon, and Wonshik Choi. Transmission matrix of a scattering medium and its applications in biophotonics. *Optics express*, 23 (10):12648–12668, 2015.

[21] Bahaa EA Saleh and Malvin Carl Teich. *Fundamentals of photonics, 2 volume set*. john Wiley & sons, 2019.

[22] Gediminas Račiukaitis, Evaldas Stankevičius, Paulius Gečys, Mindaugas Gedvilas, Christian Bischoff, Erwin Jäger, Udo Umhofer, and Friedemann Völklein. Laser processing by using diffractive optical laser beam shaping technique. *Journal of laser micro/nanoengineering*, 6(1), 2011.

[23] Jeremiah D Brown and David R Brown. Beam shaping with diffractive diffusers. *CRC*, pages 333–366, 2014.

[24] Gregg T Borek and David R Brown. High-performance diffractive optics for beam shaping. In *Diffractive and Holographic Technologies, Systems, and Spatial Light Modulators VI*, volume 3633, pages 51–60. SPIE, 1999.

[25] Alexander Laskin and Vadim Laskin. πshaper–refractive beam shaping optics for advanced laser technologies. In *Journal of Physics: Conference Series*, volume 276, page 012171. IOP Publishing, 2011.

[26] Alexander Laskin and Vadim Laskin. Refractive field mapping beam shaping optics: important features for a right choice. In *ICALEO 2010: 29th International Congress on Laser Materials Processing, Laser Microprocessing and Nanomanufacturing*, pages 1181–1189. AIP Publishing, 2010.

[27] August Köhler. Ein neues beleuchtungsverfahren für mikrophotographische zwecke. *Zeitschrift für wissenschaftliche Mikroskopie und für Mikroskopische Technik*, 10(4):433–440, 1893.

[28] Jeff W Lichtman and José-Angel Conchello. Fluorescence microscopy. *Nature methods*, 2(12):910–919, 2005.

[29] Zhen Song, Yuri G Anissimov, Jiangbo Zhao, Andrei V Nechaev, Annemarie Nadort, Dayong Jin, Tarl W Prow, Michael S Roberts, and Andrei V Zvyagin. Background free imaging of upconversion nanoparticle distribution in human skin. *Journal of biomedical optics*, 18(6):061215–061215, 2013.

[30] Annemarie Nadort, Varun KA Sreenivasan, Zhen Song, Ekaterina A Grebenik, Andrei V Nechaev, Vladimir A Semchishen, Vladislav Y Panchenko, and Andrei V Zvyagin. Quantitative imaging of single upconversion nanoparticles in biological tissue. *PloS one*, 8(5):e63292, 2013.

[31] Ralph J Florijn, Jan Bonnet, Hans Vrolijk, Anton K Raap, and Hans J Tanke. Effect of chromatic errors in microscopy on the visualization of multi-color fluorescence in situ hybridization. *Cytometry: The Journal of the International Society for Analytical Cytology*, 23(1):8–14, 1996.

[32] Gary R Bright, Gregory W Fisher, Jadwiga Rogowska, and D Lansing Taylor. Fluorescence ratio imaging microscopy: temporal and spatial measurements of cytoplasmic ph. *Journal of Cell Biology*, 104(4):1019–1033, 1987.

[33] Reinhard Voelkel and Kenneth J Weible. Laser beam homogenizing: limitations and constraints. In *Optical Fabrication, Testing, and Metrology III*, volume 7102, pages 222–233. SPIE, 2008.

[34] Rantsch Kurt, Bertele Ludwig, and Merz Alfred. Illuminating system, January 9 1940. US Patent 2,186,123.

[35] Frank AW Coumans, Edwin van der Pol, and Leon WMM Terstappen. Flat-top illumination profile in an epifluorescence microscope by dual microlens arrays. *Cytometry Part A*, 81(4):324–331, 2012.

[36] Ernst Abbe. Beiträge zur theorie des mikroskops und der mikroskopischen wahrnehmung. *Archiv für mikroskopische Anatomie*, 9(1):413–468, 1873.

[37] Ying Ma, Kai Wen, Min Liu, Juanjuan Zheng, Kaiqin Chu, Zachary J Smith, Lixin Liu, and Peng Gao. Recent advances in structured illumination microscopy. *Journal of Physics: Photonics*, 3(2):024009, 2021.

[38] Anne Sentenac, Kamal Belkebir, Hugues Giovannini, and Patrick C Chaumet. Subdiffraction resolution in total internal reflection fluorescence microscopy with a grating substrate. *Optics letters*, 33 (3):255–257, 2008.

[39] Reto Fiolka, Markus Beck, and Andreas Stemmer. Structured illumination in total internal reflection fluorescence microscopy using a spatial light modulator. *Optics letters*, 33(14):1629–1631, 2008.

[40] Jan T Frohn, Helmut F Knapp, and Andreas Stemmer. True optical resolution beyond the rayleigh limit achieved by standing wave illumination. *Proceedings of the National Academy of Sciences*, 97 (13):7232–7236, 2000.

[41] Julian Roth, Johanna Mehl, and Alexander Rohrbach. Fast tirf-sim imaging of dynamic, low-fluorescent biological samples. *Biomedical optics express*, 11(7):4008–4026, 2020.

[42] Olga Gliko, William E Brownell, and Peter Saggau. Fast two-dimensional standing-wave total-internal-reflection fluorescence microscopy using acousto-optic deflectors. *Optics letters*, 34(6):836–838, 2009.

[43] Mats GL Gustafsson. Nonlinear structured-illumination microscopy: wide-field fluorescence imaging with theoretically unlimited resolution. *Proceedings of the National Academy of Sciences*, 102(37):13081–13086, 2005.

[44] E Hesper Rego, Lin Shao, John J Macklin, Lukman Winoto, Göran A Johansson, Nicholas Kamps-Hughes, Michael W Davidson, and Mats GL Gustafsson. Nonlinear structured-illumination microscopy with a photoswitchable protein reveals cellular structures at 50-nm resolution. *Proceedings of the National Academy of Sciences*, 109(3):E135–E143, 2012.

[45] Krishnendu Samanta and Joby Joseph. An overview of structured illumination microscopy: recent advances and perspectives. *Journal of Optics*, 23(12):123002, 2021.

[46] Zhaojun Wang, Yanan Cai, Jia Qian, Tianyu Zhao, Yansheng Liang, Dan Dan, Ming Lei, and Baoli Yao. Hybrid multifocal structured illumination microscopy with enhanced lateral resolution and axial localization capability. *Biomedical Optics Express*, 11(6):3058–3070, 2020.

[47] Andrew G York, Sapun H Parekh, Damian Dalle Nogare, Robert S Fischer, Kelsey Temprine, Marina Mione, Ajay B Chitnis, Christian A Combs, and Hari Shroff. Resolution doubling in live, multicellular organisms via multifocal structured illumination microscopy. *Nature methods*, 9(7):749–754, 2012.

[48] Wei Zhang, Bin Yu, Danying Lin, Huanhuan Yu, Siwei Li, and Junle Qu. Optimized approach for optical sectioning enhancement in multifocal structured illumination microscopy. *Optics express*, 28(8):10919–10927, 2020.

[49] Maria Ingaramo, Andrew G York, Peter Wawrzusin, Oleg Milberg, Amy Hong, Roberto Weigert, Hari Shroff, and George H Patterson. Two-photon excitation improves multifocal structured illumination microscopy in thick scattering tissue. *Proceedings of the National Academy of Sciences*, 111(14):5254–5259, 2014.

[50] Stephan Roth, Colin JR Sheppard, Kai Wicker, and Rainer Heintzmann. Optical photon reassignment microscopy (opra). *Optical Nanoscopy*, 2:1–6, 2013.

[51] Stephan Roth and Rainer Heintzmann. Optical photon reassignment with increased axial resolution by structured illumination. *Methods and Applications in Fluorescence*, 4(4):045005, 2016.

[52] Anna Bezryadina, Junxiang Zhao, Yang Xia, Xiang Zhang, and Zhaowei Liu. High spatiotemporal resolution imaging with localized plasmonic structured illumination microscopy. *ACS nano*, 12(8): 8248–8254, 2018.

[53] Feifei Wei, Dylan Lu, Hao Shen, Weiwei Wan, Joseph Louis Ponsetto, Eric Huang, and Zhaowei Liu. Wide field super-resolution surface imaging through plasmonic structured illumination microscopy. *Nano letters*, 14(8):4634–4639, 2014.

[54] Øystein Ivar Helle, Firehun Tsige Dullo, Marcel Lahrberg, Jean-Claude Tinguely, Olav Gaute Hellesø, and Balpreet Singh Ahluwalia. Structured illumination microscopy using a photonic chip. *Nature photonics*, 14(7):431–438, 2020.

[55] Emeric Mudry, Kamal Belkebir, J Girard, Julien Savatier, Emmeran Le Moal, C Nicoletti, Marc Allain, and Anne Sentenac. Structured illumination microscopy using unknown speckle patterns. *Nature Photonics*, 6(5):312–315, 2012.

[56] JuanJuan Zheng, Xiang Fang, Kai Wen, Jiaoyue Li, Ying Ma, Min Liu, Sha An, Jianlang Li, Zeev Zalevsky, and Peng Gao. Large-field lattice structured illumination microscopy. *Optics Express*, 30(15): 27951–27966, 2022.

[57] Bo-Jui Chang, Wei-Chun Tang, Yen-Ting Liu, Yun-Chi Tsai, Chieh Tsao, Peilin Chen, and Bi-Chang Chen. Two-beam interference lattice lightsheet for structured illumination microscopy. *Journal of Physics D: Applied Physics*, 53(4):044005, 2019.

[58] Lin Shao, Peter Kner, E Hesper Rego, and Mats GL Gustafsson. Super-resolution 3d microscopy of live whole cells using structured illumination. *Nature methods*, 8(12):1044–1046, 2011.

[59] Lothar Schermelleh, Peter M Carlton, Sebastian Haase, Lin Shao, Lukman Winoto, Peter Kner, Brian Burke, M Cristina Cardoso, David A Agard, Mats GL Gustafsson, et al. Subdiffraction multicolor imaging of the nuclear periphery with 3d structured illumination microscopy. *science*, 320(5881):1332–1336, 2008.

[60] Marcel Müller, Viola Mönkemöller, Simon Hennig, Wolfgang Hübner, and Thomas Huser. Open-source image reconstruction of super-resolution structured illumination microscopy data in imagej. *Nature communications*, 7(1):10980, 2016.

[61] Amit Lal, Chunyan Shan, and Peng Xi. Structured illumination microscopy image reconstruction algorithm. *IEEE Journal of Selected Topics in Quantum Electronics*, 22(4):50–63, 2016.

[62] Graeme Ball, Justin Demmerle, Rainer Kaufmann, Ilan Davis, Ian M Dobbie, and Lothar Schermelleh. Simcheck: a toolbox for successful super-resolution structured illumination microscopy. *Scientific reports*, 5(1):15915, 2015.

[63] Pavel Křížek, Tomáš Lukeš, Martin Ovesnỳ, Karel Fliegel, and Guy M Hagen. Simtoolbox: a matlab toolbox for structured illumination fluorescence microscopy. *Bioinformatics*, 32(2):318–320, 2016.

[64] Yulun Zhang, Kunpeng Li, Kai Li, Lichen Wang, Bineng Zhong, and Yun Fu. Image super-resolution using very deep residual channel attention networks. In *Proceedings of the European conference on computer vision (ECCV)*, pages 286–301, 2018.

[65] Charles N Christensen, Edward N Ward, Meng Lu, Pietro Lio, and Clemens F Kaminski. Ml-sim: universal reconstruction of structured illumination microscopy images using transfer learning. *Biomedical optics express*, 12(5):2720–2733, 2021.

[66] Chang Ling, Chonglei Zhang, Mingqun Wang, Fanfei Meng, Luping Du, and Xiaocong Yuan. Fast structured illumination microscopy via deep learning. *Photonics Research*, 8(8):1350–1359, 2020.

[67] N Dögnitz and G Wagnieres. Determination of tissue optical properties by steady-state spatial frequency-domain reflectometry. *Lasers in medical science*, 13(1):55–65, 1998.

[68] Yuzhen Lu, Richard Li, and Renfu Lu. Gram–schmidt orthonormalization for retrieval of amplitude images under sinusoidal patterns of illumination. *Applied Optics*, 55(25):6866–6873, 2016.

[69] Yuzhen Lu, Richard Li, and Renfu Lu. Fast demodulation of pattern images by spiral phase transform in structured-illumination reflectance imaging for detection of bruises in apples. *Computers and Electronics in Agriculture*, 127:652–658, 2016.

[70] Anouk L Post, Dirk J Faber, and Ton G Van Leeuwen. Model for the diffuse reflectance in spatial frequency domain imaging. *Journal of biomedical optics*, 28(4):046002–046002, 2023.

[71] Xueming He, Xu Jiang, Xiaping Fu, Yingwang Gao, and Xiuqin Rao. Least squares support vector machine regression combined with monte carlo simulation based on the spatial frequency domain imaging for the detection of optical properties of pear. *Postharvest Biology and Technology*, 145:1–9, 2018.

[72] Tim A Erickson, Amaan Mazhar, David Cuccia, Anthony J Durkin, and James W Tunnell. Lookup-table method for imaging optical properties with structured illumination beyond the diffusion theory regime. *Journal of biomedical optics*, 15(3):036013–036013, 2010.

[73] Piotr Kijanka and Pawel Packo. Novel method for true guided waves spectral characteristics estimation using a logistic function fit and nonlinear least square algorithm. *Structural Control and Health Monitoring*, 26(9):e2388, 2019.

[74] Joseph Angelo, Christina R Vargas, Bernard T Lee, Irving J Bigio, and Sylvain Gioux. Ultrafast optical property map generation using lookup tables. *Journal of biomedical optics*, 21(11):110501–110501, 2016.

[75] Jianwen Song, Daniel L Lau, Yo-Sung Ho, and Kai Liu. Automatic look-up table based real-time phase unwrapping for phase measuring profilometry and optimal reference frequency selection. *Optics Express*, 27(9):13357–13371, 2019.

[76] Sreyankar Nandy, Ian S Hagemann, Matthew A Powell, Cary Siegel, and Quing Zhu. Quantitative multispectral ex vivo optical evaluation of human ovarian tissue using spatial frequency domain imaging. *Biomedical Optics Express*, 9(5):2451–2456, 2018.

[77] Jessie R Weber, David J Cuccia, William R Johnson, Gregory H Bearman, Anthony J Durkin, Mike Hsu, Alexander Lin, Devin K Binder, Dan Wilson, and Bruce J Tromberg. Multispectral imaging of tissue absorption and scattering using spatial frequency domain imaging and a computed-tomography imaging spectrometer. *Journal of biomedical optics*, 16(1):011015–011015, 2011.

[78] Rajinder P Singh-Moon, Darren M Roblyer, Irving J Bigio, and Shailendra Joshi. Spatial mapping of drug delivery to brain tissue using hyperspectral spatial frequency-domain imaging. *Journal of biomedical optics*, 19(9):096003–096003, 2014.

[79] Thu TA Nguyen, Jessica C Ramella-Roman, Lauren T Moffatt, Rachel T Ortiz, Marion H Jordan, and Jeffrey W Shupp. Novel

application of a spatial frequency domain imaging system to determine signature spectral differences between infected and non-infected burn wounds. *Journal of Burn Care & Research*, 34(1): 44–50, 2013.

[80] Adrien Ponticorvo, Rebecca Rowland, Melissa Baldado, David M Burmeister, Robert J Christy, Nicole P Bernal, and Anthony J Durkin. Evaluating clinical observation versus spatial frequency domain imaging (sfdi), laser speckle imaging (lsi) and thermal imaging for the assessment of burn depth. *Burns*, 45(2):450–460, 2019.

[81] Rebecca Rowland, Adrien Ponticorvo, Melissa Baldado, Gordon T Kennedy, David M Burmeister, Robert J Christy, Nicole P Bernal, and Anthony J Durkin. A simple burn wound severity assessment classifier based on spatial frequency domain imaging (sfdi) and machine learning. In *Photonics in Dermatology and Plastic Surgery 2019*, volume 10851, pages 10–20. SPIE, 2019.

[82] David M McClatchy III, Elizabeth J Rizzo, Wendy A Wells, Candice C Black, Keith D Paulsen, Stephen C Kanick, and Brian W Pogue. Light scattering measured with spatial frequency domain imaging can predict stromal versus epithelial proportions in surgically resected breast tissue. *Journal of Biomedical Optics*, 24(7): 071605–071605, 2019.

[83] Ashley M Laughney, Venkataramanan Krishnaswamy, Tyler B Rice, David J Cuccia, Richard J Barth, Bruce J Tromberg, Keith D Paulsen, Brian W Pogue, and Wendy A Wells. System analysis of spatial frequency domain imaging for quantitative mapping of surgically resected breast tissues. *Journal of biomedical optics*, 18(3): 036012–036012, 2013.

[84] Daniel J Rohrbach, Daniel Muffoletto, Jonathan Huihui, Rolf Saager, Kenneth Keymel, Anne Paquette, Janet Morgan, Nathalie Zeitouni, and Ulas Sunar. Preoperative mapping of nonmelanoma skin cancer using spatial frequency domain and ultrasound imaging. *Academic radiology*, 21(2):263–270, 2014.

[85] Xinlin Chen, Weihao Lin, Chenge Wang, Shaoheng Chen, Jing Sheng, Bixin Zeng, and Min Xu. In vivo real-time imaging of cutaneous hemoglobin concentration, oxygen saturation, scattering properties, melanin content, and epidermal thickness with visible spatially modulated light. *Biomedical optics express*, 8(12):5468–5482, 2017.

[86] Jeffrey B Travers, Chien Poon, Daniel J Rohrbach, Nathan M Weir, Elizabeth Cates, Faye Hager, and Ulas Sunar. Noninvasive mesoscopic imaging of actinic skin damage using spatial frequency domain imaging. *Biomedical Optics Express*, 8(6):3045–3052, 2017.

[87] Amr Yafi, Fuad K Muakkassa, Tejasvi Pasupneti, Judy Fulton, David J Cuccia, Amaan Mazhar, Kimberly N Blasiole, and Eliot N Mostow. Quantitative skin assessment using spatial frequency domain imaging (sfdi) in patients with or at high risk for pressure ulcers. *Lasers in surgery and medicine*, 49(9):827–834, 2017.

[88] Christina R Vargas, John T Nguyen, Yoshitomo Ashitate, Joseph Angelo, Vivek Venugopal, Frank Kettenring, Florin Neacsu, John V Frangioni, Sylvain Gioux, and Bernard T Lee. Intraoperative hemifacial composite flap perfusion assessment using spatial frequency domain imaging: a pilot study in preparation for facial transplantation. *Annals of plastic surgery*, 76(2):249–255, 2016.

[89] John T Nguyen, Samuel J Lin, Adam M Tobias, Sylvain Gioux, Amaan Mazhar, David J Cuccia, Yoshitomo Ashitate, Alan Stockdale, Rafiou Oketokoun, Nicholas J Durr, et al. A novel pilot study using spatial frequency domain imaging to assess oxygenation of perforator flaps during reconstructive breast surgery. *Annals of plastic surgery*, 71(3):308–315, 2013.

[90] Alexander J Lin, Maya A Koike, Kim N Green, Jae G Kim, Amaan Mazhar, Tyler B Rice, Frank M LaFerla, and Bruce J Tromberg. Spatial frequency domain imaging of intrinsic optical property contrast in a mouse model of alzheimer's disease. *Annals of biomedical engineering*, 39:1349–1357, 2011.

[91] Alexander J Lin, Nicholas A Castello, Grace Lee, Kim N Green, Anthony J Durkin, Bernard Choi, Frank LaFerla, and Bruce J Tromberg. In vivo optical signatures of neuronal death in a mouse model of alzheimer's disease. *Lasers in surgery and medicine*, 46 (1):27–33, 2014.

[92] Amaan Mazhar, David J Cuccia, Sylvain Gioux, Anthony J Durkin, John V Frangioni, and Bruce J Tromberg. Structured illumination enhances resolution and contrast in thick tissue fluorescence imaging. *Journal of biomedical optics*, 15(1):010506–010506, 2010.

[93] Bin Yang, Manu Sharma, and James W Tunnell. Attenuation-corrected fluorescence extraction for image-guided surgery in spatial frequency domain. *Journal of biomedical optics*, 18(8):080503–080503, 2013.

[94] Jessica Sun, Jessica P Miller, Deep Hathi, Haiying Zhou, Samuel Achilefu, Monica Shokeen, and Walter J Akers. Enhancing in vivo tumor boundary delineation with structured illumination fluorescence molecular imaging and spatial gradient mapping. *Journal of biomedical optics*, 21(8):080502–080502, 2016.

[95] Sergey Alexandrov, Paul M McNamara, Nandan Das, Yi Zhou, Gillian Lynch, Josh Hogan, and Martin Leahy. Spatial frequency domain correlation mapping optical coherence tomography for nanoscale structural characterization. *Applied Physics Letters*, 115 (12), 2019.

[96] David M Burmeister, Adrien Ponticorvo, Bruce Yang, Sandra C Becerra, Bernard Choi, Anthony J Durkin, and Robert J Christy. Utility of spatial frequency domain imaging (sfdi) and laser speckle imaging (lsi) to non-invasively diagnose burn depth in a porcine model. *Burns*, 41(6):1242–1252, 2015.

[97] Adrien Ponticorvo, David M Burmeister, Bruce Yang, Bernard Choi, Robert J Christy, and Anthony J Durkin. Quantitative assessment of graded burn wounds in a porcine model using spatial frequency domain imaging (sfdi) and laser speckle imaging (lsi). *Biomedical optics express*, 5(10):3467–3481, 2014.

[98] Thomas A Klar and Stefan W Hell. Subdiffraction resolution in far-field fluorescence microscopy. *Optics letters*, 24(14):954–956, 1999.

[99] Thomas A Klar, Stefan Jakobs, Marcus Dyba, Alexander Egner, and Stefan W Hell. Fluorescence microscopy with diffraction resolution barrier broken by stimulated emission. *Proceedings of the National Academy of Sciences*, 97(15):8206–8210, 2000.

[100] Suhui Deng, Li Liu, Ya Cheng, Ruxin Li, and Zhizhan Xu. Effects of primary aberrations on the fluorescence depletion patterns of sted microscopy. *Optics express*, 18(2):1657–1666, 2010.

[101] Suhui Deng, Li Liu, Ya Cheng, Ruxin Li, and Zhizhan Xu. Investigation of the influence of the aberration induced by a plane interface on sted microscopy. *Optics express*, 17(3):1714–1725, 2009.

[102] Martin Booth, Débora Andrade, Daniel Burke, Brian Patton, and Mantas Zurauskas. Aberrations and adaptive optics in super-resolution microscopy. *Microscopy*, 64(4):251–261, 2015.

[103] Egidijus Auksorius, Bosanta R Boruah, Christopher Dunsby, Peter MP Lanigan, Gordon Kennedy, Mark AA Neil, and Paul MW French. Stimulated emission depletion microscopy with a supercontinuum source and fluorescence lifetime imaging. *Optics letters*, 33(2):113–115, 2008.

[104] Yiye Zhang, Chenxue Wu, Yanchun Song, Ke Si, Yao Zheng, Lejia Hu, Jiajia Chen, Limin Tang, and Wei Gong. Machine learning based adaptive optics for doughnut-shaped beam. *Optics express*, 27(12):16871–16881, 2019.

[105] Mary Grace M Velasco, Mengyang Zhang, Jacopo Antonello, Peng Yuan, Edward S Allgeyer, Dennis May, Ons M'Saad, Phylicia Kidd, Andrew ES Barentine, Valentina Greco, et al. 3d super-resolution deep-tissue imaging in living mice. *Optica*, 8(4):442–450, 2021.

[106] Gerald Donnert, Jan Keller, Rebecca Medda, M Alexandra Andrei, Silvio O Rizzoli, Reinhard Lührmann, Reinhard Jahn, Christian Eggeling, and Stefan W Hell. Macromolecular-scale resolution in biological fluorescence microscopy. *Proceedings of the National Academy of Sciences*, 103(31):11440–11445, 2006.

[107] Michael Weber, Marcel Leutenegger, Stefan Stoldt, Stefan Jakobs, Tiberiu S Mihaila, Alexey N Butkevich, and Stefan W Hell. Minsted fluorescence localization and nanoscopy. *Nature photonics*, 15 (5):361–366, 2021.

[108] J Chance Carter, S Michael Angel, Marion Lawrence-Snyder, Jon Scaffidi, Richard E Whipple, and John G Reynolds. Standoff detection of high explosive materials at 50 meters in ambient light conditions using a small raman instrument. *Applied Spectroscopy*, 59(6):769–775, 2005.

[109] Fay Nicolson, Lauren E Jamieson, Samuel Mabbott, Neil C Shand, Duncan Graham, and Karen Faulds. Through barrier detection of ethanol using handheld raman spectroscopy—conventional raman versus spatially offset raman spectroscopy (sors). *Journal of Raman Spectroscopy*, 48(12):1828–1838, 2017.

[110] Charlotte Eliasson and Pavel Matousek. Noninvasive authentication of pharmaceutical products through packaging using spatially offset raman spectroscopy. *Analytical Chemistry*, 79(4):1696–1701, 2007.

[111] Pavel Matousek, Ian P Clark, Edward RC Draper, MD Morris, AE Goodship, N Everall, M Towrie, WF Finney, and AW Parker. Subsurface probing in diffusely scattering media using spatially offset raman spectroscopy. *Applied spectroscopy*, 59(4):393–400, 2005.

[112] Pavel Matousek, Edward RC Draper, Allen E Goodship, Ian P Clark, Kate L Ronayne, and Anthony W Parker. Noninvasive raman spectroscopy of human tissue in vivo. *Applied spectroscopy*, 60(7):758–763, 2006.

[113] Khan Mohd Khan, Surjendu B Dutta, Nitin Kumar, Anita Dalal, Amrita Srivastava, Hemant Krishna, and Shovan K Majumder. Inverse spatially-offset raman spectroscopy using optical fibers: An axicon lens-free approach. *Journal of Biophotonics*, 12(11): e201900140, 2019.

[114] Matthew V Schulmerich, Kathryn A Dooley, Michael D Morris, Thomas M Vanasse, and Steven A Goldstein. Transcutaneous fiber optic raman spectroscopy of bone using annular illumination and a circular array of collection fibers. *Journal of biomedical optics*, 11 (6):060502–060502, 2006.

[115] Ren A Odion, Pietro Strobbia, Bridget M Crawford, and Tuan Vo-Dinh. Inverse surface-enhanced spatially offset raman spectroscopy (sesors) through a monkey skull. *Journal of Raman Spectroscopy*, 49(9):1452–1460, 2018.

[116] Ivo M Vellekoop and Allard P Mosk. Focusing coherent light through opaque strongly scattering media. *Optics letters*, 32(16): 2309–2311, 2007.

[117] Sébastien M Popoff, Geoffroy Lerosey, Rémi Carminati, Mathias Fink, Albert Claude Boccara, and Sylvain Gigan. Measuring the transmission matrix in optics: An approach to the study and control format of light propagation in disordered media. *Physical review letters*, 104(10):100601, 2010.

[118] Sébastien M Popoff, Geoffroy Lerosey, Mathias Fink, Albert Claude Boccara, and Sylvain Gigan. Controlling light through optical disordered media: transmission matrix approach. *New Journal of Physics*, 13(12):123021, 2011.

[119] Allard P Mosk, Ad Lagendijk, Geoffroy Lerosey, and Mathias Fink. Controlling waves in space and time for imaging and focusing in complex media. *Nature photonics*, 6(5):283–292, 2012.

[120] Shachar Resisi, Yehonatan Viernik, Sebastien M Popoff, and Yaron Bromberg. Wavefront shaping in multimode fibers by transmission matrix engineering. *APL Photonics*, 5(3), 2020.

[121] Navid Borhani, Eirini Kakkava, Christophe Moser, and Demetri Psaltis. Learning to see through multimode fibers. *Optica*, 5(8): 960–966, 2018.

[122] Alex Turpin, Ivan Vishniakou, and Johannes D Seelig. Light scattering control in transmission and reflection with neural networks. *Optics express*, 26(23):30911–30929, 2018.

[123] Babak Rahmani, Damien Loterie, Georgia Konstantinou, Demetri Psaltis, and Christophe Moser. Multimode optical fiber transmission with a deep learning network. *Light: science & applications*, 7(1):69, 2018.

[124] Angélique Drémeau, Antoine Liutkus, David Martina, Ori Katz, Christophe Schülke, Florent Krzakala, Sylvain Gigan, and Laurent Daudet. Reference-less measurement of the transmission matrix of a highly scattering material using a dmd and phase retrieval techniques. *Optics express*, 23(9):11898–11911, 2015.

[125] Tianrui Zhao, Sebastien Ourselin, Tom Vercauteren, and Wenfeng Xia. Seeing through multimode fibers with real-valued intensity transmission matrices. *Optics express*, 28(14):20978–20991, 2020.

[126] Youngwoon Choi, Changhyeong Yoon, Moonseok Kim, Taeseok Daniel Yang, Christopher Fang-Yen, Ramachandra R Dasari, Kyoung Jin Lee, and Wonshik Choi. Scanner-free and wide-field endoscopic imaging by using a single multimode optical fiber. *Physical review letters*, 109(20):203901, 2012.

[127] Shay Ohayon, Antonio Caravaca-Aguirre, Rafael Piestun, and James J DiCarlo. Minimally invasive multimode optical fiber microendoscope for deep brain fluorescence imaging. *Biomedical optics express*, 9(4):1492–1509, 2018.

[128] Sergey Turtaev, Ivo T Leite, Tristan Altwegg-Boussac, Janelle MP Pakan, Nathalie L Rochefort, and Tomáš Čižmár. High-fidelity multimode fibre-based endoscopy for deep brain in vivo imaging. *Light: Science & Applications*, 7(1):92, 2018.

[129] Georgia Konstantinou, Antoine Boniface, Damien Loterie, Eirini Kakkava, Demetri Psaltis, and Christophe Moser. Improved two-photon polymerization through an optical fiber using coherent beam shaping. *Optics and Lasers in Engineering*, 160:107232, 2023.

[130] Tomáš Čižmár and Kishan Dholakia. Shaping the light transmission through a multimode optical fibre: complex transformation analysis and applications in biophotonics. *Optics express*, 19(20): 18871–18884, 2011.

[131] Silvio Bianchi and Roberto Di Leonardo. A multi-mode fiber probe for holographic micromanipulation and microscopy. *Lab on a Chip*, 12(3):635–639, 2012.

[132] Hyeonseung Yu, Timothy R Hillman, Wonshik Choi, Ji Oon Lee, Michael S Feld, Ramachandra R Dasari, and YongKeun Park. Measuring large optical transmission matrices of disordered media. *Physical review letters*, 111(15):153902, 2013.

[133] Guanying Chen, Hailong Qiu, Paras N Prasad, and Xiaoyuan Chen. Upconversion nanoparticles: design, nanochemistry, and applications in theranostics. *Chemical reviews*, 114(10):5161–5214, 2014.

[134] François Auzel. Upconversion and anti-stokes processes with f and d ions in solids. *Chemical reviews*, 104(1):139–174, 2004.

[135] Can T Xu, Qiuqiang Zhan, Haichun Liu, Gabriel Somesfalean, Jun Qian, Sailing He, and Stefan Andersson-Engels. Upconverting nanoparticles for pre-clinical diffuse optical imaging, microscopy and sensing: Current trends and future challenges. *Laser & Photonics Reviews*, 7(5):663–697, 2013.

[136] Markus Haase and Helmut Schäfer. Upconverting nanoparticles. *Angewandte Chemie International Edition*, 50(26):5808–5829, 2011.

[137] Aruna Ivaturi, Sean KW MacDougall, Rosa Martín-Rodríguez, Marta Quintanilla, Jose Marques-Hueso, Karl W Krämer, Andries Meijerink, and Bryce S Richards. Optimizing infrared to near infrared upconversion quantum yield of β-nayf4: Er3+ in fluoropolymer matrix for photovoltaic devices. *Journal of applied physics*, 114(1), 2013.

[138] Yong Li, Xiantao Wei, and Min Yin. Synthesis and upconversion luminescent properties of er3+ doped and er3+–yb3+ codoped gdocl powders. *Journal of alloys and compounds*, 509(41):9865–9868, 2011.

[139] Genevieve Mialon, Silvan Turkcan, Geraldine Dantelle, Daniel P Collins, Maria Hadjipanayi, Robert A Taylor, Thierry Gacoin, Antigoni Alexandrou, and Jean-Pierre Boilot. High up-conversion efficiency of yvo4: Yb, er nanoparticles in water down to the single-particle level. *The Journal of Physical Chemistry C*, 114(51):22449–22454, 2010.

[140] Marylyn S Arai and Andrea SS de Camargo. Exploring the use of upconversion nanoparticles in chemical and biological sensors: from surface modifications to point-of-care devices. *Nanoscale Advances*, 3(18):5135–5165, 2021.

[141] Shihui Wen, Jiajia Zhou, Kezhi Zheng, Artur Bednarkiewicz, Xiaogang Liu, and Dayong Jin. Advances in highly doped upconversion nanoparticles. *Nature communications*, 9(1):2415, 2018.

[142] Guanying Chen, Haichun Liu, Gabriel Somesfalean, Huijuan Liang, and Zhiguo Zhang. Upconversion emission tuning from green to red inyb3+/ho3+-codopednayf4 nanocrystals bytridoping with ce3+ ions. *Nanotechnology*, 20(38):385704, 2009.

[143] Qiuqiang Zhan, Jun Qian, Huijuan Liang, Gabriel Somesfalean, Dan Wang, Sailing He, Zhiguo Zhang, and Stefan Andersson-Engels. Using 915 nm laser excited tm3+/er3+/ho3+-doped naybf4 upconversion nanoparticles for in vitro and deeper in vivo bioimaging without overheating irradiation. *ACS nano*, 5(5):3744–3757, 2011.

[144] Meng Wang, Cong-Cong Mi, Wen-Xing Wang, Cui-Hong Liu, Ying-Fan Wu, Zhang-Run Xu, Chuan-Bin Mao, and Shu-Kun Xu. Immunolabeling and nir-excited fluorescent imaging of hela cells by using nayf4: Yb, er upconversion nanoparticles. *ACS nano*, 3(6): 1580–1586, 2009.

[145] Liqin Xiong, Zhigang Chen, Qiwei Tian, Tianye Cao, Congjian Xu, and Fuyou Li. High contrast upconversion luminescence targeted imaging in vivo using peptide-labeled nanophosphors. *Analytical chemistry*, 81(21):8687–8694, 2009.

[146] Ewen Smith and Geoffrey Dent. *Modern Raman spectroscopy: a practical approach*. John Wiley & Sons, 2019.

[147] Caroline Boudoux. *Fundamentals of biomedical optics*. Blurb, 2017.

[148] David Tuschel. Raman thermometry: Understanding the mathematics to better design raman measurements. 2019.

[149] Abigail S Haka, Zoya Volynskaya, Joseph A Gardecki, Jon Nazemi, Robert Shenk, Nancy Wang, Ramachandra R Dasari, Maryann Fitzmaurice, and Michael S Feld. Diagnosing breast cancer using raman spectroscopy: prospective analysis. *Journal of biomedical optics*, 14(5):054023–054023, 2009.

[150] Christine M O'Brien, Jennifer L Herington, Naoko Brown, Isaac J Pence, Bibhash C Paria, James C Slaughter, Jeff Reese, and Anita Mahadevan-Jansen. In vivo raman spectral analysis of impaired cervical remodeling in a mouse model of delayed parturition. *Scientific reports*, 7(1):6835, 2017.

[151] Mustafa Unal and Ozan Akkus. Raman spectral classification of mineral-and collagen-bound water's associations to elastic and post-yield mechanical properties of cortical bone. *Bone*, 81:315–326, 2015.

[152] Michelle Janssens, Jeroen van Smeden, GJ Puppels, APM Lavrijsen, PJ Caspers, and JA Bouwstra. Lipid to protein ratio plays an important role in the skin barrier function in patients with atopic eczema. *British Journal of Dermatology*, 170(6):1248–1255, 2014.

[153] Sara Mosca, Claudia Conti, Nick Stone, and Pavel Matousek. Spatially offset raman spectroscopy. *Nature Reviews Methods Primers*, 1(1):21, 2021.

[154] Laura E Masson, Christine M O'Brien, Isaac J Pence, Jennifer L Herington, Jeff Reese, Ton G Van Leeuwen, and Anita Mahadevan-Jansen. Dual excitation wavelength system for combined fingerprint and high wavenumber raman spectroscopy. *Analyst*, 143(24): 6049–6060, 2018.

[155] Steven L Jacques. Optical properties of biological tissues: a review. *Physics in Medicine & Biology*, 58(11):R37, 2013.

[156] Donald F Swinehart. The beer-lambert law. *Journal of chemical education*, 39(7):333, 1962.

[157] David T Delpy, Mark Cope, Pieter van der Zee, Simon Arridge, Susan Wray, and JS Wyatt. Estimation of optical pathlength through tissue from direct time of flight measurement. *Physics in Medicine & Biology*, 33(12):1433, 1988.

[158] Michael S Patterson, Britton Chance, and Brian C Wilson. Time resolved reflectance and transmittance for the noninvasive measurement of tissue optical properties. *Applied optics*, 28(12):2331–2336, 1989.

[159] Edward D Chan, Michael M Chan, and Mallory M Chan. Pulse oximetry: understanding its basic principles facilitates appreciation of its limitations. *Respiratory medicine*, 107(6):789–799, 2013.

[160] Meir Nitzan, Ayal Romem, and Robert Koppel. Pulse oximetry: fundamentals and technology update. *Medical Devices: Evidence and Research*, pages 231–239, 2014.

[161] Nicholas Metropolis and Stanislaw Ulam. The monte carlo method. *Journal of the American statistical association*, 44(247):335–341, 1949.

[162] Lihong Wang, Steven L Jacques, and Liqiong Zheng. Mcml—monte carlo modeling of light transport in multi-layered tissues. *Computer methods and programs in biomedicine*, 47(2):131–146, 1995.

[163] Qianqian Fang and David A Boas. Monte carlo simulation of photon migration in 3d turbid media accelerated by graphics processing units. *Optics express*, 17(22):20178–20190, 2009.

[164] Siddra Maryam, Sanathana Konugolu Venkata Sekar, M. Daniyal Ghauri, Edward Fahy, Marcelo Saito Nogueira, Huihui Lu, Flavien Beffara, Georges Humbert, Richeal Ni Riordain, Patrick Sheahan, Ray Burke, Kiang Wei Kho, Rekha Gautam, and Stefan Andersson-Engels. Mobile multi-configuration clinical translational raman system for oral cancer application. *Analyst*, 148:1514–1523, 2023. doi: 10.1039/D2AN01921C. URL http://dx.doi.org/10.1039/D2AN01921C.

[165] Scott Prahl. Tissue phantoms. https://omlc.org/~prahl/projects/phantoms.html, n.d. URL https://omlc.org/~prahl/projects/phantoms.html. Accessed: 27 July 2025.

[166] Martha Z Vardaki and Nikolaos Kourkoumelis. Tissue phantoms for biomedical applications in raman spectroscopy: a review. *Biomedical engineering and computational biology*, 11:1179597220948100, 2020.

[167] Lindokuhle Ntombela, Bamise Adeleye, and Naven Chetty. Low-cost fabrication of optical tissue phantoms for use in biomedical imaging. *Heliyon*, 6(3), 2020.

[168] Brian W Pogue and Michael S Patterson. Review of tissue simulating phantoms for optical spectroscopy, imaging and dosimetry. *Journal of biomedical optics*, 11(4):041102–041102, 2006.

[169] Sanathana Konugolu Venkata Sekar, Andrea Pacheco, Pierluigi Martella, Haiyang Li, Pranav Lanka, Antonio Pifferi, and Stefan Andersson-Engels. Solid phantom recipe for diffuse optics in biophotonics applications: a step towards anatomically correct 3d tissue phantoms. *Biomedical optics express*, 10(4):2090–2100, 2019.

[170] Crystal D Karakochuk, Sonja Y Hess, Denish Moorthy, Sorrel Namaste, Megan E Parker, Aviva I Rappaport, Rita Wegmüller, Omar Dary, and HEmoglobin MEasurement (HEME) Working Group. Measurement and interpretation of hemoglobin concentration in clinical and field settings: a narrative review. *Annals of the new York Academy of Sciences*, 1450(1):126–146, 2019.

[171] Gyeongsil Lee, Seulggie Choi, Kyuwoong Kim, Jae-Moon Yun, Joung Sik Son, Su-Min Jeong, Sung Min Kim, and Sang Min Park. Association of hemoglobin concentration and its change with cardiovascular and all-cause mortality. *Journal of the American Heart Association*, 7(3):e007723, 2018.

[172] Sun-Kyung Park, Chahnmee Hur, Young-Won Kim, Seokha Yoo, Young-Jin Lim, and Jin-Tae Kim. Noninvasive hemoglobin monitoring for maintaining hemoglobin concentration within the target range during major noncardiac surgery: A randomized controlled trial. *Journal of Clinical Anesthesia*, 93:111326, 2024.

[173] Jens Kraitl, D Klinger, D Fricke, U Timm, and H Ewald. Non-invasive measurement of blood components: sensors for an in-vivo haemoglobin measurement. In *Advancement in Sensing Technology: New Developments and Practical Applications*, pages 237–262. Springer, 2013.

[174] José AL Calbet, Carsten Lundby, Maria Koskolou, and Robert Boushel. Importance of hemoglobin concentration to exercise: acute manipulations. *Respiratory physiology & neurobiology*, 151 (2-3):132–140, 2006.

[175] Lynnette M Neufeld, Leila M Larson, Anura Kurpad, Sheila Mburu, Reynaldo Martorell, and Kenneth H Brown. Hemoglobin concentration and anemia diagnosis in venous and capillary blood: biological basis and policy implications. *Annals of the new York Academy of Sciences*, 1450(1):172–189, 2019.

[176] Edward L Hull, Michael G Nichols, and Thomas H Foster. Quantitative broadband near-infrared spectroscopy of tissue-simulating phantoms containing erythrocytes. *Physics in Medicine & Biology*, 43(11):3381, 1998.

[177] Troy O McBride, Brian W Pogue, Ellen D Gerety, Steven B Poplack, Ulf L Österberg, and Keith D Paulsen. Spectroscopic diffuse optical tomography for the quantitative assessment of hemoglobin concentration and oxygen saturation in breast tissue. *Applied optics*, 38(25):5480–5490, 1999.

[178] Peck H Koh, Clare E Elwell, and David T Delpy. Development of a dynamic test phantom for optical topography. *Adv. Exp. Med. Biol*, 645:141–146, 2009.

[179] Tsukasa Funane, Hirokazu Atsumori, Masashi Kiguchi, Yukari Tanikawa, and Eiji Okada. Dynamic phantom with two stage-driven absorbers for mimicking hemoglobin changes in superficial and deep tissues. *Journal of biomedical optics*, 17(4):047001–047001, 2012.

[180] Jeremy C Hebden, Joanna Brunker, Teresa Correia, Ben D Price, Adam P Gibson, and NL Everdell. An electrically-activated dynamic tissue-equivalent phantom for assessment of diffuse optical imaging systems. *Physics in Medicine & Biology*, 53(2):329, 2007.

[181] Ali I Siam, Fathi Abd El-Samie, Atef Abu Elazm, Nirmeen El-Bahnasawy, and Ghada Elbanby. Real-world ppg dataset. https://doi.org/10.17632/yynb8t9x3d.3, 2022.

[182] Julian Bailes. Photostability of semiconductor quantum dots in response to uv exposure. In *Nanoparticles in Biology and Medicine: Methods and Protocols*, pages 343–349. Springer, 2020.

[183] Pavel Matousek, MD Morris, N Everall, IP Clark, M Towrie, E Draper, A Goodship, and AW Parker. Numerical simulations of subsurface probing in diffusely scattering media using spatially offset raman spectroscopy. *Applied spectroscopy*, 59(12):1485–1492, 2005.

[184] Jason R Maher and Andrew J Berger. Determination of ideal offset for spatially offset raman spectroscopy. *Applied spectroscopy*, 64(1):61–65, 2010.

Appendix

HIGH CONTRAST BREAST CANCER BIOMARKER SEMI-QUANTIFICATION AND IMMUNOHISTOCHEMISTRY IMAGING USING UPCONVERTING NANOPARTICLES

Supplementary Material (S1)

Formalin-fixed paraffin-embedded samples were sectioned in 4 µm thin slices on a microtome (Microm HM-360, Marshall Scientific, USA). The sections were placed on SuperFrost™ Plus microscope slides (HistoLab, Sweden). Dewaxing was performed by immersing the samples 2× for 5 min in Xylene followed by rehydration in 2× 5 min absolute ethanol, 5 min 96% ethanol, 5 min 70% ethanol, and 5 min in distilled H2O. For heat-induced antigen retrieval (HIER), the slides were transferred into a container with antigen-retrieval buffer (250 mL, EnVision FLEX high pH, Agilent, USA) that was pre-heated (95 °C) in a water bath. The HIER was conducted for 20 min at 95 °C. The container was removed from the water bath and allowed to cool down for 20 min.

The following steps were conducted at room temperature. Depending on the size of the sections 150–350 µL of the reagents were necessary to sufficiently cover the samples. The slides were transferred into a container with Tris-buffered saline containing 1 mM sodium fluoride (TBSF). Samples that were counterstained with hematoxylin were immersed in Mayer's Hematoxylin for 3 min followed by washing in TBSF (2× 1 min). Sections used for labelling with antibody-horseradish-peroxidase (HRP) conjugates were quenched with 0.3% H2O2 in TBSF for 10 min followed by a washing step in TBSF. All sections were encircled with a liquid blocker (ImmEdge Pen, Vector Laboratories, USA) and transferred to a Coplin jar with TBSF. The blocking buffer was applied to each section and incubated for 45 min followed by washing in TBSF for 1 min.

UCNP Labelling

For UCNP labellings, endogenous biotin was blocked using a ready-to-use streptavidin solution (20 min, SP-2002, Vector Laboratories) followed by a biotin solution (20 min, SP-2002, Vector Laboratories). Non-specific binding sites were blocked using TBSF containing 10% SuperBlock (37535, ThermoFisher Scientific) The slides were washed 2× for 1 min in TBSF after each blocking step.

The primary anti-HER2 antibody (A0485, Agilent) was diluted to 1 µg/mL in dilution buffer (TBSF + 0.05% Tween20, 10% SuperBlock) added to the sections, and incubated for 60 min. Negative controls were incubated with dilution buffer without the primary antibody. The slides were washed 2× 1 min with TBSF.

Slides for traditional IHC labelling (HRP/DAB) were incubated with a ready-to-use anti-rabbit secondary antibody-HRP conjugate (ImmPress® HRP Goat Anti-Rabbit IgG Polymer Detection Kit Peroxidase, Vector Laboratories) for 45 min and washed 3× 1 min with TBSF. For the DAB reaction, one droplet of the DAB substrate per milliliter substrate buffer (EnVision Flex Mini Kit, High pH, Agilent) was prepared. The antibody-HRP labelled slides were incubated for 10 min with substrate dilution and washed 3×1 min with TBSF. The DAB slides were then dehydrated by immersing them subsequently for 3× 1 min in 70% ethanol, 96% ethanol, and absolute ethanol, and at the end in Xylene for 5 min. Mounting of the coverslip was performed with Pertex as a mounting medium.

Slides for UCNP labelling were incubated with 2 µg/mL biotinylated anti-rabbit secondary antibody in dilution buffer (711-005-152, Jackson Immunoresearch, USA) for 60 min. The slides were washed 2× 1 min with TBSF and incubated for 45 min with a UCNP-streptavidin conjugate (SCIZYS reagent, Lumito, Sweden) in dilution buffer. After 3× washing for 1 min in TBSF, the slides were mounted with an aqueous mounting medium (Fluoroshield™, Sigma

Aldrich). Slides counterstained with DAPI were instead mounted with a DAPI-containing mounting medium (ab104139, Abcam, UK).

A Köhler reflected light illumination and imaging microscope system was employed to image the UCNPs labelled samples. A collimated 976nm laser (dst11-t193-h2o, Ostech) beam passed through two identical microlens arrays (10 x 10mm, 500µm Pitch, 1.2° Divergence, Edmund Optics), and then was magnified by a telescope system (LB1779-B, LB1676-B, Thorlabs). After that, the beam was focused by the objective lens (20X Nikon CFI60 TU Plan Epi ELWD, Nikon) of the microscope to form a 725x725 µm spot to illuminate the sample. The anti-Stokes emission from UCNPs was filtered by a 950 nm short-pass filter (FF01-950/SP-25, Semrock) to block the reflected laser light.

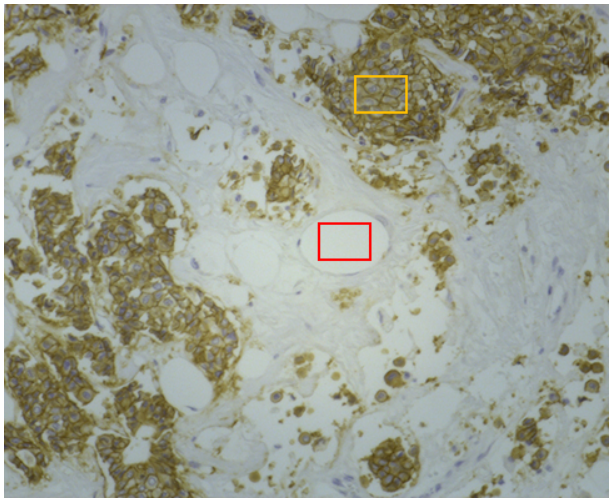

Fig. S1. DAB labeled HER2 3+ breast cancer image with DAB signal (yellow box) and background area indicated with a red box.

The signal-to-background for DAB was calculated by taking the ratio of average background with no labeling (red box in Sup.Fig.1) to DAB (yellow box in Fig. S1.) labeled section of breast cancer image. To perform the calculation, the signal was averaged across RGB pixels and the signal-to-background for DAB was found to be 1.6.

Supplementary Materials for:

Raman Spectroscopy based framework for In-vivo Assessment of Bone Composition

Hui Ma[1,2,*], Pranav Lanka[1], Suraj Kumar Kothuri[1,2], Baptiste Jayet[1], Anita Mahadevan Jansen[3], Stefan Andersson-Engels[1,4,5], Sanathana Konugolu Venkata Sekar[1,4,5], and Rekha Gautam[1,*]

[1] Biophotonics@Tyndall, Cork, Ireland

[2] Engineering Science, University College Cork, Cork, Ireland

[3] Vanderbilt Biophotonics Center, Vanderbilt University, Nashville, TN, USA

[4] School of Physics, University College Cork, Cork, Ireland

[5] BioPixS Ltd, Cork, Ireland

* hui.ma@tyndall.ie and rekha.gautam@tyndall.ie

Table S1 Laser power for different ring sizes (offset) keeping the overall power below MPE for both 730 nm and 830 nm. Laser power for different ring sizes (offset) keeping the overall power below MPE for both 730 nm (0.23 W/cm^2) and 830 nm (0.36 W/cm^2) according to the American national standard for safe use of lasers (ANSI Z136.1) [1]

Offset in mm	Laser power (mW)	
	730 nm	830nm
3	43.3	68.6
5	72.1	114
7	101	160
9	130	206
11	159	252
MPE	230 mW/cm^2	360 mW/cm^2

Table S2 ENR values for all ten participants at different spatial offsets.

Spatial Offset(mm)	M1	M2	M3	M4	M5	F1	F2	F3	F4	F5
0	9.32	6.02	5.53	7.13	7.18	4.25	4.34	4.11	5.57	4.03
3	75.8	34.2	26.4	34.3	41.2	42.8	55.8	25.9	43.5	32.4
5	85.2	43.3	38.1	80.6	19.1	44.3	50.8	37.7	73.2	66.5
7	121	35.9	57.1	62.3	89.4	77.8	70.9	52.2	58.3	83.1
9	56.6	17.0	37.7	46.5	8.96	61.3	67.0	44.8	74.0	58.6
11	18.1	16.1	24.8	70.9	10.4	48.1	52.7	33.8	53.4	47.5

Table S3 Ultrasound measured tissue (US-Tissue) thickness and maximum (Max) enhancement-to-noise ratio (ENR): Ideal offset for participants.

Participants	US-Tissue median thickness (mm)	Max. ENR: Ideal offset (mm)
P1	5.02	7
P2	4.20	5
P3	5.34	7
P4	5.14	7
P5	14.9	9
P6	4.85	7
P7	8.69	7
P8	9.46	7
P9	4.84	5
P10	4.92	7

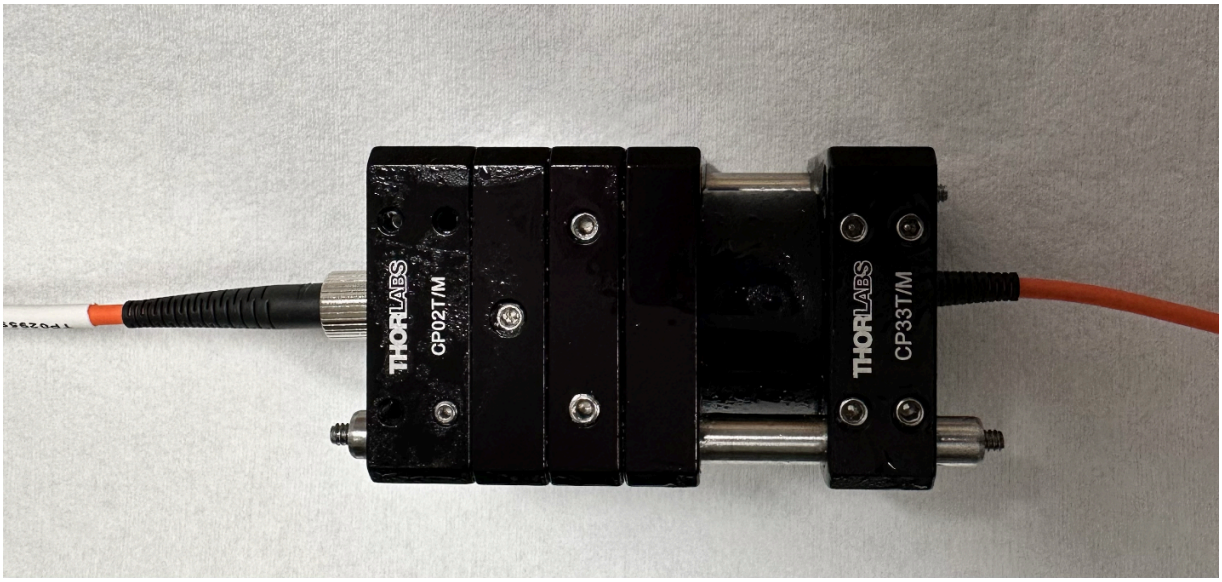

Figure S1 Sample holder for transmission mode time of flight measurements

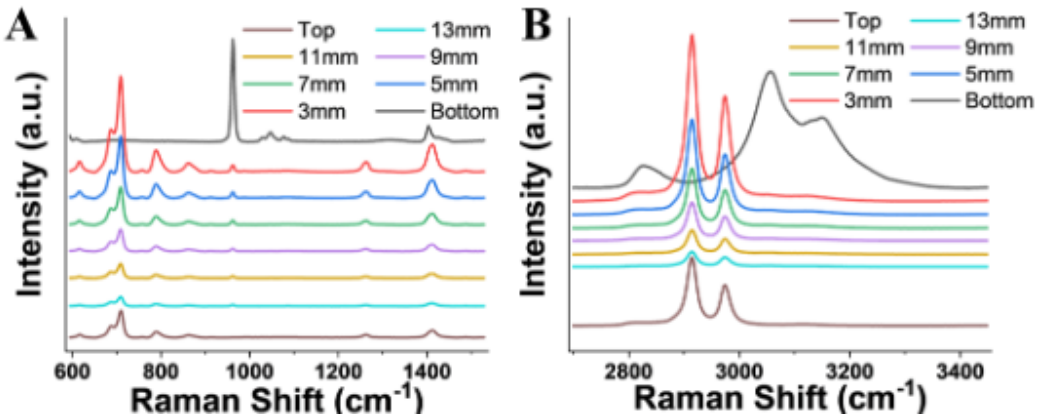

Figure S2 Raman spectra with a 5mm top layer at different offsets for (A) fingerprint region and (B) high wavenumber region. The spectra are baseline corrected but not normalised.

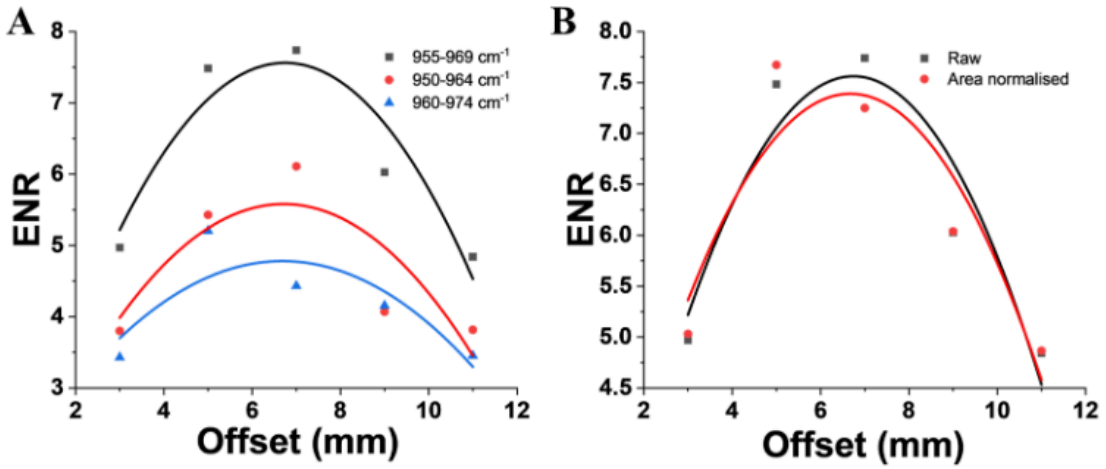

Figure S3 Evaluation of the robustness of the ENR metric to analysis parameters: (A) effect of shifting the bottom-layer peak integration window for the 961 cm^{-1} band by ±5 cm^{-1}, and (B) effect of applying global area normalization. In both cases, the optimal spatial offset varied by less than 10%.

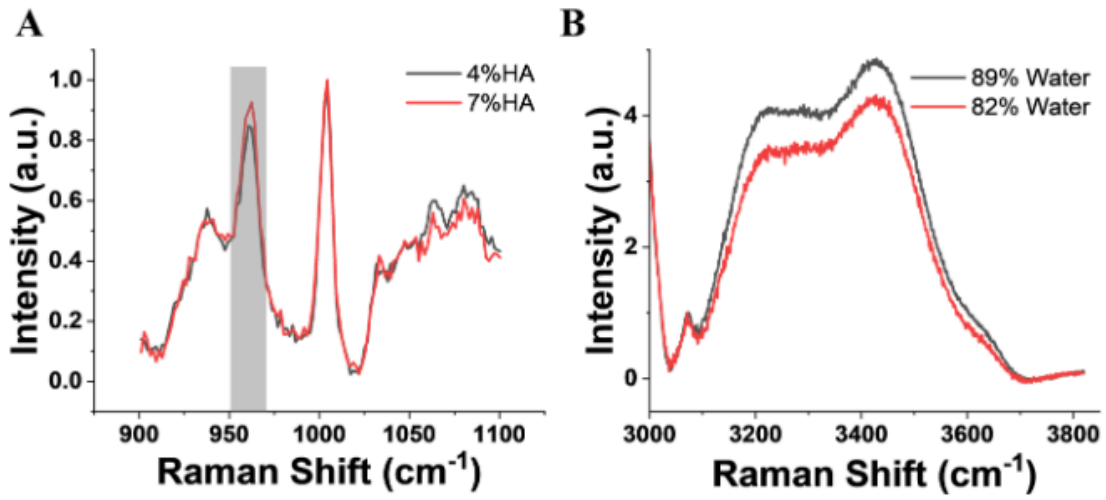

Figure S4 Raman spectra of (A) 7% and 4% hydroxyapatite (HA) phantoms with a 5 mm top layer under 6 mm ring illumination in the fingerprint region. (B) 89.1% and 81.7% water phantoms with a 5 mm top layer under 6 mm ring illumination in the high-wavenumber region.

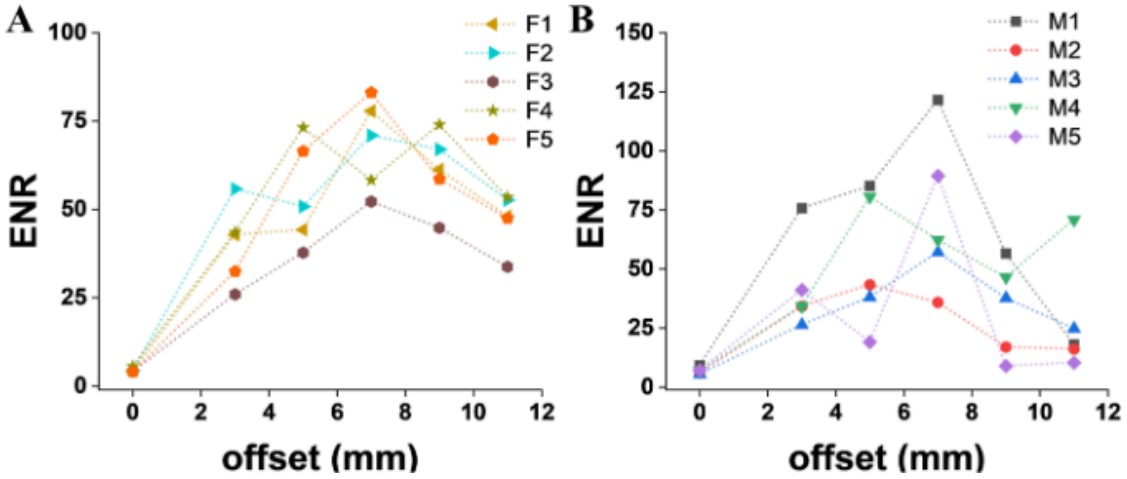

Figure S5 In-vivo measurements results from ten participants where Enhancement-to-noise ratio (ENR) is plotted against source-detector offset to identify ideal offset for (A) five female (F) participants and (B) five male (M) participants.

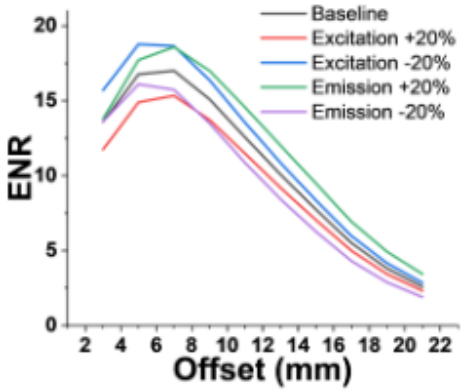

Figure S6 The absorption coefficient (μ_a) and reduced scattering coefficient (μ_s') of the top layer were scaled simultaneously by ±20% relative to their nominal values at the excitation wavelength (λex=830 nm), μ_a =0.102 cm^{-1} and μ_s'=9.07 cm^{-1}, while at the Raman emission wavelength (λem=880 nm), μ_a =0.114 cm^{-1} and μ_s'=8.21 cm^{-1}, as listed in Table 1. Variations in optical properties result in modest changes to ENR magnitude and curve width, while the optimal spatial offset shifts by less than 1 mm.

[1] Su, Joshua Weiming, et al. "Depth-sensitive Raman spectroscopy for skin wound evaluation in rodents." *Biomedical optics express* 10.12 (2019): 6114-6128.